The Analysis of the Lattice Dynamics and Thermodynamics of Major Earth-forming Silicates

Atul Patel

Department of Geological Sciences,
University College, London

Submitted for the degree of Doctor of Philosophy,
University of London.

August, 1992

ABSTRACT

There is a great demand for accurate data of structural, elastic and thermodynamic properties of the Earth-forming silicates. Experiments to simulate the conditions of the mantle and core are obviously difficult. Therefore, theoretical models which can predict the required geophysical data at such conditions are of immediate importance.

This work is a theoretical investigation into the lattice dynamics and thermodynamics of the major Earth-forming silicates. We use an atomistic approach based on the Born model of solids. This work is a rigorous test of the methodology and reliability of the lattice dynamics model at extreme geological conditions, i.e. high pressures and temperatures.

We chose the modelling of oxygen isotope fractionation between geologically relevant silicates as a stringent test for our approach. The model works very well, although the calculated fractionation factors are not yet sufficiently accurate to be practically useful.

We have compared calculations based on the quasi-harmonic approximation with corresponding molecular dynamics results for the geophysically important minerals periclase (MgO) and $MgSiO_3$ perovskite. It has been clearly shown that the quasi-harmonic approximation breaks down at high temperatures and low pressures but this deviation is reduced when the external pressure is increased. Therefore, it is necessary to use the molecular dynamics technique for upper mantle conditions and the lattice dynamics model is limited to the lower mantle although inclusion of intrinsic anharmonicity into the model will remove such restrictions.

All electron Hartree-Fock calculations were performed for the geologically relevant cubic $MgSiO_3$ perovskite (an idealised structure). Successful geometry optimisations and reasonable bulk moduli were obtained. Subsequently, potentials

obtained by fitting to such an ab initio energy surface can be incorporated into the lattice dynamics code, thus eliminating the problem of empirically determined potentials.

The inclusion of the above considerations into the lattice dynamics code will yield a reliable theoretical technique for studying minerals at any geological condition. With such a powerful tool, coupled with the growing experimental techniques to probe such levels, the models of the Earth's interior can be clarified to give an overall consistent picture.

ACKNOWLEDGEMENTS

I would like to thank Dr. Steve Parker and Prof. Masanori Matsui for the loan and use of their computer codes. The computing aspect has not been free of complications and I would like to express my appreciation to Dr. Monica Mendelssohn and the UCL Computing Centre Advisory for coming to my immediate assistance.

During the course of this studentship I have enjoyed many interesting discussions with my colleagues concerning the underlying philosophy of the subject. I would particularly like to thank Ross Angel, Guy Cooper, Matthew Genge, Tim Hackwell, Chris Hayward, Nancy Ross, John Stuart, Lidunka Vočadlo, Ian Wood and Kate Wright.

Thanks also to Kumar and Mina for their love and support.

Finally, this PhD would not have been possible without the continued support, encouragement and positive attitude that was given by my supervisor, Prof. David Price. Many thanks for sticking it out when things became a little "uncertain"! Therefore, it gives me great pleasure to dedicate this thesis to his children who, like all the other children, are the future caretakers of our beloved Earth.

August, 1992

TABLE OF CONTENTS

ABSTRACT 2

ACKNOWLEDGEMENTS 4

CHAPTER ONE

INTRODUCTION

1.0 The problem of beyond perception and the beginning of the Earth 19

1.1 Models of the Earth's interior 20
1.1.1 Seismological models 20
1.1.2 Thermal models 23
1.1.3 Mineralogical models 28

1.2 Summary 35

CHAPTER TWO

MOLECULAR AND LATTICE DYNAMICAL SIMULATION MODELS

2.0 Introduction 39

2.1 The potential energy of a crystal structure 39
2.1.1 The derivation of the potential parameters 42

2.2 The molecular dynamics simulation model 44
2.2.1 Quantum corrections to the MDS model 50
2.2.2 Anharmonicity and the MDS model 52

2.3 The lattice dynamics simulation (LDS) model 52
2.3.1 Quasi-harmonicity, anharmonicity, thermal expansion and the Grüneisen 57

2.4 Concluding remarks 59

CHAPTER THREE

A COMPUTER SIMULATION APPROACH TO MODELLING THE STRUCTURE, THERMODYNAMICS AND OXYGEN ISOTOPE EQUILIBRIA OF SILICATES

3.0 Introduction 63

3.1 Data input to PARAPOCS 64

3.2 Brillouin Zone Sampling 67

3.3 Predicted Structural, Elastic and Thermodynamic Properties. 72

3.4 Equilibrium Isotope Effects of O^{18} Substitution 79

3.5 Oxygen Isotope Partitioning. 92

3.5 Summary 110

CHAPTER FOUR

ANHARMONICITY AND THE BREAKDOWN OF THE QUASI-HARMONIC APPROXIMATION

4.0 Introduction 116

4.1 Review of recent literature on anharmonicity 117

4.2 Input for the simulation models 118

4.3 The effects of intrinsic anharmonicity on key geophysical properties 123

4.4 Summary 161

CHAPTER FIVE

QUANTUM MECHANICAL SIMULATIONS OF SILICATES

5.0 Introduction 163

5.1 Outline of model 164

5.2 Results and Discussion 165

5.3 Summary 169

CHAPTER SIX

SUMMARY

SUMMARY. 172

REFERENCES 175

APPENDIX 189

LIST OF TABLES

CHAPTER THREE

A COMPUTER SIMULATION APPROACH TO MODELLING THE STRUCTURE, THERMODYNAMICS AND OXYGEN ISOTOPE EQUILIBRIA OF SILICATES

3.1 Potential parameters used for silicates 66

3.2a The predicted values of zero-point energy and C_V for ilmenite at 300 K with varying Brillouin zone sampling techniques 70

3.2b The predicted zero-point energies and heat capacities for pyrope and α-quartz for a variety of Brillouin zone sampling procedures 71

3.3 Predicted and observed lattice parameters and cell volume 73

3.4 Predicted and observed average bond angles and average bond lengths for albite, diopside and wollastonite 74

3.5 Elastic constants and bulk moduli for the silicates studied 75

3.6 Predicted and observed average Grüneisen parameter and thermal expansion coefficient at T = 300 K 76

3.7 Predicted and observed heat capacities and entropies 77

3.8a Predicted enthalpy, zero-point energy and cell volume for the O^{16} isotope silicates 80

3.8b Predicted enthalpy, zero-point energy and cell volume for the O^{18} isotope silicates 82

3.9a Calculated lattice energies, Gibbs free energies and heat capacities at constant volume for the O^{16} silicates 92

3.9b Calculated lattice energies, Gibbs free energies and heat capacities at constant volume for the O^{18} silicates 95

3.10a Predicted average Grüneisen parameter, isothermal bulk modulus and thermal expansion coefficient for the O^{16} isotope silicates 98

3.10b Predicted average Grüneisen parameter, isothermal bulk modulus and thermal expansion coefficient for the O^{18} isotope silicates 100

3.11 Predicted heat capacity and entropy for the O^{18} isotope silicates . . . 103

3.12 Predicted and observed fractionation factors 110

3.13 Reduced partition function ratios of the silicates studied 113

CHAPTER FOUR

ANHARMONICITY AND THE BREAKDOWN OF THE QUASI-HARMONIC APPROXIMATION

4.1 Potential parameters used for MgO and $MgSiO_3$ 118

4.2a Calculated Anderson-Grüneisen parameters for MgO.FI 134

4.2b Calculated Anderson-Grüneisen parameters for MgO.PI 137

4.2c Calculated Anderson-Grüneisen parameters for $MgSiO_3$ 138

CHAPTER FIVE

QUANTUM MECHANICAL SIMULATIONS OF SILICATES

5.1 Calculated energies, bulk moduli and cell volumes. 170

APPENDIX

A1 Enthalpy and volume data calculated at various pressures and temperatures for MgO.FI LDS model 189

A2 Enthalpy and volume data calculated at various pressures and temperatures for MgO.FI MDS model 191

A3 Enthalpy and volume data calculated at various pressures and temperatures for MgO.PI LDS model. 193

A4 Enthalpy and volume data calculated at various pressures and temperatures for MgO.PI MDS model. 195

A5 Enthalpy and volume data calculated at various pressures and temperatures for $MgSiO_3$ perovskite LDS model 197

A6 Enthalpy and volume data calculated at various pressures and temperatures for $MgSiO_3$ perovskite MDS model 199

LIST OF FIGURES

CHAPTER ONE

INTRODUCTION

1.1 PREM model: Seismic velocities and density profile 22

1.2 PREM model: Pressure profile 22

1.3 PREM model: Seismic parameter profile 23

1.4 PREM model: Poisson's ratio profile 23

1.5 Schematic diagrams of the whole-mantle and layered convection models and corresponding temperature and viscosity profiles 27

1.6 Geotherms from various techniques. 28

1.7 Principle of the diamond-anvil cell. 31

1.8 P, T Phase diagram for $MgSiO_3$ composition 32

1.9 Isothermal (T=1000°C) phase diagram for the $MgSiO_3$-$FeSiO_3$ system 33

1.10 P, T phase diagram for the Mg_2SiO_4 polymorphs 34

1.11 Isothermal (T=1600°C) calculated phase diagram for the Mg_2SiO_4-Fe_2SiO_4 system 35

CHAPTER TWO

MOLECULAR AND LATTICE DYNAMICAL SIMULATION MODELS

2.1 Asymmetric potential "well" 42

2.2 Thermal expansion 59

CHAPTER THREE

A COMPUTER SIMULATION APPROACH TO MODELLING THE STRUCTURE, THERMODYNAMICS AND OXYGEN ISOTOPE EQUILIBRIA OF SILICATES

3.1a Isotopic volume differences vs. temperature for albite, diopside and forsterite 85

3.1b Isotopic volume differences vs. temperature for pyrope, α-quartz and wollastonite 86

3.2a Isotopic zero-point energy differences against temperature for albite, diopside and forsterite 88

3.2b Isotopic zero-point energy differences against temperature for pyrope, α-quartz and wollastonite 89

3.3a Isotopic heat capacity differences vs. temperature for albite, diopside and forsterite 91

3.3b Isotopic heat capacity differences vs. temperature for pyrope, α-quartz and wollastonite 92

3.4 The temperature dependency of the fractionation factor 110

CHAPTER FOUR

ANHARMONICITY AND THE BREAKDOWN OF THE QUASI-HARMONIC APPROXIMATION

4.1 Plot of static pressure and vibrational pressure (for selected temperatures) as a function of lattice constant 118

4.2a Temperature dependence of the molar volume of MgO at zero pressure 122

4.2b Pressure dependence of the molar volume of MgO at 300K 122

4.2c The P-V-T relations of perovskite 123

4.3a Calculated molar volumes for MgO.FI 125

4.3b Calculated molar volumes for MgO.PI. 126

4.3c Calculated molar volumes for $MgSiO_3$ 127

4.4a Calculated enthalpies for MgO.FI 129

4.4b Calculated enthalpies for MgO.PI 130

4.4c Calculated enthalpies for $MgSiO_3$ 131

4.5a Calculated thermal expansion coefficients for MgO.FI 132

4.5b Calculated thermal expansion coefficients for MgO.PI 133

4.5c Calculated thermal expansion coefficients for $MgSiO_3$ 134

4.6a Calculated isothermal bulk moduli for MgO.FI 140

4.6b Calculated isothermal bulk moduli for MgO.PI 141

4.6c Calculated isothermal bulk moduli for $MgSiO_3$ 142

4.7a Calculated heat capacities at constant pressure for MgO.FI 144

4.7b Calculated heat capacities at constant pressure for MgO.PI 145

4.7c Calculated heat capacities at constant pressure for $MgSiO_3$ 146

4.8a Comparison of the LDS calculated heat capacity at constant volume for $MgSiO_3$ at 0.001 and 100.0 (top plot) kbars pressure 148

4.8b Comparison of the LDS calculated heat capacity at constant volume for $MgSiO_3$ at 200.0 and 300.0 (top plot) kbars pressure 149

4.8c Comparison of the LDS calculated heat capacity at constant volume for $MgSiO_3$ at 400.0 and 500.0 (top plot) kbars pressure 150

4.8d Comparison of the LDS calculated heat capacity at constant volume for $MgSiO_3$ at 1000.0 kbars pressure 151

4.9a Calculated heat capacities at constant volume for MgO.FI 152

4.9b Calculated heat capacities at constant volume for MgO.PI 153

4.9c Calculated heat capacities at constant volume for $MgSiO_3$ 154

4.10a Calculated average Grüneisen parameters for MgO.FI 155

4.10b Calculated average Grüneisen parameters for MgO.PI 156

4.10c Calculated average Grüneisen parameters for $MgSiO_3$ 157

4.11 Deviation (LDS model away from the MDS model) contours (0.25%, 0.5% and 1.0%) for the molar volume of MgO.FI 159

4.12 Deviation (LDS model away from the MDS model) contours (2%, 10% and 15%) for the thermal expansion coefficient of MgO.FI .. 160

4.13 Deviation (LDS model away from the MDS model) contours (2%, 5% and 10%) for the isothermal bulk modulus of MgO.FI 161

CHAPTER FIVE

QUANTUM MECHANICAL SIMULATIONS OF SILICATES

5.1a Variationally optimised inner and outer exponents of silicon 167

5.1b Variationally optimised inner and outer exponents of oxygen. 168

5.2 Variationally optimised lattice parameter for the cubic $MgSiO_3$ perovskite 169

CHAPTER ONE

INTRODUCTION

In this thesis we present a theoretical analysis of the lattice dynamics and thermodynamics of the major Earth-forming silicates. This includes a test of the reliability of the model at the relevant geological conditions, i.e. high pressures and temperatures. The structure of the thesis is presented at the end of this chapter as we wish to develop the preliminary ideas and clarify the key presuppositions which are implicit in the geosciences. A brief discussion of the current models for the interior of the Earth will now be given, highlighting the interrelationships and interdependency between the seismological, thermal and compositional theories. It is hoped that this will provide a clear context for the work presented in this thesis.

1.0 The problem of beyond perception and the beginning of the Earth

How is it possible to study the Earth's interior? The planet is far too big to simply dig a hole and take a look! It is possible to observe phenomena on the surface and then by proposing explanations and causal relationships we may infer and gain insight into the interior. A test, not only in science but all knowledge, is consistency. If a prediction from a theory is not observed from experiment or is inconsistent with other models then the theory is obviously limited and has to be revised or dismissed. Through lack of information it may still be necessary to make some presuppositions and the geosciences are no exception to this.

The beginning of the Earth is still a mystery and a totally consistent model is yet to emerge. Brown and Mussett (1981) give an account of the different classes of theories which attempt to explain the mystery. A brief summary of the main

ideas of the three classes of theories will now be given.

The first class of theory states that the Sun was fully formed before the planets and the material of the planets came directly from the Sun or another star. The once widely accepted "tidal theories" belong to this class. The second class of theories assumes that the Sun and all the planets all formed from a rotating cloud or nebula as a natural result of the evolution of the cloud in response to gravitational and other forces. Finally, the last group of theories agrees with the first that the Sun was fully formed before the planets but states that the planetary material was drawn from interstellar clouds or other sources to form a nebula.

A relevant example of such a test of consistency in the Earth sciences is the analysis of chondritic meteorites as a reflection of the composition of the original solar nebula. Clearly, such tests lead to, not only a fuller understanding of the theory but also an awareness of its limitations. Excellent treatises of how the Earth models weave together are Poirier (1991) and Anderson (1989). A brief review of the current models of the interior of the Earth is presented in the following section. This gives the precise context of the work undertaken in this thesis.

1.1 Models of the Earth's interior

The models to describe the interior of the Earth fall into three categories; seismological, thermal and compositional (mineralogical). Each theory uses pieces of information to support each other, resulting in a complex weaving of relationships. As stated earlier, the more consistency emerges, the more we feel that we are reaching a true understanding of the Earth.

1.1.1 Seismological models

The seismological models are based on velocity-depth profiles determined

from travel-time-distance curves for seismic waves, and on periods of free oscillations (see, for example, Bolt 1982). Due to a network of sophisticated world-wide seismograms the quantity and amount of data has increased so that it is possible to collect all the results into one overall model. The International Association of Seismology and Physics of the Earth's Interior have decided on such a model and it is referred to as the preliminary reference Earth model (PREM) (see, Dziewonski and Anderson 1981). Seismological models yield density, pressure and elastic moduli as functions of depth and these are shown in Figures 1.1 to 1.4 for the PREM model.

The main assumptions made in order to derive the density-depth expressions will now be outlined without including the mathematical technicalities. Compression is assumed to be adiabatic, that is, there is no exchange of heat which could cause temperature variations and add a thermal expansion contribution to the density variations with pressure. It is also assumed that the Earth is in hydrostatic equilibrium and spherically symmetric, hence, it is possible to formulate simple expressions for both pressure and acceleration due to gravity profiles with depth in order to derive a density-depth expression. The Adams-Williamson equation (see, Williamson and Adams 1923) relates density and bulk moduli with depth and therefore is an equation of state. For depths where non-adiabaticity occurs, it is possible to add a thermal expansion term to the Adams-Williamson equation to provide a necessary correction. Figure 1.1 shows the velocity and density profiles of the PREM model.

Figures 1.2, 1.3 and 1.4 are the variations of pressure, seismic parameter and Poisson's ratio with depth respectively. All this information of the Earth's interior now provides constraints on the other models, namely, the thermal and compositional models.

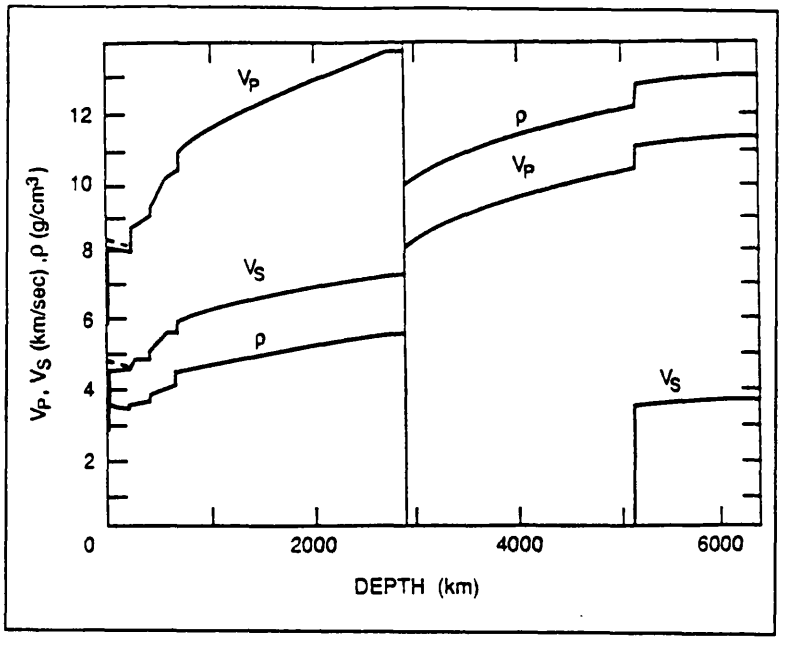

Figure 1.1 PREM model: Seismic velocities and density profile (after Dziewonski and Anderson 1981)

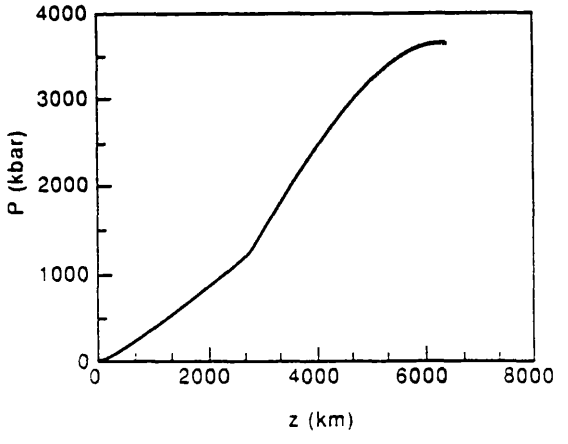

Figure 1.2 PREM model: Pressure profile

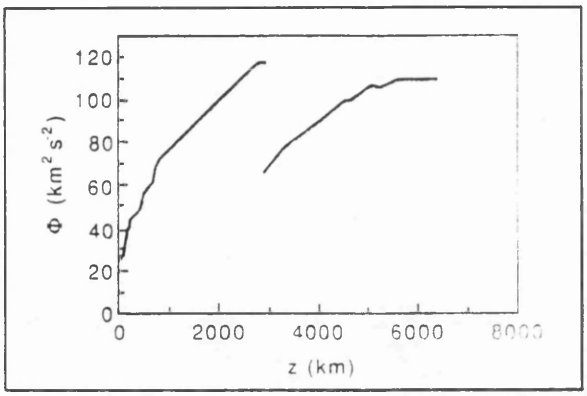

Figure 1.3 PREM model: Seismic parameter profile

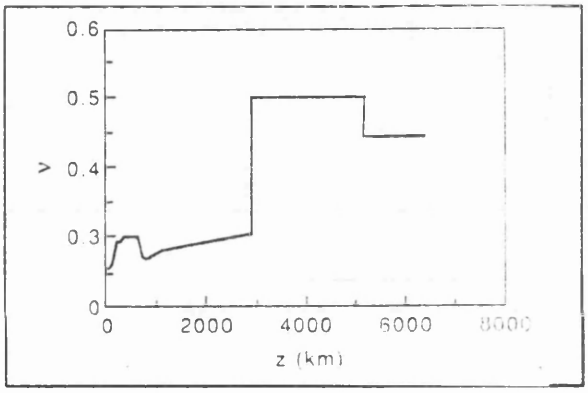

Figure 1.4 PREM model: Poisson's ratio profile

1.1.2 Thermal models

How does temperature vary with depth? Equations of state are the variations of a property with pressure and temperature, therefore, if we wish to develop a satisfactory compositional model it is necessary to have some knowledge of the geotherms, that is, the variation of temperature with depth. The thermal models attempt to give such a temperature-depth profile. Also discussed in this section are the various heat transport mechanisms and patterns of convection in the mantle.

The boundary condition for any thermal model is the heat flux coming from inside the Earth which can be measured at the surface and has a mean value of 80 mW /m^2. To infer a temperature profile one must also have some knowledge of the sources of heat which are transported through the mantle and eventually radiated at the surface.

The sources of heat fall into three categories classified by original, radiogenic and "others". The "original" heat is the accretional heat due to the dissipation of gravitational energy when planetesimals bombarded the surface of the growing Earth, which eventually partly melted. This theory partly assumes that the Earth is still cooling after its initial hot state, but this belief is not held by all, and hence is still a matter of debate.

Radiogenic heat is the heat given off from the radioactive decay of elements U^{235}, U^{238}, Th^{232} and K^{40}. The heat production per mass unit of each element is well known but their concentration in the Earth is much less certain. One estimate (Verhoogen 1980) states that the total radiogenic production of heat in the mantle accounts for at least 60% of the total heat output.

Other sources of heat may be tidal dissipation in the solid Earth and frictional dissipation in the convecting mantle. These contributions are assumed to be negligible in comparison to the radiogenic heat. However, a significant contribution to the total heat output could be the latent heat released during crystallization of the inner core and by the gravitational energy released as particles of solid iron fall toward the inner core and as the mantle falls in on a shrinking core. The heat flux from the core into the lower mantle is another boundary condition for the convective problem. It is estimated to be about 10% of the total heat output of the Earth (Verhoogen 1980).

Due to the opacity of iron-bearing minerals at high pressure, radiative transfer of heat is assumed to be negligible in the Earth's mantle. Therefore, the two remaining mechanisms for heat are convection and conduction. The latter can

be viewed as vibrations through crystal structures. Convection is when heat containing material is transported from one location to another.

Convection in the mantle is when heat containing matter is bodily transported in a fluidlike manner. To gain some insight into the conditions under which convection takes place we consider a layer of fluid in a gravitational field. The lower surface is at a higher temperature than the upper surface and hence, there is a temperature gradient. The nature of the temperature gradient in the fluid determines whether there is convection or not. If an element of fluid rises along the adiabatic temperature gradient then it will undergo a decompression without any loss of heat. For a temperature gradient less than the adiabatic gradient (subadiabatic), the element of fluid is cooler, hence denser than the surrounding fluid and sinks again. The fluid is stratified and stable with respect to convection and heat is transported by conduction. If the temperature gradient in the fluid is superadiabatic, that is, steeper than the adiabatic gradient, the element of fluid is warmer and lighter than the surrounding fluid; it is buoyant and will go on rising. In this case, the situation is unstable and provides the criterion for the onset of convection. A tighter criterion is given by the dimensionless Rayleigh number which measures the relative importance of the buoyancy force (which is proportional to the acceleration due to gravity, the thermal expansion coefficient and the temperature gradient) and the viscosity drag force (which hinders convection).

Continental drift and plate tectonics are a clear indication that the upper mantle convects. Recent measurements of the Rayleigh number and Bullen parameter (another constant which provides a criterion for convection) have led to the conclusion that the lower mantle also convects. The patterns of convection are a matter of considerable debate and have fallen into two main categories; whole mantle and two-layer convection. Figure 1.5 shows a schematic diagram of each pattern along with their corresponding temperature and viscosity profiles. Therefore, more accurate knowledge of temperature and viscosity varying with depth could lead to a clearer picture of the patterns of convection in the mantle. As yet, there

is still not enough experimental evidence or theoretical consistency to end the dispute of the convection patterns in the mantle.

Geotherms are temperature profiles as a function of depth and are usually anchored at the seismic discontinuities identified with phase transitions whose P, T boundaries are experimentally known or extrapolated. From these points the geotherms follow an adiabat in the homogenous regions, where the Bullen parameter is close to 1.0 (lower mantle and outer core). The adiabatic gradient is often determined by using a value of the acoustic Grüneisen parameter compatible with a seismological Earth model. The uncertainty in the temperature is usually not less than a few hundred degrees and can be as much as 1000K. The geotherm calculated or measured from various techniques are shown in Figure 1.6

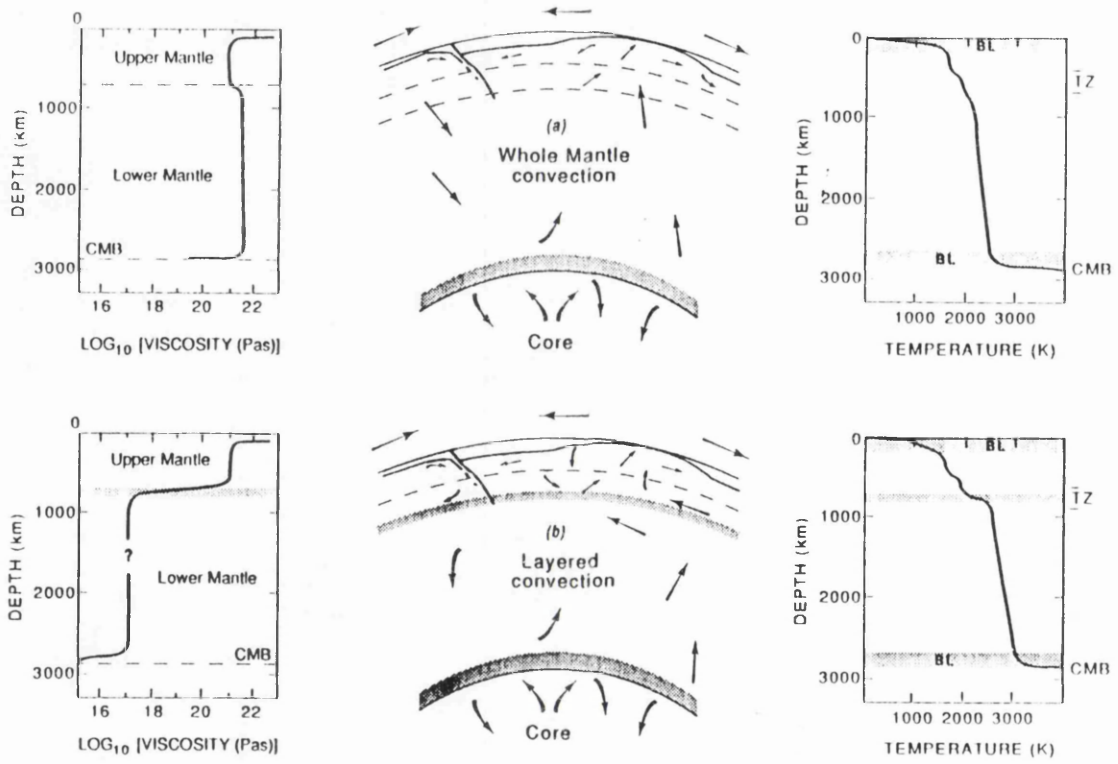

Figure 1.5 Schematic diagrams of the whole-mantle and layered convection models and corresponding temperature and viscosity profiles (after Peltier and Jarvis 1982)

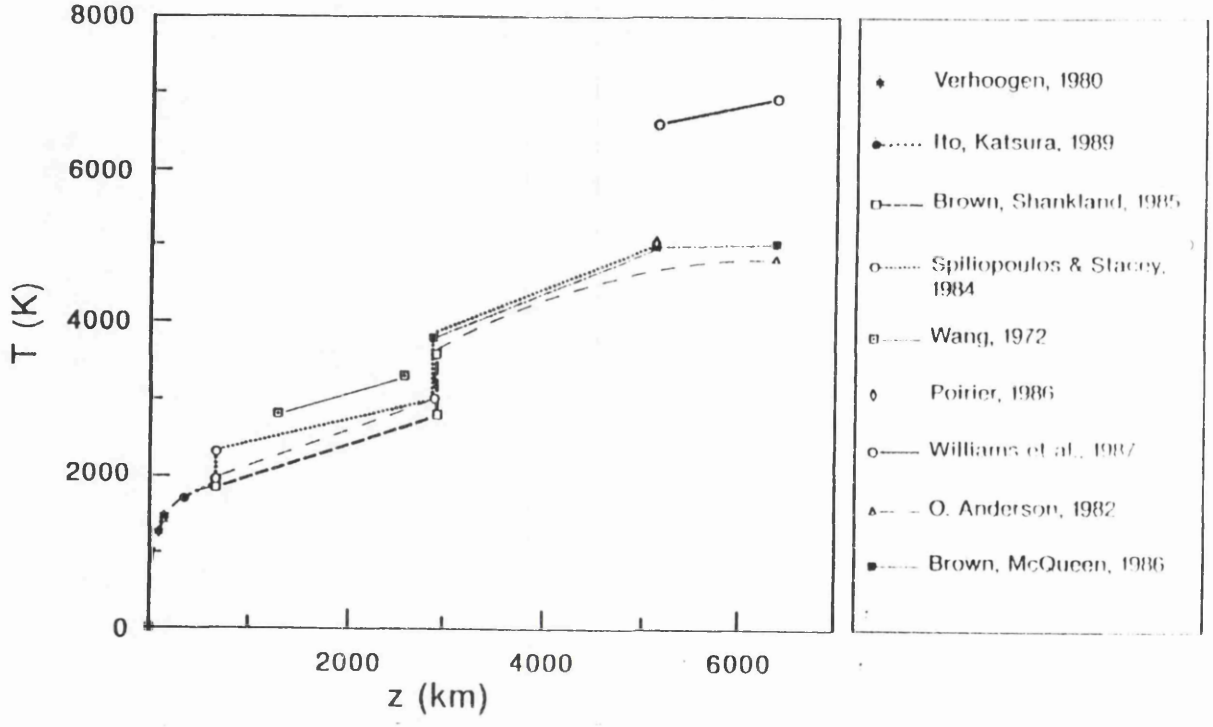

Figure 1.6 Geotherms from various techniques. For all these temperature profiles, the error bar is about ±800K (after Poirier 1991)

1.1.3 Mineralogical models

This section concludes the summary presented in this thesis of the models which attempt to give a description of the Earth's interior. All models, as we have seen, require consistency between each other for an overall coherent view of the Earth.

The compositional models are constrained by the seismological models where a direct correlation with the velocity and density profiles is required. The initial conditions of the composition of the Earth is derived from assumptions of the primitive bulk Earth composition and the chemical evolution of the Earth. The mineralogical model is then tailored to fit the needs of the various convection models and therefore, conditions the choice of geotherm.

There are two approaches to constructing a compositional model. Firstly, the actual density and elastic moduli at various depths are adiabatically extrapolated to zero pressure and brought down from the final temperature to room temperature. A mineral assemblage is devised so that its density and aggregate elastic properties fit the decompressed material. Alternatively, a mineral assemblage at room temperature and ambient pressure is synthesised so that after heating and adiabatically compressing it, its density and seismic velocities fit the seismological model.

Discrepancies between contending mineralogical models arise from two sources. The models use different assumptions for the primitive bulk Earth composition and its evolution. It is generally assumed that the primitive composition of the bulk Earth (and terrestrial planets) is that of the devolatilized solar nebula (Hart and Zindler 1986). The problem is to decide what is the composition of the original solar nebula and to what degree it has lost its elements. The second source of discrepancy lies in the choice of elastic and thermal parameters of the high-pressure candidate minerals. Most of them are, if not unknown, at least subject to a high degree of uncertainty, stemming either from the

inherent experimental errors and/or from the fact that we must rely on one measurement. Obviously, there is a pressing need for accurate laboratory measurements of these parameters for the high pressure phases.

The development of theoretical models which predict the relevant data would not only be a complementary approach, but also relieves the difficult task of performing precise experiments of such practically unattainable conditions. This indicates the precise context of the work presented in this thesis and will be further qualified in the last section of this chapter. The bulk of the mineralogical models is the study of phase transitions of minerals. A brief overview of this subject is now presented.

The phase of a mineral can be viewed as the relative stability field in terms of the intensive parameters pressure and temperature. If the parameters are varied then there is a movement through different phases, and between these phases are the phase transitions. The "order" of a phase transition can indicate the type changes that take place within a crystal structure. A first-order transition is associated with a change in volume, where atoms or ions are actually moving from their sites to other locations. A second-order transition is often displacive and corresponds to a mere distortion of bonds. Most of the experimental work in the recent years has been carried out using two high-pressure techniques; the multi-anvil apparatus, up to 250kbar, and the laser heated diamond-anvil cell (Figure 1.7), up to 1Mbar (see, for example, Bassett 1977; Hemley et al. 1987).

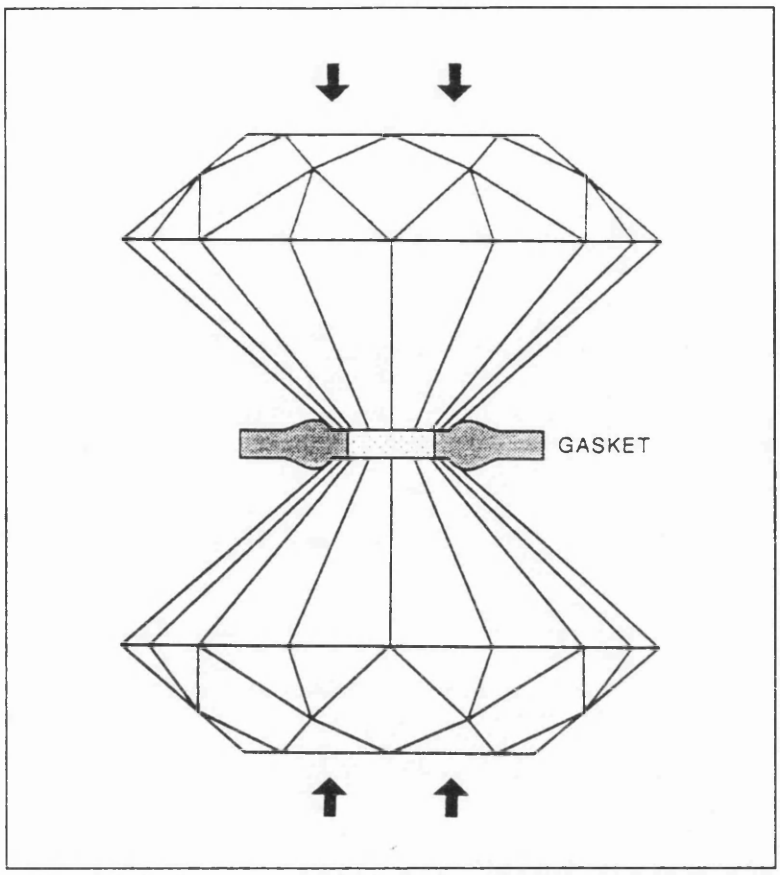

Figure 1.7 Principle of the diamond-anvil cell. The sample (stippled) is contained in a small hole (200 to 400 μm) drilled in a metal gasket, compressed by the diamonds. It can be heated by focusing a laser beam on it. (After Poirier 1991).

The most recent experimentally observed phase transitions of geologically important minerals are shown in Figures 1.8, 1.9, 1.10 and 1.11. It is generally assumed that $MgSiO_3$ and Mg_2SiO_4 are two of the most significant minerals with respect to the Earth's interior (see, for example, Poirier 1991; Anderson 1989) and their phase transitions are shown in the above mentioned figures. We see from Figures 1.8 and 1.9 that the structure of $MgSiO_3$ evolves from pyroxene through to garnet, ilmenite and perovskite with increasing pressure. It is thought that about 80% of the lower mantle consists of $(MgFe)SiO_3$.

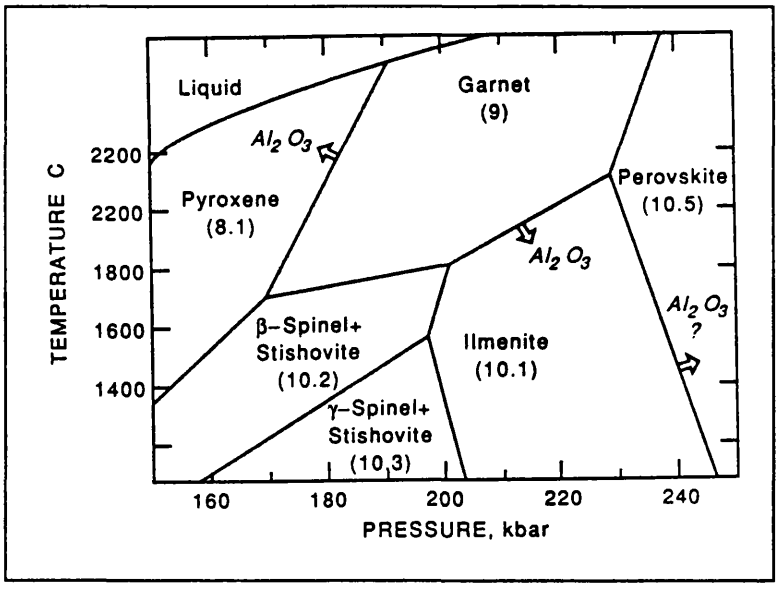

Figure 1.8 P, T Phase diagram for $MgSiO_3$ composition. The approximate velocity of P waves (in km/s) is indicated below the names of the mineral phases. The arrows show the direction in which the phase boundaries are expected to move when Al_2O_3 is added (after D. L. Anderson 1987a)

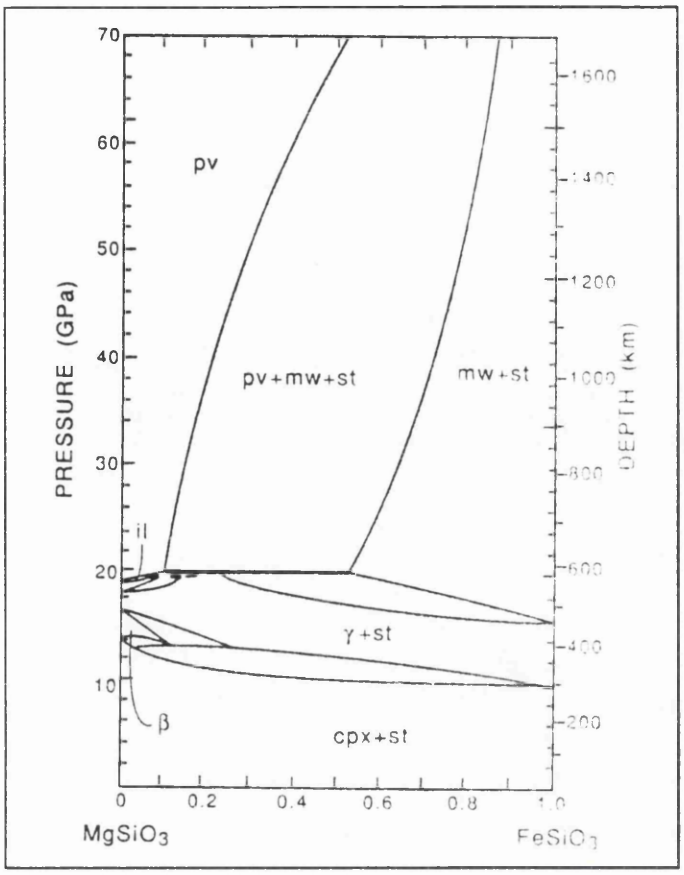

Figure 1.9 Isothermal (T=1000°C) phase diagram for the $MgSiO_3$-$FeSiO_3$ system. The crystalline structures are cpx (clinopyroxene), β (β-phase), γ (γ-spinel, mw magnesiowüstite), st (stishovite), pv (perovskite) (after Jeanloz and Thompson 1983).

The important and possibly dominant mineral of the upper mantle is olivine $(Mg_{1-x}Fe_x)_2SiO_4$ (with $x \cong 0.1$). Figure 1.10 shows the variation Mg_2SiO_4 polymorphs with increasing temperature and pressure. The calculated phase diagram of the Mg_2SiO_4-Fe_2SiO_4 system is shown in Figure 1.11.

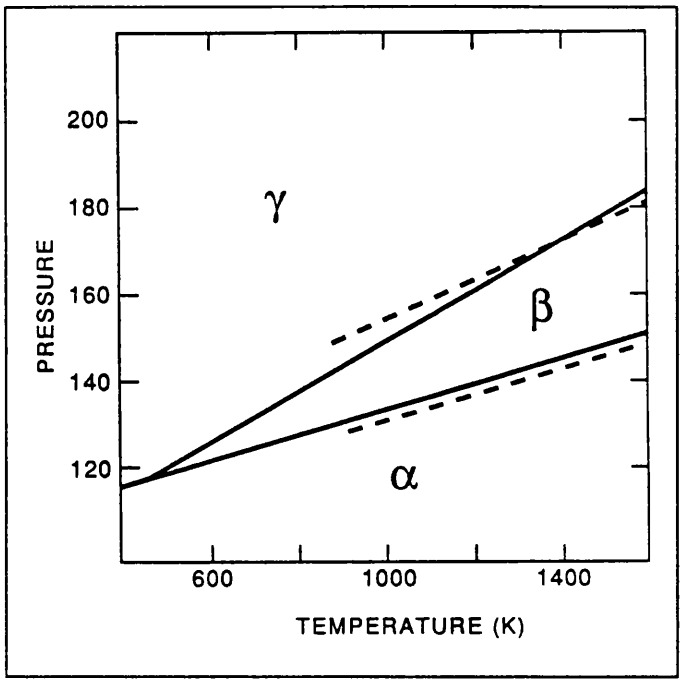

Figure 1.10 P, T phase diagram for the Mg_2SiO_4 polymorphs (α: olivine, β: modified spinel phase, γ: spinel). Solid lines from Akaogi et al. (1984), dashed lines from Suito (1977) (after Akaogi et al. 1984).

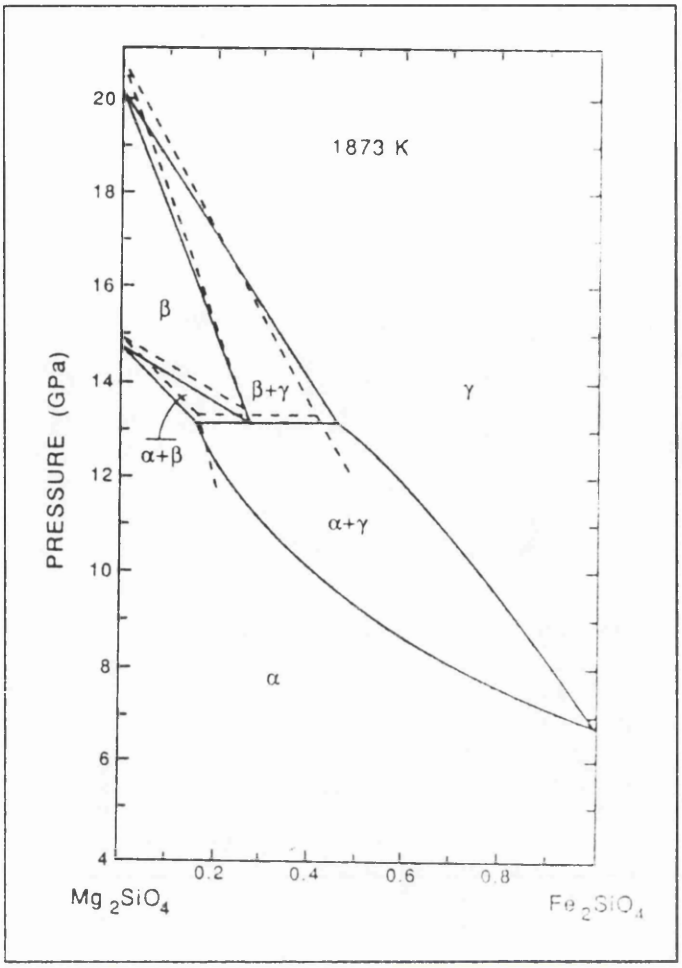

Figure 1.11 Isothermal (T=1600°C) calculated phase diagram for the Mg_2SiO_4-Fe_2SiO_4 system. The crystalline structures are α (olivine), β (β-phase), γ (γ-spinel). The boundaries experimentally determined by Katsura and Ito (1989) are shown by dashed curves (after Akaogi et al. 1989).

This concludes the brief overview of the models of the Earth's interior. The remaining section of this chapter outlines the objectives of the research presented in this thesis and also summarises the flow of ideas as presented chapter by chapter.

1.2 Summary

As was stated in the previous section, there is a great demand for accurate data of structural, elastic and thermodynamic properties of the Earth-forming silicates so that refinements can be made to existing compositional models and discrepancies between the precise interrelationships of the models are clarified. It is hoped that insight into the exact conditions for the formation and evolution of the Earth is gained. Experiments to simulate the conditions of the mantle and core are obviously difficult. Therefore, theoretical models which can predict the required geophysical data at such conditions are of immediate importance.

Currently there are three ways to model the physical structure and properties of the crystalline phase: classical, semi-classical and quantum mechanical. The classical approach, known as molecular dynamics and Monte Carlo methods, are based upon solving Newton's equations of motion for an ensemble of atoms or ions which constitute the crystalline material. The lattice dynamics model is referred to as semi-classical because it contains the non-classical novelty of wave-particle duality. The kinetic or "dynamic" energy of the crystal is assumed to be the sum of all the lattice vibrations. Both the molecular and lattice dynamical methods use a potential model to simulate the net forces between the atoms or ions. Most of the physical properties predicted by these models are derived from the potential or some derivative of the potential. Hence, the accuracy of the calculated properties is sensitive to the "realism" of the potential model. A full discussion of this as well as an outline of the theory of molecular and lattice dynamics is given in Chapter Two. Similarities and differences between the two methods are also presented.

The lattice dynamical simulation method has recently been a topic of detailed research (see, for example, Parker and Price 1989; Catlow and Mackrodt 1982). Many developments to the simulation codes have allowed the possibility of modelling a whole variety of silicate structures over a wide range of temperature and pressure. It is for these reasons that the test of the lattice dynamics method for geologically relevant conditions is the core of the research presented in this thesis.

Isotope exchange reactions between minerals involve small energy changes and to model such subtleties is a stringent test for any model. The prediction of the fractionation factors as a function of temperature for oxygen isotope exchange reactions between the rock-forming minerals: albite, diopside, forsterite, pyrope, quartz and wollastonite, was chosen as a sufficient "probe" for the potential model of the lattice dynamics approach. Such predictions are also of geophysical importance in the context of geothermometry and can provide useful constraints for geotherms. The detailed analysis of, not only the fractionation factors, but also other predicted structural, elastic and thermodynamic data is presented in Chapter Three.

For the simulation model to be useful when applied to the geophysical context it has to perform well at high temperatures and pressures, i.e. the conditions of the Earth's interior. The potentials have previously been modelled for silicates (see, for example, Sanders et al. 1984; Lewis and Catlow 1985), therefore, this limits the applicability of the lattice dynamics model to the compositions of the upper and lower mantle. The model calculations are performed at the quasi-harmonic level of approximation. This treats the potential energy function as a quadratic, that is, a symmetrical parabola, but allows for the effect of thermal expansion. This approximation works well for low temperatures as the ions in the lattice do not move significantly away from their equilibrium positions. However, at high temperatures there will be anharmonic effects due to the asymmetrical form of the "true" potential. Hardy (1980) states that these anharmonic effects increase with temperature but decrease with increasing pressure. Hence, the lattice dynamics simulation code may be applied to mantle conditions without due concern for anharmonicity if Hardy's (1980) hypothesis is correct. We test this hypothesis by comparing molecular and lattice dynamical simulations of MgO (periclase) and $MgSiO_3$ (perovskite) at a wide range of temperature and pressure. It is assumed that the molecular dynamics method includes the anharmonic effects so that by comparing the predicted physical parameters: enthalpy, volume, thermal expansion coefficient, isothermal bulk modulus, heat capacity and so on, with those obtained from the lattice dynamics simulations, it is possible to pinpoint the magnitude of

anharmonicity as a function of temperature and pressure and also see if the two approaches converge at high temperatures and pressures. This work is presented in Chapter Four.

Recent developments on simulation codes have given rise to a quantum mechanical treatment of periodic structures (Pisani et al. 1988). The exact solution of Schrödinger's equation for a many-body system is, as yet, impossible therefore the calculations are performed at the Hartree-Fock level of approximation. A detailed discussion of this as well as a brief outline of the theory and preliminary calculations of the energy, optimised volume and bulk modulus of cubic perovskite is given in Chapter Five. The possibility of quantum mechanical simulations of the charge density within a crystal structure, lending information for the development of "a priori" potential models, is also discussed.

Finally, the main points to arise from the work in this thesis is summarized in Chapter Six. Also presented in the final chapter are suggestions for future work and developments especially regarding the potential model for the lattice dynamics simulation technique.

CHAPTER TWO

MOLECULAR AND LATTICE DYNAMICAL SIMULATION MODELS

2.0 Introduction

In this chapter we discuss the two simulation approaches, molecular and lattice dynamics, which are used for the research presented in this thesis. Energy is viewed as activity and subsequently potential energy is discussed in terms of "implicit" activity. The potential model is the crux to both simulation techniques because it is from the form and derivatives of the explicit potential energy equations that all dynamic properties are derived. This matter is discussed in detail and a summary of the method for obtaining the potential parameters is given. The molecular dynamics model is presented in great detail showing the derivations and equations which link the potential model to the dynamical variables. A similar treatment is given for the lattice dynamics model and the chapter is concluded with an analysis of anharmonicity and its deviations from the quasi-harmonic approximation.

2.1 The potential energy of a crystal structure

As stated above, energy is presupposed to be activity or process and hence, motion is a manifestation of energy and is usually represented as the sum of kinetic and potential component of the dynamical system. The kinetic component is the quantification of the movement of the whole system (the crystal structure) or the components of the system (atoms or ions in our case) and the potential energy is

the amount of activity or work needed to bring about the crystal structure. This is usually expressed as the energy required to bring the atoms or ions from infinite distances from each other to their locations in a crystal structure. Alternatively, one can view the crystal structure as sitting in a "field" or context which, although ultimately extends to the whole Universe, is abstracted or reduced to a limited domain which can be handled mathematically. Due to the minute masses of crystals in comparison with planets, the effects of gravitation can be neglected. Also, we can neglect the effects of the strong and weak force as these deal with a deeper level of system than we wish to deal with (i.e. less than 10^{-13} metres). We also assume that the magnetic effects within ions give a negligible contribution to the overall potential energy of the crystal structure. It follows then, that the first component of the potential energy is the electrostatic or Coulombic term (without constants):

$$U_C = \Sigma_{ij} e^2 q_i q_j r_{ij}^{-1}, \qquad (2.1)$$

where e is the charge of the electron, q_i and q_j are the point charges associated with ions i and j, and r_{ij} is the distance between them. This expression models the forces between ions in the crystal structure which arise directly from their internal motions. This gives an intuitive and imaginative picture of the cause for such forces. Note that from interpreting Newton's equations of motion, a force can be defined as the effect of motion or, more specifically, the rate of change of the rate of change of position with respect to time. Hence, this makes the above interpretation of the electrostatic interaction viable.

The intrinsic activity within the charged ions could lead to many effects which have a significant contribution to the overall potential energy. Obviously, it is not possible to model all these effects and so an approximation is made based on the Born model of solids (Born and Huang 1954) which states that the interatomic potentials are defined to simulate the net forces between the ions. These forces are usually assumed to be pair-wise additive.

The Buckingham potential is used to describe the short-range repulsive and attractive dispersion forces between the ions and takes the following form:

$$U_{SR} = \Sigma_{ij} A_{ij} \exp(-r_{ij}/\rho_{ij}) - C_{ij} r_{ij}^{-6}, \qquad (2.2)$$

where A_{ij} and ρ_{ij} are the effective repulsive parameters and C_{ij} is the effective dispersion coefficient. These potential parameters have to be derived for each pair of species i and j and this is achieved via empirical fitting procedures (see, for example, Lewis and Catlow 1985). This topic will be further elucidated in section 2.1.1. The short-range repulsive force arises from the forbiddance of overlapping electron clouds of neighbouring ions. This is a direct result of the Pauli exclusion principle which states that no two species can have the same quantum numbers or in less technical terms, they cannot occupy the same space at the same time. The internal activity of the charged ions leads to creation of dipoles which can give rise to mutual dipole-dipole attractions between neighbours. This is known as the van der Waals interaction and is modelled by the r^{-6} term in the Buckingham potential.

Figure 2.1 shows how the contributions from the long-range Coulomb attractive potential and the short-range dispersive and repulsive interactions give an overall asymmetric potential "well" which shows the variation in potential energy as a function of interatomic spacing.

Both potentials 2.1 and 2.2 are employed in the molecular dynamics (MDS) and lattice dynamics (LDS) simulation techniques. It is possible to model other forces that can arise from the internal processes within the ions: many-body effects and polarizability are such examples, however, the MDS code generally do not incorporate these developments as they have given successful simulations without the need of these additional terms (see for example, Dove 1988; Matsui 1988). Hence, the remaining components to the potential energy only apply to the LDS model.

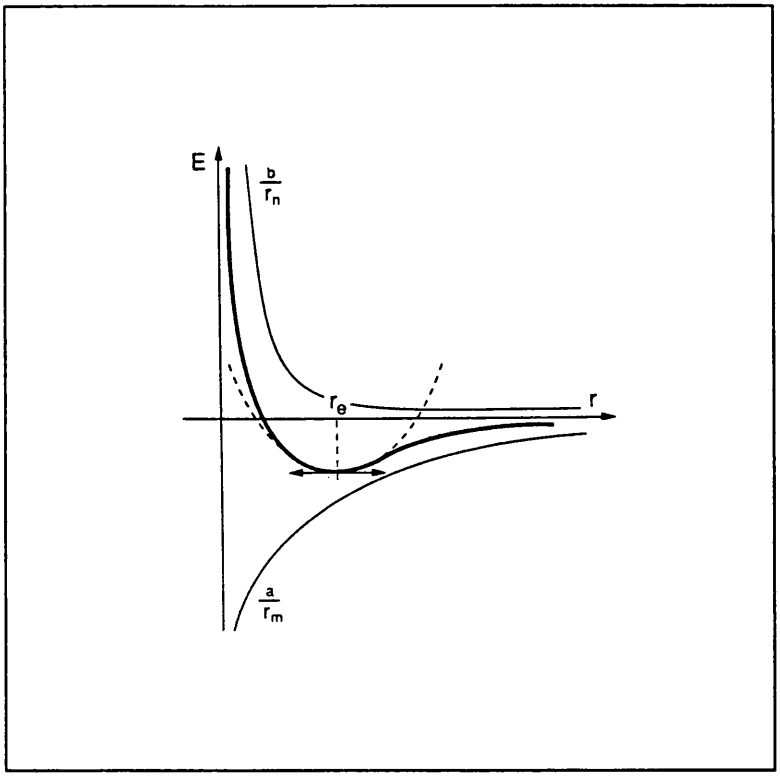

Figure 2.1 Asymmetric potential "well" (bold curve). The potential is the sum of the attractive Coulombic potential and a short-range repulsive (thin curves). The parabola at $r = r_e$ (dashed curve) corresponds to the harmonic approximation.

The shell model provides a simple description of the ease with which the charged ion is deformed by being in a particular environment and this effect is technically referred to as ionic polarizability. In this model, the ion (it is frequently assumed that oxygen is the only polarizable atom in the structure) is described as having a core containing all the mass, surrounded by a massless shell of charge Y, representing the outer valence electron cloud. The core and shell are coupled by a harmonic spring, so that their interaction can be expressed as:

$$U_P = \Sigma_i k_{S,i} r_i^2, \qquad (2.3)$$

where $k_{S,i}$ is the spring constant, and r_i is the core-shell separation. The free-ion

polarizability (α) is given by the term:

$$\alpha = Y_i^2/(k_{S,i}). \tag{2.4}$$

In addition to these terms it has previously found (Sanders et al. 1984) that in order to describe the directionality of the O-Si-O bond in silicates, it is necessary to include in the potential a three-body or bond-bending term of the type:

$$U_B = \Sigma_{ijk} k^B_{ijk}(\theta_{ijk} - \theta_O)^2, \tag{2.5}$$

where k^B_{ijk} is the spring constant, θ_{ijk} is the O-Si-O bond angle, and θ_O is the tetrahedral angle.

Other many-body contributions and magnetic effects (eg. quadrupolar moments) are assumed to be negligible, therefore, these are not included in the overall potential model. It is important to note here that all the dynamical properties of a crystal structure are derived from the form and derivatives of the potential energy function. Hence, it is important in any solid-state model to obtain a realistic potential for the context one is investigating (e.g. covalent, ionic, metal, semiconductor, superconductor etc.). Therefore, the next section is devoted to the derivation of the potential parameters.

2.1.1 The derivation of the potential parameters

The reliability of the simulation in modelling a particular solid depends on the accuracy of the chosen potential parameters. Indeed, it is the reliability of the potential model rather than the approximations in the simulation methods which usually determines the success of the simulation. Thus the inclusion of all the important interatomic interactions, and then the subsequent derivation of the appropriate parameters is critical in determining the outcome of the simulation.

The short-range interaction and shell model parameters are obtained using a least squares fitting procedure. Parameters are adjusted until agreement between experimental and calculated crystal properties is achieved. Cohesive energies, lattice constants, elastic constants and dielectric constants constitute the data which is used for the fitting procedures (see, Lewis 1985). The parameters are first derived for the component binary oxides and then applied, in a direct transferable manner, to the system of interest. This approach to deriving a potential energy function has yielded many encouraging results (see for example, Price et al. 1987; Catlow and Mackrodt 1982) and is preferred to the alternative methods: the modified electron gas approach (Gordon and Kim 1972) and the ab-initio quantum mechanical methods (Lasaga and Gibbs 1987). In Chapter Five we will discuss the possibility of deriving potential energy surfaces from all electron Hartree-Fock calculations.

This concludes the discussion of potential energy of a crystal structure. The next section deals with the kinetic contribution to the total energy of the dynamical system of a crystal lattice. The first model presented is the classical Newtonian approach which is the MDS technique.

2.2 The molecular dynamics simulation model

The idea of MDS is the straightforward numerical solution of Newton's equations of motion for a system of particles or ions. The computer stores the positions and velocities of a number of particles in a fictitious "box" at a given time, and from a given model for the forces acting between the different particles, the changes in the set positions and velocities are calculated. Newton's equations are continuous in time but the simulation uses an integration algorithm to calculate the discrete changes in the dynamic variables over a small given time interval. This process is repeated iteratively for several thousand timesteps, and effectively the simulation generates the trajectories of the particles in time. The accuracy of the trajectories depends upon how realistic the force (potential) model is and the size of the timestep used. The smaller the timestep the closer one tends to the

continuous evolution of the system in time. Hence, starting from a given configuration of particle coordinates and velocities, the simulation generates the trajectory of the entire ensemble through the phase space spanned by the dynamic variables of all the particles in a completely deterministic way. Conditions such as the density of the system and the temperature can easily be imposed during an initial equilibration stage of the simulation.

In the MDS code used for the work presented in this thesis (called QCTPMD, written and donated by Prof. Masanori Matsui), Newton's laws of motion are solved numerically for the ensemble of particles or ions by the fifth-order predictor-corrector algorithm developed by Gear (1971), and calculates the new positions and velocities of each ion for each timestep increment. The code initially assigns a random set of positions and velocities for each ion in order to start the algorithm. To obtain the subsequent positions and hence velocities, the force law is required for the ensemble of atoms. For a set of N particles which have coordinates $\mathbf{r}_i$, velocities $\dot{\mathbf{r}}_i$ and masses m_i (where i = 1,....,N), the potential energy function is given by:

$$\phi(\mathbf{r}_{ij}) = U_C + U_{SR}, \tag{2.6}$$

where $r_{ij} = | \mathbf{r}_{ij} | = | \mathbf{r}_i - \mathbf{r}_j |$ is the distance between the ith and jth atoms. To facilitate the computation of the Coulomb and dispersion interactions, respectively, the Ewald sum method and the convergence-acceleration technique (Williams 1971) are used. Newton's law of motion takes the following form:

$$m_i\ddot{\mathbf{r}}_i = \Sigma_{j\neq i} r_{ij}^{-1}(d\phi/dr_{ij})\mathbf{r}_{ij}, \qquad i = 1,....,N. \tag{2.7}$$

The MDS code is based upon a microcanonical ensemble treatment (N,Ω,E) of a crystal structure, where N is the number of atoms or ions, Ω is the volume and E is the energy. This is a statistical ensemble where the brackets (....) denote the quantities which remain constant. A constant volume simulation severely restricts the number of problems one can study, specifically, phase transitions of crystal

structures. Hence, Andersen (1980) developed a constant pressure method for the statistical ensemble (N,H,P) where H is the enthalpy and P is the applied pressure. Parrinello and Rahman (1981) extended this method to study crystal structures of any symmetry and this provides the foundation for the model which is used in the MDS code. An outline of the essential equations which constitutes the MDS model is now given.

It is useful to adopt the Lagrangian formulation to treat the microcanonical ensemble and the general Lagrangian can be expressed as the sum of the kinetic and potential energy of the system:

$$\mathcal{L} = 1/2\ \Sigma_i m_i |\ r_i\ |^2 - 1/2\ \Sigma_{ij}\phi_{ij}(r_{ij}). \tag{2.8}$$

Parrinello and Rahman (1981) have proposed a Lagrangian for the study of microcanonical ensembles of particles where the size and shape of the MDS cell is allowed to vary with an externally applied hydrostatic pressure. This is easily extended to consider a general external stress (see Parrinello and Rahman 1981) but will not be discussed here. It is worth noting that the Lagrangian has not been derived from first principles and its validity is to be judged from the equations of motions and statistical ensembles that it generates. The Lagrangian is expressed as:

$$\mathcal{L} = 1/2\ \Sigma_{i=1}^{N} m_i \dot{s}_i' G \dot{s}_i - \Sigma_{i=1}^{N} \Sigma_{j>i}^{N} \phi(r_{ij}) + 1/2\ W(Tr\dot{h}'\dot{h}) - P\Omega, \tag{2.9}$$

where P is the hydrostatic pressure, **h** is a matrix whose columns are, in order, the components of the MDS cell vectors; **a**, **b** and **c** which completely define the size and shape of the cell by their lengths and mutual orientations. Hence, the volume of the cell is given by:

$$\Omega = \|\ \mathbf{h}\| = \mathbf{a}\cdot(\mathbf{b}\times\mathbf{c}), \tag{2.10}$$

where **a**, **b** and **c** are assumed to for a right-handed triad. The position $\mathbf{r}_i$ of the ith particle can be reexpressed in terms of **h** and of a column vector $\mathbf{s}_i$ as:

$$\mathbf{r}_i = \mathbf{h}\mathbf{s}_i = \alpha_{1i}\mathbf{a} + \alpha_{2i}\mathbf{b} + \alpha_{3i}\mathbf{c}, \tag{2.11}$$

where α_{1i}, α_{2i} and α_{3i} are in the range between 0 and 1, and i = 1,....N. If the prime ´ denotes the transpose of a vector or tensor then the square of the distance between i and j ions can be written as:

$$r_{ij}^2 = (\mathbf{s}_i - \mathbf{s}_j)'\mathbf{G}(\mathbf{s}_i - \mathbf{s}_j), \tag{2.12}$$

where the metric tensor **G** is:

$$\mathbf{G} = \mathbf{h}'\mathbf{h}. \tag{2.13}$$

In reciprocal space the vectors are defined as:

$$2\pi/\Omega\{\mathbf{bxc}, \mathbf{cxa}, \mathbf{axb}\} \equiv (2\pi/\Omega)\sigma, \tag{2.14}$$

where the matrix $\sigma \equiv \Omega\mathbf{h}'^{-1}$ carries information concerning the size and orientation of the MDS cell and is subject to the usual periodic conditions. The parameter W in equation 2.9 has dimensions of mass and will be further discussed later. From the proposed Lagrangian the equations of motion are found to be:

$$\ddot{\mathbf{s}}_i = -\Sigma_{j\neq i} m_i^{-1}(\phi'/r_{ij})(\mathbf{s}_i - \mathbf{s}_j) - \mathbf{G}^{-1}\dot{\mathbf{G}}\dot{\mathbf{s}}_i, \qquad i=1,...,N, \tag{2.15}$$

$$W\ddot{\mathbf{h}} = (\pi - P)\sigma, \tag{2.16}$$

where, using the dyadic notation, and writing $\mathbf{v}_i = \mathbf{h}\dot{\mathbf{s}}_i$:

$$\Omega\pi = \Sigma_i m_i \mathbf{v}_i\mathbf{v}_i - \Sigma_i\Sigma_{j>i}(\phi'/r_{ij})\mathbf{r}_{ij}\mathbf{r}_{ij}. \tag{2.17}$$

When the MDS cell is time independent, **h** = constant and $\dot{\mathbf{G}} = 0$. From equation 2.11 we see that equations 2.15 and 2.7 become equivalent. The average pressure

is calculated from 1/3 of the trace of the average of π. Equation 2.16 allows the system to be driven by the dynamic imbalance between the externally applied pressure and the internally generated stress tensor, hence, the equation allows one to study nonequilibrium phenomena which are driven by these imbalances. In a state of equilibrium, making the external stress have an oscillatory time dependence will also one to study frequency dependant response of the system to external stimuli of various kinds. From equation 2.16 it also follows that the mass W determines the relaxation time for recovery from an imbalance between the external pressure and the internal stress. Andersen's (1980) suggestion for the value of W is such that the relaxation time is of the same order of magnitude as the time L/c, where L is the MDS cell size and c is the velocity of sound. This eliminates the arbitrariness in the choice of W and makes the calculation more realistic.

From equation 2.9 one can construct the corresponding Hamiltonian following the usual rules of mechanics. Since the system is not subject to time dependent forces the Hamiltonian is a constant and is given by:

$$H = \Sigma_i 1/2 m_i v_i^2 + \Sigma_i \Sigma_{j>i} \phi(r_{ij}) + 1/2 W(Tr\dot{\mathbf{h}}'\dot{\mathbf{h}}) + P\Omega. \qquad (2.18)$$

In equilibrium at temperature T, the equipartition of energy theorem gives $(9/2)k_BT$ contribution from the term containing W and $(3N/2)k_BT$ from the other kinetic terms. Therefore to an accuracy of 3:N one finds that the constant in motion is simply the enthalpy:

$$H = E + P\Omega, \qquad (2.19)$$

where the total energy is given by:

$$E = \Sigma_i 1/2 m_i v_i^2 + \Sigma_i \Sigma_{j>i} \phi(r_{ij}). \qquad (2.20)$$

Hence, the Lagrangian in equation 2.9 generates, as stated previously, a constant pressure, enthalpy and number of ions (P,H,N) ensemble.

We have seen from the above treatment how the potential model is used in the solution of Newton's laws of motion to calculate the enthalpy of a number of particles in a "box" which are at a given temperature and applied pressure. Other elastic and thermodynamic parameters can be calculated from the variation of volume and enthalpy with changing pressures and temperatures. The heat capacity at constant pressure is given by:

$$C_P = (\partial H/\partial T)_P. \tag{2.21}$$

The thermal expansion coefficient and isothermal bulk modulus can be defined, respectively, as:

$$\alpha = V^{-1}(\partial V/\partial T)_P \tag{2.22}$$

$$K_T = - V(\partial P/\partial V)_T, \tag{2.23}$$

where V is the volume at pressure P and temperature T. It is now possible to show how the heat capacity at constant volume is related to the heat capacity at constant pressure:

$$C_P = C_V + TV\alpha^2K_T, \tag{2.24}$$

where the final term in the above expression is known as the anharmonic contribution. Anharmonicity will be discussed later in section 2.2.2.

From simulations of a crystal structure at different pressures and temperatures it is possible to obtain the above thermodynamic and elastic properties by performing linear interpolations on enthalpy-temperature, volume temperature and volume-pressure plots. These properties may be derived in MDS studies using the fluctuation formulae, however for certain MDS conditions (which will be employed later) they show rather large uncertainties (see, Nosé and Klein 1983).

2.2.1 Quantum corrections to the MDS model

At absolute zero temperature quantum theory predicts a non-zero energy for the crystal structure and this is called the zero-point energy. This result directly contradicts classical physics which relates the motion of the ions in the crystal structure to the temperature, hence, predicting zero energy at absolute zero temperature. The reason for the zero-point energy is that the ions have to possess a non-zero momentum so that it is not possible to know the position and velocity precisely and violate Heisenberg's uncertainty principle.

The classical mechanics description of atoms in a solid is only approximately valid at temperatures considerably above the Debye temperature. To estimate the quantum contribution to the structural, elastic and thermodynamic properties our code employs the Wigner-Kirkwood expansion (see for example, Landau and Lifshitz 1958; Hansen and Weis 1969; Matsui 1989) of the free energy in powers of Planck constant h. The corrections include only the first nonvanishing term having the order h^2, and neglect all higher-order terms. When the crystal potential energy is taken as the sum of pairwise interactions, as in equation 2.6, the quantum correction to the Helmholtz free energy, F, per formula unit (quantum minus classical is denoted by Δ) is expressed as (see, Hoover et al. 1969; Barker et al. 1971):

$$\Delta F = (E_0/T)\langle \Sigma_i m_i^{-1} \nabla_i^2 U \rangle$$

$$= (E_0/TZ)\langle \Sigma_i \Sigma_j m_i^{-1} (\phi_{ij}'' + 2\phi_{ij}' r_{ij}^{-1}) \rangle, \qquad (2.25)$$

where E_0 is $h^2/(96\pi^2 k)$, k is Boltzmann constant, m_i is the mass of the ith ion, U = ϕ_{ij} is the crystal potential energy per formula unit (see equation 2.6), ∇_i^2 is the Laplacian with respect to the coordinates of the ith ion, Z is the number of formula units per basic cell, and the angle brackets denote averages over the classical ensemble. Here the summation over i includes the ions in one basic cell, and j is summed over all atoms in the crystal except i=j.

The quantum corrections to the pressure P, the isothermal bulk modulus K_T, the heat capacity at constant pressure C_P, and the product of K_T and the thermal expansion coefficient α are obtained from differentiating ΔF with respect to volume V and/or temperature T. the results are:

$$\Delta P = -[\partial(\Delta F)/\partial V]_T = - E_0/(3TVZ)\{\langle\Sigma_i\Sigma_j m_i^{-1}(\phi_{ij}'''r_{ij} + 2\phi_{ij}'' - 2\phi_{ij}'r_{ij}^{-1})\rangle$$

$$- (2kTZ)^{-1} \times [\Sigma_i\Sigma_j m_i^{-1}(\phi_{ij}'' + 2\phi_{ij}'r_{ij}^{-1}) \times \Sigma_i\Sigma_j(\phi_{ij}'r_{ij})\rangle$$

$$- \langle\Sigma_i\Sigma_j m_i^{-1}(\phi_{ij}'' + 2\phi_{ij}'r_{ij}^{-1})\rangle \times \langle\Sigma_i\Sigma_j(\phi_{ij}'r_{ij})\rangle]\}, \qquad (2.26)$$

$$\Delta K_T = V[\partial^2(\Delta F)/\partial V^2]_T = E_0/(9TVZ)\{\langle\Sigma_i\Sigma_j m_i^{-1}(\phi_{ij}''''r_{ij}^2 - 8\phi_{ij}'' + 8\phi_{ij}'r_{ij}^{-1})\rangle$$

$$- (2kTZ)^{-1}[\langle\Sigma_i\Sigma_j m_i^{-1}(\phi_{ij}'''r_{ij} + 2\phi_{ij}'' - 2\phi_{ij}'r_{ij}^{-1}) \times \Sigma_i\Sigma_j(\phi_{ij}'r_{ij})\rangle$$

$$- \langle\Sigma_i\Sigma_j\, m_i^{-1}(\phi_{ij}'''r_{ij} + 2\phi_{ij}'' - 2\phi_{ij}'r_{ij}^{-1})\rangle \times \langle\Sigma_i\Sigma_j(\phi_{ij}'r_{ij})\rangle]\}, \qquad (2.27)$$

$$\Delta C_P = - T[\partial^2(\Delta F)/\partial T^2]_P \qquad \text{as } P \to 0$$

$$= - 2\Delta F/T, \qquad (2.28)$$

$$\Delta(\alpha K_T) = - [\partial^2(\Delta F)/\partial T\partial V]_{VT} = [\partial(\Delta F)/\partial V]_T/T$$

$$= - \Delta P/T. \qquad (2.29)$$

Finally, the quantum correction to α is obtained using equations 2.27 and 2.29 as $\Delta\alpha = [\Delta(\alpha K_T) - \alpha\Delta K_T]/K_T$, and the correction to V is calculated using ΔP as $\Delta V = (V/K_T)\Delta P$.

2.2.2 Anharmonicity and the MDS model

Previously, it was shown in Figure 2.1 how the distribution of potential energy varies between two neighbouring ions. At low temperatures the ions in the crystal structure vibrate about their equilibrium positions with small displacements. The curve at and around the equilibrium separation can be accurately approximated by a symmetrical parabola which is referred to as the harmonic approximation because the solutions to the dynamical equation for the ion are sinusoidal.

When the temperature of the crystal structure is increased the vibrations of the ions are more energetic and the displacements increase. The harmonic approximation is no longer valid for such conditions and the solutions to the dynamical equation are anharmonic (ie. includes overtones) due to the asymmetry of the potential energy distribution. This high temperature effect is known as anharmonicity and is included in the MDS treatment of a crystal structure by sampling the actual potential energy distribution and derivatives with respect to increasing interatomic spacing. This is transparent from equations 2.6, 2.15 and 2.17. Harmonicity and quasi-harmonicity will be further discussed in section 2.3.1.

2.3 The lattice dynamics simulation (LDS) model

The kinetic contribution in the LDS model is from treating the motions of the atoms or ions in a crystal structure as waves or, as they are commonly called, lattice vibrations. The LDS technique is often referred to as a semi-classical approach because the lattice vibrations are quantised (also called phonons) but the analysis of the dynamics of the atoms or ions utilises Newton's laws of motion. This approach was pioneered by Born and Huang (1954) and calculates the vibrational frequencies in periodic structures. We now discuss the main equations which constitute the LDS model.

In the Born model of solids one assumes that the net interacting forces are

described by interatomic potentials. From the previous section we see that the total potential energy is given by:

$$U_T = U_C + U_{SR} + U_P + U_B. \tag{2.30}$$

All the vibrational, elastic and thermodynamic properties calculated in the LDS model depends upon realism of the potential model. Also, the main assumption in the LDS model is the quasi-harmonic approximation which treats the vibrational motions of the atoms or ions in the crystal structure as independent quantized harmonic oscillators whose frequencies vary with cell volume. This will be discussed in greater detail, along with anharmonicity, thermal expansion and the Grüneisen parameter, in the next section.

The prediction of crystal structures and other temperature dependant crystal properties first requires the calculation of internal stress caused by the vibration of the constituent atoms. As stress is equal to the derivative of free energy with respect to volume, and the free energy at a given volume can be evaluated directly from the phonon frequencies, the first step is to determine the frequencies. These are calculated using a prescription elucidated by Cochran (1977) for the above shell model potential. The equations of motion to be solved are:

$$m d^2\mathbf{u}/dt^2 = dU_T/d\mathbf{u}, \tag{2.31}$$

where **u** is the displacement of the core and m its corresponding mass. In the case of the massless shells we have the condition:

$$0 = dU_T/d\mathbf{w}, \tag{2.32}$$

where **w** is the shell displacement, corresponding to zero net forces on the shells. The potential energy is expanded to second order with respect to ion displacements, i.e., the harmonic approximation:

$$U_T(\mathbf{r}') - U_T(\mathbf{r}) = 1/2(\mathbf{W_{uu}}\cdot\mathbf{u}\cdot\mathbf{u} + \mathbf{W_{uw}}\cdot\mathbf{u}\cdot\mathbf{w} + \mathbf{W_{wu}}\cdot\mathbf{w}\cdot\mathbf{u} + \mathbf{W_{ww}}\cdot\mathbf{w}\cdot\mathbf{w}), \quad (2.32)$$

assuming the unit cell is at equilibrium and $\mathbf{W_{uu}}$ represents the second derivative matrix between cores, $\mathbf{W_{uw}}$ between core and shell and $\mathbf{W_{ww}}$ between shells.

Finally, before solving for the derivatives with respect to core and shell displacements, the periodic nature of the solid must be considered by including the dependence of atomic displacements on the wave-vector **q**, i.e.,

$$\mathbf{u} = \mathbf{u}\exp(i(\mathbf{q}\cdot\mathbf{r} - \omega t)) \quad (2.33)$$

and

$$\mathbf{w} = \mathbf{w}\exp(i(\mathbf{q}\cdot\mathbf{r} - \omega t)), \quad (2.34)$$

where **r** is the atom position and ω the vibrational frequency. The second derivative or force constant matrix is similarly affected. For example, the force constant matrix for the interactions involving only shells is given by:

$$\mathbf{S} = \mathbf{W}\exp(iq(\mathbf{r_a} - \mathbf{r_b})), \quad (2.35)$$

which is summed over all ions $\mathbf{r_b}$. Similar expressions are obtained for the core-shell (**T**) and the core-core (**R**) matrices. Hence we can now solve the equations of motion 2.30 and 2.31 from equation 2.32 to get:

$$\omega^2\mathbf{m}\cdot\mathbf{u} = \mathbf{R}\cdot\mathbf{u} + \mathbf{T}\cdot\mathbf{w}, \quad (2.36)$$

and

$$0 = \mathbf{T}\cdot\mathbf{u} + \mathbf{S}\cdot\mathbf{w}, \quad (2.37)$$

where **m** is the diagonal matrix of core masses. Removing the shell displacements

w by substituting 2.36 and 2.37 gives:

$$\omega^2 \mathbf{m}\cdot\mathbf{u} = (\mathbf{R} + \mathbf{T}\cdot\mathbf{S}^{-1}\cdot\mathbf{T})\cdot\mathbf{u}. \tag{2.38}$$

Finally, by defining the dynamical matrix **D** as:

$$\mathbf{D} = \mathbf{m}\cdot(\mathbf{R} - \mathbf{T}\cdot\mathbf{S}^{-1}\cdot\mathbf{T})\cdot\mathbf{m}, \tag{2.39}$$

and

$$\mathbf{u} = \mathbf{m}\cdot\mathbf{n}, \tag{2.40}$$

to give

$$\omega^2 \mathbf{n} = \mathbf{D}\cdot\mathbf{n}, \tag{2.41}$$

which is now the eigen-vector problem and hence the frequencies can be calculated by diagonalising the dynamical matrix. However, the phonon frequencies are dependant on the wave-vector, i.e. phonon dispersion, thus to determine the phonon density of states we need to calculate the frequencies over all possible wave-vectors.

The need to calculate the frequencies for all wave-vectors is overcome in part by determining only those frequencies on a three-dimensional mesh of points within the Brillouin zone, using an appropriate weighting factor. The weighting will depend on the number of times a point appears in the Brillouin zone, thus the zone centre **q** = (0,0,0) which appears only once will have a weighting factor of one, while **q** = (0.5,0.5,0.5) for an orthorhombic crystal will have a weighting factor of eight. Fortunately the thermodynamic properties converge rapidly with the size of the mesh for temperatures above 50 K. The failure at very low temperatures is because acoustic phonons with wave-vectors close to the zone centre are the only thermally excited modes, therefore we need a fine mesh in this region to determine

correctly the phonon frequencies and hence the thermodynamic properties. This may be overcome by using "uneven sampling" techniques (see, Baldereschi 1973; Chadi and Cohen 1973; Filippini et al. 1976) which give an appropriate weighting to wave-vectors near the zone centre. Brillouin zone sampling will be discussed in greater detail in the next chapter.

Once the phonon frequencies have been determined for point within the irreducible Brillouin zone we can calculate the thermodynamic functions E, S, F and C_V i.e., the vibrational energy, entropy, free energy and heat capacity at constant volume, respectively, using the appropriate weighting factors. They are determined from the following expressions for a set of harmonic oscillators:

$$E = kT\Sigma_i^M (x/2 + x/(e^x - 1), \tag{2.42}$$

$$S = k\Sigma_i^M (-\ln(1 - e^{-x}) + x/(e^x - 1)), \tag{2.43}$$

$$F = kT\Sigma_i^M (x/2 + \ln(1 - e^{-x})), \tag{2.44}$$

$$C_V = k\Sigma_i^M (x^2e^x)/(e^x - 1)^2, \tag{2.45}$$

where each is summed over the total number of phonon frequencies, M, and where $x = h\omega_i/kT$. The zero-point energy $\Sigma_i h\omega_i/2$ is also included in the vibrational energy and free energy. In addition it is possible to calculate the density of states from the phonon frequencies within a small finite frequency interval where the total number of modes is 3n, (n being number of atoms in the unit cell).

The kinetic pressure P_K is simply the derivative of vibrational free energy with respect to volume. Thus for an isotropic material:

$$P_K = dF/dV, \tag{2.46}$$

and is determined by calculating the free energy at a given volume and then

recalculating after making a small adjustment to the cell volume dV. If the calculation is at desired hydrostatic pressure P_H then the difference between P_K and P_H needs to be minimised by iterative changes in volume where the free energy and, hence, vibrational frequencies are recalculated for each iteration. The calculations involve the utilisation of static simulation routines for constant temperature (Norgett and Fletcher 1970) and constant pressure (Catlow and Norgett 1976; Parker and Price 1989), and details of these routines will not be given here. The calculation, as stated previously, is based upon the quasi-harmonic approximation and this is the topic for discussion in the next section. A further analysis of anharmonicity and its implications for the LDS model, thermal expansion and the Grüneisen parameter are also discussed.

2.3.1 Quasi-harmonicity, anharmonicity, thermal expansion and the Grüneisen parameter.

The harmonic approximation neglects higher than second order terms in the expansion of the potential energy about the equilibrium separation between neighbouring atoms in the crystal structure. The most important consequences of the approximation are:

a) there is no thermal expansion;
b) the force constants and hence the elastic constants are independent of temperature and pressure;
c) the heat capacity becomes constant at high temperatures;
d) the specific heats measured at constant pressure and constant volume are equal: $C_P = C_V$;
e) since there are no collisions between phonons, their mean free paths and lifetimes are infinite;
f) as a consequence of (e), a perfectly harmonic crystal would have an infinite thermal conductivity;
g) the line widths of the infrared absorption peaks and of the Raman, Brillouin and

inelastic scattering peaks are zero for perfectly-ordered harmonic crystals.

In real crystals none of these consequences are satisfied accurately.

We have seen how the kinetic contribution to the total energy of a crystal can be evaluated from the frequencies of the lattice vibrations. These calculations are performed by the computer code PARAPOCS (Parker and Price 1989) at the quasi-harmonic level of approximation. In this approximation the frequencies of the lattice vibrations are a function of volume, however after each volume increment the frequencies are recalculated assuming that the atoms or ions are independent quantized harmonic oscillators. This approach accommodates thermal expansion but still neglects the nonlinear coupling of phonons. We see from equation 2.24 that the heat capacities at constant pressure and constant volume are no longer equal, and at high temperatures one would expect a linear dependence of C_V with temperature but this is not the case because in the quasi-harmonic approximation the specific anharmonic term is not included in the calculation of the free energy (see, Brüesch 1982).

The asymmetric form of the crystal potential energy is the cause for thermal expansion (see Figure 2.2). As the temperature of the crystal increases so do the vibrations of the atoms. The interatomic separation oscillates between r_1 and r_2, with $r_2 - r_e > r_e - r_1$, that is the extension of the bond is greater than its compression. In addition, the restoring force (i.e. the negative of the slope of the curve) is smaller on the extension side, so that, on average, the bond spends a longer time in extension than in compression. The mean value of the bond length becomes longer than the equilibrium value at low temperature: $r_1 + r_2 > 2r$, hence the crystal expands. One can also see from Figure 2.2 that if a pressure is applied at constant temperature in order to decrease the crystal spacing, the restoring force increases more rapidly than in the harmonic case: compression becomes more and more difficult, that is, the bulk modulus increases with pressure.

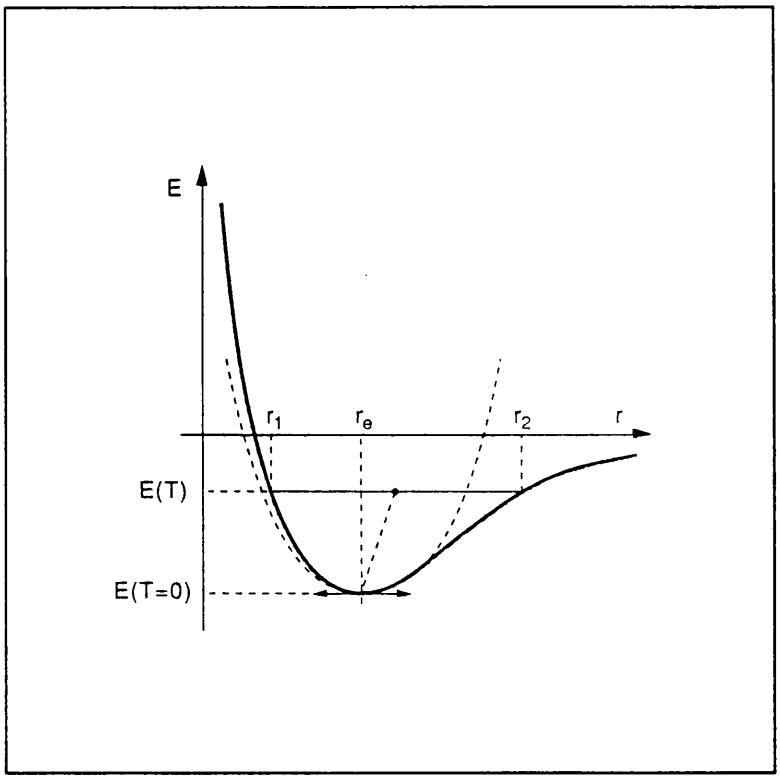

Figure 2.2 Thermal expansion. At T=0 K, the interatomic potential is minimum for the equilibrium distance r_e. At a finite temperature, the potential E(T) is higher and due to the asymmetric shape of the anharmonic curve, the equilibrium distance is the average between r_1 and r_2, which is greater than r_e. For a symmetrical harmonic potential (dashed curve) there would be no thermal expansion. (After Poirier, 1991)

Thermal expansion coefficient can be calculated in two ways using PARAPOCS. The first method measures the crystal structure at two finite temperatures, and the change in volume is calculated (see equation 2.22). This is analogous to the experimental technique using dilatometers where small changes in volume are measured on heating (see, White et al. 1985). Alternatively, the following thermodynamic relation can be used:

$$\beta = \gamma C_V/K_T V = \gamma C_P/K_S V, \qquad (2.47)$$

where V is the molar volume, K_S is the adiabatic bulk modulus and γ is the thermal Grüneisen parameter.

The thermal or average Grüneisen parameter is found from calculating the mode Grüneisen parameters which are defined as:

$$\gamma_i(q) = -V/\omega_i(q)\cdot[d\omega_i(q)/dV], \tag{2.48}$$

and provide an explicit measure of the variation of vibrational frequencies with volume. Hence, the average Grüneisen parameter is given by (see, Kieffer 1982):

$$\gamma = 1/C_V\Sigma_i(C_V)_i\cdot\omega_i, \tag{2.49}$$

where $(C_V)_i$ is the contribution to the heat capacity made by each mode, i (see equation 2.45). From the above definitions we see that the Grüneisen parameter provides a good measure of anharmonicity. The quasi-harmonic approximation only takes into account the effect of thermal expansion, and this can be viewed as taking account of "extrinsic" contribution of anharmonicity. We now discuss the consequences of "intrinsic" anharmonicity.

If a crystal is held at a fixed volume and the temperature is increased then all the energy goes into the thermally excited phonons or lattice vibrations, assuming there is no heat loss. Up to now we have assumed that the phonon is equivalent to an independent lattice vibration which is similar to a normal mode or standing wave. In other words, the vibration is distributed instantaneously over the whole crystal structure and, as stated earlier, leads to an infinite thermal conductivity. Obviously, the instantaneous distribution of energy in the form of lattice vibrations does not allow for the transport of heat (i.e. energy) and is only applicable to equilibrium conditions."Far from equilibrium" states such as the flow of seismic waves from earthquakes require a treatment where the phonon lifetime is not infinite (see, Reissland 1973; Brüesch 1982). This also implies a "far from equilibrium" thermodynamics for the study of macroscopic properties (see,

Prigogine and Stengers 1984).

When treating "intrinsic" anharmonicity the expansion of the potential energy with respect to interatomic separation is taken to higher than second order terms. This expression is then placed in the anharmonic Hamiltonian for the solution of Schrödinger's equation for a set of quantum anharmonic oscillators. The solution to this equation is very complex because there is coupling between the equations of each oscillator leading to non-linear effects. Brüesch (1982), Reissland (1973) and Ball (1989) all contain some aspects of the mathematical analyses of the anharmonic crystal and we refer the interested reader to these texts. We will merely state some results of the anharmonic problem which have a relevance for our context.

At high temperatures C_v increases linearly with temperature, that is, there is a positive deviation from the Dulong-Petit limit. The vibrational frequencies of the mode of vibrations in the crystal decrease with increasing temperature (see, Gillet et al. 1991) and hence, Grüneisen parameters for the variation with temperature and pressure can be defined. Hardy (1980) investigated the variation of the derivatives of the crystal potential energy, ϕ, with respect to the interatomic spacing and defined a dimensionless parameter λ as:

$$\lambda = \phi'''(R)X_{rms}/\phi''(R), \tag{2.50}$$

where R is the mean distance between nearest neighbours and X_{rms} is the root mean square value of the ionic displacements due to thermal motion. This parameter provides a measure of the anharmonic effects relative to the harmonic approximation. The second and third derivatives $\phi''(R)$ and $\phi'''(R)$ are the major parameters determining the size of harmonic and of cubic anharmonic effects, respectively. The equipartition theorem allows X_{rms} to be estimated with the formula:

$$(1/2)CX_{rms}^2 = (1/2)kT, \tag{2.51}$$

where C is a typical value for the harmonic force constants. It is roughly proportional to $\phi''(R)$. When the attractive part of the potential ($\phi_A(r) = -A/r$ where r is the distance between ions) is neglected in relation to the repulsive part ($\phi(r) = B/r^n$ where n is between 7 and 12 for ionic solids), the second derivative $\phi''(R)$ is proportional to $1/R^{n+2}$, so that X_{rms}^2 is proportional to TR^{n+2}. The third derivative $\phi'''(R)$ is proportional to $1/R^{n+3}$, so that the ratio λ is proportional to:

$$(1/R^{n+3})(TR^{n+2})^{1/2}R^{n+2} = (TR^n)^{1/2}. \qquad (2.52)$$

Hence, the relative magnitude of anharmonic to harmonic effects depends upon the product TR^n. Since the mean distance R decreases as pressure increases, it follows from equation 2.52 that T must be increased to keep the value of λ constant as pressure is increased. Therefore, the temperature at which anharmonicity has the same relative magnitude increases as pressure increases. In other words, at high temperatures the anharmonic treatment (MDS model) should tend to the quasi-harmonic approximation (LDS model) as pressure is increased. It is precisely this hypothesis which is tested in Chapter Four.

2.4 Concluding remarks

We have seen the similarities and differences between the MDS and LDS models. In Chapter Three we present the results of a rigorous test of the potential model for the LDS approach. The modelling of oxygen isotope equilibria up to 1000 K temperatures for a variety of silicate minerals was chosen as a suitable stringent probe because the reactions between the minerals involve small exchanges of energy.

CHAPTER THREE

A COMPUTER SIMULATION APPROACH TO MODELLING THE STRUCTURE, THERMODYNAMICS AND OXYGEN ISOTOPE EQUILIBRIA OF SILICATES

3.0 Introduction

With the advent of powerful supercomputers, much effort has been put into the modelling of crystal structures and the calculation of their associated lattice dynamic and thermodynamic properties (see for example, Parker and Price 1989; Catlow and Mackrodt 1982). It has been clearly demonstrated that from a microscopic treatment of periodic systems, accurate macroscopic properties can be calculated (see for example, Kieffer and Navrotsky 1985; Price et al. 1987). The study presented in this chapter is not only an extension of previous work of Price et al. (1987), but also a rigorous test of the methodology employed. As described in the previous chapter, our approach is based upon the atomistic or Born model of solids, in which potential functions represent the interactions between atoms in a structure. We have used potentials which were previously fitted (Lewis and Catlow 1985) either to the physical properties of binary oxides or to quantum mechanical energy surfaces, and contain terms to describe three-body interactions (Sanders et al. 1984) as well as oxygen-oxygen and cation-oxygen short-range interactions. These potentials have been successfully used in the past to model phase relations between magnesium silicates (Parker and Price 1989). In this chapter we test the precision and transferability of the potentials by comparing, for a wide range of silicates, our calculated structural, elastic and bulk thermodynamic properties with existing experimental data. Whereas in previous studies (see, for example, Wall and Price 1988; Price et al. 1987) simple high-symmetry silicate structures have been investigated, here we also look at silicates with framework, chain and low symmetry structures (albite, diopside, α-quartz and wollastonite) as

well as the higher symmetry forsterite and pyrope. We also take the prediction of thermodynamic properties to its very limit by investigating the effect that oxygen isotope substitution has on the physical properties of the silicates and also studying a highly subtle reaction, namely that of oxygen isotope partitioning. The successful simulation of this process should prove a most stringent test for any modelling technique.

In the following sections we discuss the input for the LDS code PARAPOCS, the problem of sampling the Brillouin zone to obtain representative estimates of thermodynamic properties, our calculated results which include structural data (such as lattice parameters, cell volume, bond lengths and bond angles), elastic constants, bulk moduli, mode Grüneisen parameters and other thermodynamic data (such as thermal expansion coefficients, heat capacities and entropies). We devote the penultimate sections to the discussion of the above mentioned stable isotope effects and oxygen isotope partitioning, giving a brief summary of the theory involved and how it relates to lattice dynamics. A detailed comparison of our results with those determined experimentally is also presented, along with a discussion of the problems arising from the experiments. Finally, we give our conclusions, outlining the geophysical implications of this work, and discuss the successes and limitations of our model.

3.1 Data input to PARAPOCS

In this study we modelled the following silicates; albite, diopside, forsterite, pyrope, α-quartz and wollastonite. These were chosen, not only for their geological importance, but also because the necessary component potentials were available to perform an accurate simulation. The availability of experimental data was also a contributing factor for our selection.

PARAPOCS requires the orthogonalised coordinates of each ion in the whole unit cell. These are calculated from the processing of the experimental x-ray

diffraction coordinates of the asymmetric cell through an orthogonalisation routine. Note that in the shell model we treat a core ion and a shell ion of the same species (see section 2.3) and so the shell coordinates are also input with initially the same values as the core ions. The magnitude of the lattice vector, L, is determined by the longest lattice parameter of the unit cell (in angstroms). The orthogonalisation routine provides a lattice vector rotation matrix which is input prior to the coordinates.

Our calculations are performed for a perfect lattice (i.e. no defects or vacancies) and based on a fully ionic potential model. Hence, the mass and full ionic charge is input for each species of ion contained in the unit cell of the crystal structure. We have applied the shell model to the oxygen atom only in our studies and so the oxygen core ion is assigned a small positive partial charge and all the mass, whilst the shell ion contains the resulting negative charge to make the species fully ionic and zero mass (see section 2.3). The potential parameters used for each component interaction (see equations 2.2, 2.3 and 2.5) are presented in Table 3.1. The short-range potential cut-off varied between 0.9 for forsterite and pyrope and 1.9 for α-quartz. However, it is usual to take of value of 1.1L. A maximum core-shell separation of 0.1L was used for all the silicates. All the minerals with the exception of forsterite were modelled with a three-body O - Si - O interaction term and albite with an extra O - Al - O term. The maximum deviation from the initial bond angle from equilibrium was set at 20.0° and the bond lengths were within the constraints of 0 to 1.76Å for the bond O - Si and 0 to 2.70Å for the O - O bond. For the O - Al - O group we set the limits to 0 to 1.9Å for the O - Al bond and 0 to 3.0Å for the O - O bond.

Table 3.1 Potential parameters used for silicates

Interaction	Potential Parameters			Ref.
	A/eV	ρ/Å	C/eVÅ^{-6}	
O^{2-} - O^{2-}	22764.0	0.1490	27.8800	1
Si^{4+} - O^{2-}	1283.9	0.3205	10.6616	1
Al^{3+} (6-fold) - O^{2-}	1114.9	0.3118	0.0	2
Al^{3+} (4-fold) - O^{2-}	1460.3	0.2991	0.0	3
Mg^{2+} - O^{2-}	1428.5	0.2945	0.0	2
Ca^{2+} - O^{2-}	1090.4	0.3437	0.0	2
Na^{+} - O^{2-}	1226.8	0.3065	0.0	4
	k/eVrad^{-2}			
O^{2-} - Si^{4+} - O^{2-}	2.097			1
O^{2-} - Al^{3+} - O^{2-}	2.097			1
	k/eVÅ^{-2}			
O^{2-} core-shell	79.9204			1

Note: 1 Sanders et al. 1984; 2 Lewis and Catlow 1985; 3 James 1979; 4 Catlow et al. 1984

The maximum magnitude of the phonon wavevector was given the value of L for all the silicates. The number of points sampled in reciprocal space was determined by taking the number of species in the unit cell into consideration. The arrays within PARAPOCS are set as high as possible so that we are able to cover as much of the dispersion curve as allowed within the given computational

constraints. However, this is the major limitation of the program and we are restricted to 8 points sampled in the Brillouin zone for large unit cells such as pyrope. A more detailed investigation of Brillouin zone sampling is given in the next section.

3.2 Brillouin Zone Sampling

Because phonon frequencies vary as a function of the wavevector **q**, it is essential, in order to calculate bulk thermodynamic properties, to evaluate phonon vibrational frequencies across the whole Brillouin zone. However, because of computational constraints, it is not practical to sample the entire zone, therefore, special sampling procedures must be used. Efficient sampling of the first Brillouin zone is essential for economizing computer time, although the best method for achieving this is not obvious. In the past there have been a variety of approaches to Brillouin zone sampling, such as the use of special-point sets (Chadi and Cohen 1973), mean-value points (Baldereschi 1973) and sampling points on a general grid (Filippini et al. 1976). We have performed calculations using all these methods, and have compared their efficiency and accuracy.

The general grid sampling methods investigated were based on a scheme used by Filippini et al. (1976). They point out that the amount of phonon dispersion is generally greatest near the Brillouin zone centre and, therefore, more dense sampling is required in this region. This is achieved by dividing the first Brillouin zone into a set of boxes, each containing one sampling point at its centre, with an edge length of the i^{th} box given by:

$$x_i = 0.5\ (2^{(i-1)})/(2^n-1), \qquad (3.1)$$

where n is the cube root of the number of points sampled. The co-ordinates of the i^{th} point are:

$$0.5(2^{(i-1)}-1)/(2^n-1) + 0.5(2^{(i-1)})/\{2(2^n-1)\}. \quad (3.2)$$

In obtaining the density of states, the eigenvalues ($\omega^2(\mathbf{q})$) calculated at each reciprocal lattice wave vector ($\mathbf{q}$) are weighted by a factor M which varies according to the size of the box, thus:

$$M = 2^{(i+j+k-3)}, \quad (3.3)$$

where i, j, k = 1 to n. Thus, even though the Brillouin zone is sampled more densely near the centre, these frequencies do not make a contribution that is out of proportion to the total frequency sum.

Filippini et al.(1976) studied the effects of three progression formulae similar to (3.1) and found that the best convergency was given by the following equation:

$$x_i = [n_i/3+n_i^2]^{1/3}, \quad (3.4)$$

where n_i = 1, 2, 3 .....etc. They also noted that it is only necessary to sample the Brillouin zone in an asymmetric sector. The symmetry conditions and the size of the sector sampled depend upon the point group of the cell.

We have used the two progression formulae (3.1) and (3.4) in a sampling procedure, which tested the convergency of the zero-point energy (ZPE) and the heat capacity at constant volume. We see from equations 2.42 and 2.45 that the ZPE and C_V are dependant on the summation of the frequencies and hence the number of modes sampled and therefore, the consistency and convergency of the predicted values should provide an adequate test of the various sampling procedures. By choosing the ZPE as a testable parameter we have included a function which is independent of the density of states and therefore not prone to the errors accumulated from such a term.

The results of our calculations for the $MgSiO_3$-ilmenite structure, which has a space group of $R\bar{3}$, are shown in Table 3.2a. Each set of calculations are internally self-consistent, and all the calculated heat capacities, irrespective of the details of the sampling process, are within 0.08 $Jmol^{-1}K^{-1}$ of each other. The zero-point energies differ by a maximum of 0.0024eV within each sampling procedure and we see for equations 3.1 (+ ve octant only) and 3.4 (all octants) the convergency is very good. Increasing the number of sampling points does not affect the convergency in a consistent manner, therefore, it is difficult to see an overall trend. Uncertainties of +/- 0.002eV and +/- 0.08 $Jmol^{-1}K^{-1}$ were, however, considered to be an acceptable limit in our study, and so for the remaining part of our work we used progression formula 3.1, against which we compared the special point sampling methods outlined below.

In an attempt to minimise the computational time spent sampling the Brillouin zone, Baldereschi (1973) defined the concept of a mean-value point to be a point at which the value assumed by any given periodic function of the wave vector is an excellent approximation to the average value of the same function throughout the Brillouin zone. The approach of using a mean-value point would be most valuable in studying a high-symmetry structure, that contains a large number of atoms. Thus we chose to compare the results obtained with the Baldereschi (1973) mean-value point with those of the grid-method in the study of garnet pyrope. Pyrope ($Mg_3Al_2Si_3O_{12}$) has 160 atoms in its body-centred cubic cell, and therefore would represent a considerable computational challenge. We tested the efficiency and accuracy of the mean-value point ($2\pi/a(1/6,1/6,1/2)$) for this lattice (Baldereschi 1973) by comparing the result obtained from using the special point to the grid point set in equation 3.1. The values calculated are given in Table 3.2b, and it can be seen that the agreement is excellent, even though the mean-value point method only used one-eighth of the cpu time. Unfortunately, mean-value points are of most use for cubic cells, so we chose not to pursue this method any further as we were to study lower symmetry structures.

Table 3.2a The predicted values of zero-point energy and C_V for ilmenite at 300 K with varying Brillouin zone sampling techniques

Sampling Equation	N_S[1]	ZPE/eV	C_V/Jmol^{-1}K^{-1}
3.1[2]	8	0.4650	79.0404
	27	0.4653	79.0164
	64	0.4654	79.0100
3.1[2]	5	0.4637	79.0314
	14	0.4633	79.0722
	30	0.4625	79.0851
3.1[3]	5	0.4651	78.9890
	14	0.4641	79.0324
	30	0.4639	79.0008
3.4[2]	5	0.4546	79.1820
	14	0.4548	79.1788
	30	0.4543	79.2236
3.4[3]	5	0.4608	79.2206
	14	0.4626	79.1559
	30	0.4632	79.1420

[1] Number of points sampled in reciprocal space; [2] + ve octant only; [3] all octants

Table 3.2b The predicted zero-point energies and heat capacities for pyrope and α-quartz for a variety of Brillouin zone sampling procedures

Mineral	Sampling Equation	N_s[1]	ZPE/eV	C_V/Jmol^{-1}K^{-1}
Pyrope (T = 100 and 300 K)	Mean-value point	1	1.8281	83.7804
		1	1.8250	323.0976
	3.1	8	1.8286	83.6086
		8	1.8255	324.7778
α - Quartz (T = 100 K)	Special-point	6	0.2993	15.5402
		12	0.2993	15.5419
		24	0.2993	15.5419
	3.1	8	0.2993	15.5207
		27	0.2992	15.5508
		64	0.2992	15.5616

1 The number of points sampled in reciprocal space

Chadi and Cohen (1973) extended the work of Baldereshi (1973) by calculating a set of special sampling points for cubic and hexagonal Bravais lattices. We tested this approach on α-quartz which has a trigonal crystal structure. The results are again shown in Table 3.2b. Agreement with the grid point sets of equation 3.1 is again excellent. Both heat capacities are converging from below, and differ by less than 1 per cent of each other.

Although a few discrepancies in our calculations did arise, we did not feel that a deeper analysis was required, as our initial question (i.e. what is the most efficient method for sampling the Brillouin zone) had been answered to the level of accuracy we required. For the sake of self-consistency and convenience, therefore, we used the grid point sets of equation 3.1 as our sampling method for the analyses described below. In the next section we discuss the structural, elastic and thermodynamic results obtained for a number of silicates using this approach.

3.3 Predicted Structural, Elastic and Thermodynamic Properties.

In this section we present the structural data predicted for albite, diopside, forsterite, pyrope, α-quartz and wollastonite, and discuss the comparability of these data with experimental values. Similar discussions are subsequently presented for their predicted elastic and thermodynamic data.

Table 3.3 shows the observed and predicted values (T=300K) for the lattice parameters and cell volume of the silicates studied. We see that the agreement with the experimental data on the whole is excellent, with the largest error in predicted cell volume being for albite (6.2%) due to a less than perfect Na-O potential, and the lowest being 1.2% for α-quartz. Significantly, the nature of the monoclinic and triclinic distortions of albite, diopside and wollastonite are all very well predicted. The average bond lengths and average bond angles for the low symmetry structures are given in Table 3.4 and once again the agreement with experimental data is very good. This reflects the excellent agreement between individual calculated bond lengths and bond angles and those observed. It should be noted that Si-O-Si angles are well reproduced without recourse to using a Si-O-Si angle dependant term in our potential model. Table 3.5 shows the results for the elastic constants and bulk moduli at a temperature of 300K. Agreement with the experimental data is again good, but the predicted values are systematically overestimated. Our predicted values for the average mode Grüneisen parameter and thermal expansion coefficient (at T=300K) is shown in Table 3.6.

Table 3.3 Predicted and observed lattice parameters and cell volume

		Lattice Parameters						Unit cell Volume
		a	b	c	α	β	γ	
Albite	ob[1]	8.14	12.79	7.16	94.19	116.61	87.98	664.48
	pr	8.48	12.91	7.15	91.23	115.77	87.93	706.06
Diopside	ob[2]	9.75	8.92	5.25		105.86		439.13
	pr	9.84	9.04	5.26		105.33		451.37
Forsterite	ob[3]	4.75	10.19	5.98				289.58
	pr	4.79	10.29	6.00				296.09
Pyrope	ob[4]	11.46						1504.70
	pr	11.34						1459.80
α-Quartz	ob[5]	4.91	4.91	5.40				113.01
	pr	4.89	4.89	5.39				111.65
Wollastonite	ob[6]	7.93	7.32	7.07	90.06	95.22	103.43	396.96
	pr	8.02	7.44	7.13	92.76	92.76	103.91	412.55

Note: Units; a, b and c are in Å; α, β and γ are in degrees; Unit cell volume, $Å^3$; References: 1 Harlow and Brown (1980), 2 Levien and Prewitt (1981), 3 Fujino et al. (1981), 4 Novak and Gibbs (1971), 5 LePage et al. (1980), 6 Ohashi (1984); T=300K

Table 3.4 Predicted and observed average bond angles and average bond lengths for albite, diopside and wollastonite.

		Albite[1]	Diopside[2]	Wollastonite[3]
O - Si -O	ob	109.44	109.32	109.25
	pr	109.39	108.26	109.19
Si - O - Si	ob	144.74	135.79	143.53
	pr	142.10	135.35	145.25
O - O	ob	2.68	2.66	2.63
	pr	2.65	2.73	2.65
Si - O	ob	1.61	1.64	1.62
	pr	1.61	1.64	1.63
Ca - O	ob		2.50	2.39
	pr		2.57	2.44
Mg - O	ob		2.08	
	pr		2.09	
Al - O	ob	1.74		
	pr	1.74		
Na - O	ob	2.55		
	pr	2.81		

Note: Units: Bond angles/° Bond lengths/Å;

References: 1 Harlow and Brown (1980); 2 Levien and Prewitt (1981); 3 Ohashi (1984)

Table 3.5 Elastic constants and bulk moduli for the silicates studied

	Albite		Diopside		Forsterite		Pyrope		α-Quartz		Wollastonite	
	pr	ob[NA]	pr	ob[1]	pr	ob[2]	pr	ob[3]	pr	ob[4]	pr	ob[NA]
C_{11}	0.71		2.03	2.23	1.99	2.00	3.79	2.95	0.96	0.87	1.67	
C_{22}	1.91		1.68	1.71	2.73	2.36	3.79	2.95	0.96	0.87	0.96	
C_{33}	1.50		2.80	2.35	3.49	3.29	3.79	2.95	1.11	1.06	1.97	
C_{44}	0.12		0.68	0.74	0.72	0.67	1.04	0.90	0.50	0.58	0.45	
C_{55}	0.37		0.57	0.67	0.81	1.04	1.04	0.90	0.50	0.58	0.43	
C_{66}	0.43		0.68	0.66	0.40	0.81	1.04	0.90	0.42	0.40	0.41	
C_{12}	0.45		0.91	0.77	0.84	0.67	1.19	1.17	0.13	0.07	0.63	
C_{13}	0.38		0.80	0.81	0.88	0.63	1.19	1.17	0.17	0.12	0.55	
C_{23}	0.21		0.67	0.57	0.92	0.73	1.19	1.17	0.17	0.12	0.43	
K_S	0.69		1.25	1.08	1.50	1.29	2.06	1.77	0.44	0.37	0.37	

Note: Units: Mbar; References: 1 Levien et al. (1979), 2 Suzuki et al. (1983), 3 Leitner et al. (1980), 4 McSkimin et al. (1965); NA = Not Available

Table 3.6 Predicted and observed average Grüneisen parameter and thermal expansion coefficient at T = 300 K

	Average Grüneisen parameter		Thermal expansion coefficient	
	γ_{pr}	γ_{ob}	β_{pr}	β_{ob}
Albite	0.612	NA	1.734	NA
Diopside[1]	0.784	NA	1.534	3.0
Forsterite[2]	1.087	1.335	1.895	2.8
Pyrope[3]	1.099	1.050	1.579	1.9
α-Quartz[3]	0.513	0.670	2.354	3.5
Wollastonite[4]	0.628	NA	1.493	0.6

Note: Units β $10^{-5}K^{-1}$; References: 1 Finger and Ohashi (1976); 2 Matsui and Manghnani (1985); 3 Anderson (1989); 4 Weston and Rodgers (1976); NA = Not available

Table 3.7 Predicted and observed heat capacities and entropies

	T/K	C_P		S	
		ob	pr	ob	pr
Albite[1,6]	100	81.66	81.95	54.30	51.73
	300	205.10	207.18	207.40	206.11
	500	262.61	265.57	328.97	327.60
	700	290.69	291.78	422.27	421.67
	1000	312.34	309.27	530.04	529.18
Diopside[2]	100	52.40	54.97	4.27	5.00
	300	167.40	166.58	143.70	147.00
	500	213.70	209.77	241.70	243.94
	700	234.00	228.16	317.20	317.89
	1000	248.19	240.44	402.90	401.74
Forsterite[3]	100	32.26	33.08	1.77	2.08
	300	119.10	116.90	94.85	95.08
	500	148.30	148.40	163.90	163.50
	700	161.70	161.70	216.10	215.90
	1000	175.10	171.10	276.20	275.50
Pyrope[1,4]	100	94.27	83.68	42.48	33.39
	300	326.60	324.76	268.28	251.51
	500	419.28	418.85	455.57	443.19
	700	455.19	458.23	603.22	591.25
	1000	473.89	485.05	769.54	759.94
Note: Continued overleaf					

Table 3.7 Continued

	T/K	C_P		S	
		ob	pr	ob	pr
α-Quartz[5,7]	100	15.70	15.57	9.69	8.95
	300	44.78	45.46	41.74	41.28
	500	59.68	60.01	68.45	68.39
	600	65.04	63.94	79.82	79.71
Wollastonite[2,*]	100	97.32	101.73	51.81	55.60
	300	259.41	257.21	246.66	251.78
	500	321.58	317.09	396.30	399.44
	700	348.84	342.88	509.70	510.81
	1000	375.01	359.73	639.30	636.41

Note: Units: $Jmol^{-1}K^{-1}$; References: 1 Robie et al. (1978); 2 Krupka et al. (1985a and 1985b); 3 Robie et al. (1982); 4 Haselton and Westrum (1980); 5 Hemingway (1987); 6 Openshaw et al. (1976); 7 Gurevich and Khlyustov (1979); * 3 moles of $CaSiO_3$

The experimental data, where they exist are also shown, and we see that the comparability between observed and calculated values is poorer than for the structural parameters, possibly reflecting some previously noted (Price et al. 1987) minor shortcoming in the third derivative of the Si-O potential. Holland (1989) has recently studied empirically the volume dependency of entropy for silicate minerals, and his predicted entropies at 298K are in excellent agreement with experimental values, with average absolute deviations of $1.41 Jmol^{-1}K^{-1}$. Our calculated heat capacities and entropies (shown in Table 3.7) are also, on the whole, in very good agreement with experimental data, with average deviations of $2\text{-}3 Jmol^{-1}K^{-1}$. The low

temperature simulations for pyrope show quite considerable errors in the predicted entropies and heat capacities. This is an effect of limited sampling of the Brillouin zone where only eight points were sampled for pyrope, because of its large unit cell. The simulations for α-quartz were not carried out above 600K because the PARAPOCS code is based on the quasi-harmonic approximation and breaks down as a soft-mode or displacive phase transition is approached. Overall, the results from the simulations show excellent comparability with experimentally determined data. This success encouraged us to consider using these models to calculate the effects on the above and other physical properties from the result of the substitution of the oxygen atom by the heavier O^{18} isotope.

3.4 Equilibrium Isotope Effects of O^{18} Substitution

The above properties were all calculated for the silicates containing the O^{16} isotope. In this section we investigate the effects on the properties when the oxygen is substituted by its heavier isotope O^{18}. The nature of the substitutions that we are interested in is that the isotopes are stable, i.e. they have very long lifetimes, and the systems are in equilibrium. O'Neil (1986) quite correctly points out that the nature of the potential energy curve is unaffected by these substitutions because there is no change in the overall charge distribution. Therefore, it is purely the effect of the mass on the bond energy, and hence, the frequencies of the modes of vibration, that we are investigating. If X is any parameter then $X(O^y)$ denotes the parameter of the y-oxygen isotope silicate.

We begin by looking at the calculated cell volumes, V, which are presented in Tables 3.8a and 3.8b. We see from our results that the volumes increase with temperature as expected. On substitution of O^{18} the cell volume is slightly reduced. We saw in section 2.5 that the LDS model within the quasi-harmonic approximation converges at an equilibrium volume when the external hydrostatic pressure is equal to the vibrational (phonon) pressure.

Table 3.8a Predicted enthalpy, zero-point energy and cell volume for the O^{16} isotope silicates

	T/K	H/eV	ZPE/eV	$V_{cell}/Å^3$
Albite	100	-480.3026	1.2066	703.39625
	300	-479.9873	1.2056	706.06395
	500	-479.4885	1.2043	709.31780
	700	-478.9064	1.2029	712.86217
	1000	-477.9657	1.2008	718.49332
Diopside	100	-336.4300	0.8795	450.22583
	300	-336.1821	0.8785	451.36806
	500	-335.7849	0.8771	453.00551
	700	-335.3277	0.8754	454.83746
	1000	-334.5947	0.8729	457.81043
Forsterite	100	-211.8399	0.6165	295.20595
	300	-211.6714	0.6152	296.08591
	500	-211.3910	0.6133	297.43141
	700	-211.0673	0.6111	298.97665
	1000	-210.5467	0.6075	301.57901

Table 3.8a Continued

	T/K	H/eV	ZPE/eV	V_{cell}/Å^3
Pyrope	100	-672.3563	1.8286	1456.3472
	300	-671.8985	1.8255	1459.8174
	500	-671.1124	1.8209	1465.0342
	700	-670.1976	1.8157	1470.9786
	1000	-668.7240	1.8071	1480.7682
α-Quartz	100	-128.3439	0.2992	111.23262
	300	-128.2773	0.2989	111.65164
	500	-128.1659	0.2985	112.27541
	600	-128.1013	0.2982	112.61117
Wollastonite	100	-497.8345	1.2572	822.66896
	300	-497.4348	1.2561	825.10338
	500	-496.8298	1.2548	828.20069
	700	-496.1416	1.2534	831.45164
	1000	-495.0441	1.2514	836.27937

Table 3.8b Predicted enthalpy, zero-point energy and cell volume for the O^{18} isotope silicates

	T/K	H/eV	ZPE/eV	$V_{cell}/Å^3$
Albite	100	-480.3423	1.1651	703.34124
	300	-480.0177	1.1640	706.01837
	500	-479.5110	1.1628	709.27433
	700	-478.9237	1.1614	712.83294
	1000	-477.9784	1.1593	718.47101
Diopside	100	-336.4595	0.8488	450.17440
	300	-336.2038	0.8478	451.33200
	500	-335.8004	0.8464	452.98004
	700	-335.3396	0.8448	454.81739
	1000	-334.6033	0.8423	457.79514
Forsterite	100	-211.8599	0.5958	295.16504
	300	-211.6859	0.5946	296.06048
	500	-211.4013	0.5927	297.41380
	700	-211.0751	0.5905	298.96342
	1000	-210.5524	0.5870	301.56884

Table 3.8b Continued

	T/K	H/eV	ZPE/eV	V_{cell}/Å^3
Pyrope	100	-672.4172	1.7658	1456.1612
	300	-671.9426	1.7627	1459.6892
	500	-671.1438	1.7582	1464.9424
	700	-670.2213	1.7531	1470.9076
	1000	-668.7412	1.7447	1480.7148
α-Quartz	100	-128.3540	0.2887	111.19651
	300	-128.2850	0.2884	111.63119
	500	-128.1716	0.2880	112.26187
	600	-128.1065	0.2878	112.62381
Wollastonite	100	-497.8771	1.2125	822.59348
	300	-497.4664	1.2115	825.04779
	500	-496.8528	1.2102	828.16119
	700	-496.1591	1.2088	831.41923
	1000	-495.0568	1.2069	836.26035

If the mass of an ion is increased its vibrational frequency decreases (see equation 2.38) therefore the phonon pressure will subsequently be smaller. If the external pressure is the same the cell volume is reduced. However, this is not the case for α-quartz at T=600K where $V(O^{18})$ is larger than $V(O^{16})$. At this temperature α-quartz is approaching a transition to its β phase, therefore anharmonic effects are obviously significant. However, our model which is based on the quasi-harmonic approximation gives no suggestion that the anharmonic effects vary with mass at constant temperature and so it is not possible to explain the above exception along these lines. In Figures 3.1a and 3.1b we see the variation in the difference in cell volumes for the two isotopes with temperature. It is interesting to note that the trend of $V(O^{18})$-$V(O^{16})$ approaching zero is consistent for all the silicates. Yet again, this is difficult to explain via anharmonic effects but our results show a definite relationship between mass and intrinsic anharmonicity at constant temperature. Boyer (1981) has clearly demonstrated the shortcomings of the quasi-harmonic approximation by showing that the vibrational pressure is consistently overestimated at high temperatures. If the increase of mass of a constituent ion tends to increase the level of anharmonicity at that temperature then we would expect an overestimation in phonon pressure and, hence, cell volume for the O^{18} silicates at high temperatures, and this would account for the observed trends. Another trend we can observe from Figures 3.1a and 3.1b is that the magnitude of cell volume difference is dependant on the size of the unit cell of the silicate. Therefore, pyrope with the largest cell volume will give the greatest cell volume difference between its isotope members and, similarly, α-quartz the smallest.

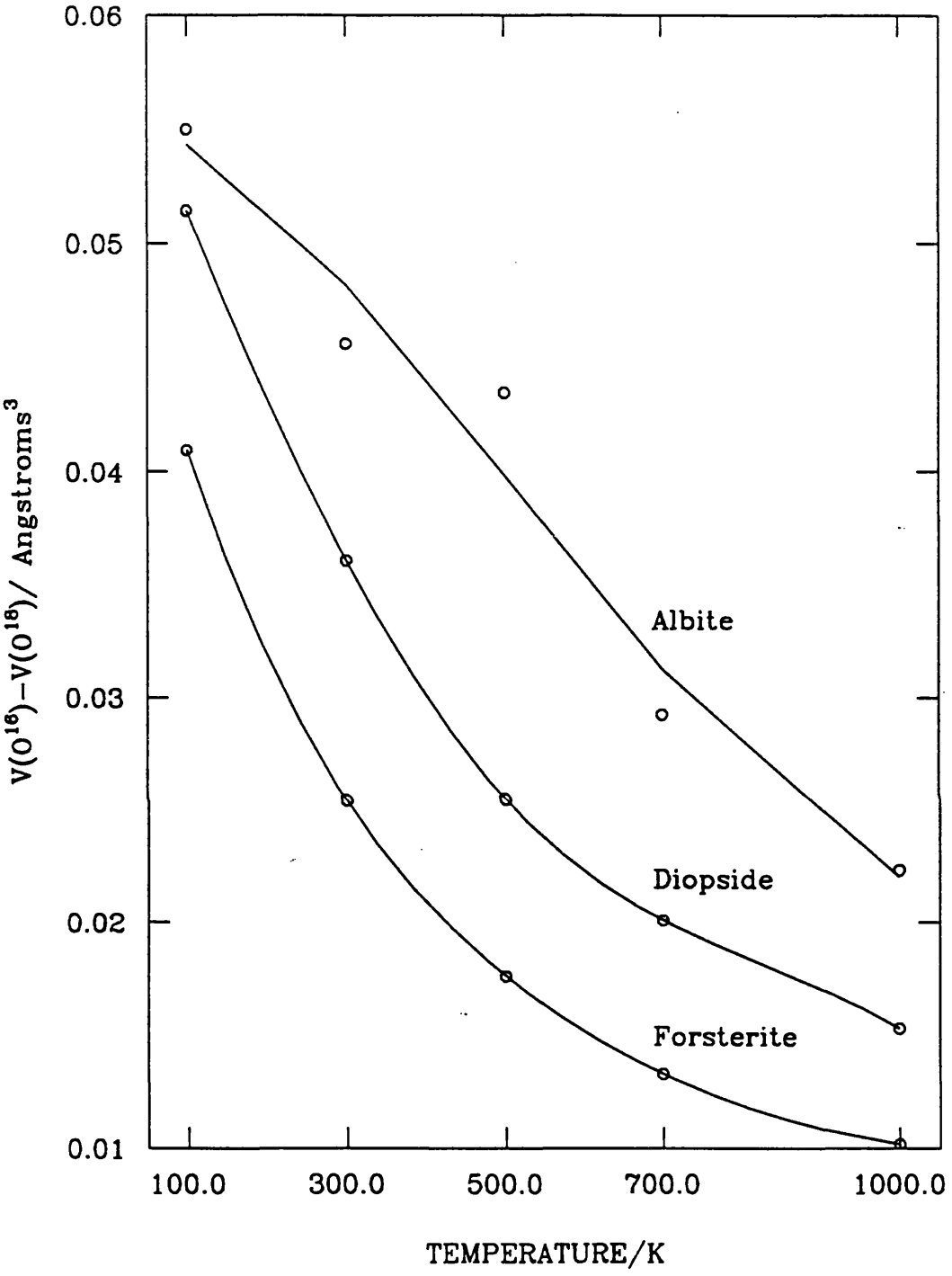

Figure 3.1a Isotopic volume differences vs. temperature for albite, diopside and forsterite

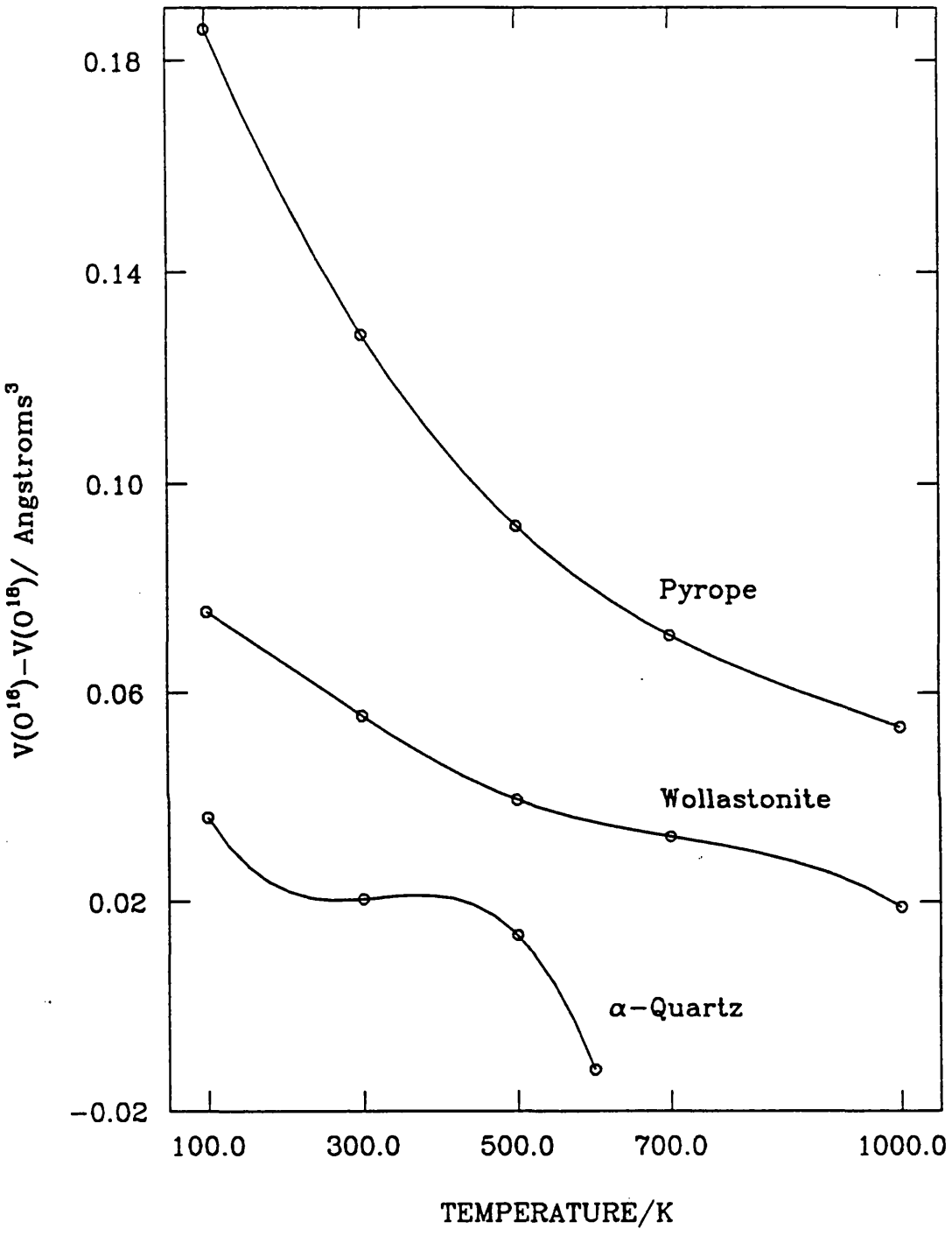

Figure 3.1b Isotopic volume differences vs. temperature for pyrope, α-quartz and wollastonite

We now turn our attention to the zero-point energies (ZPE) which are also listed in Tables 3.8a and 3.8b. There is a consistent decrease in ZPE for each silicate with increasing temperature and this would not be immediately obvious from inspection of equation 2.42 where the ZPE is shown to be independent of temperature. Nevertheless, we know there is a new volume for each new temperature and this can provide a clue for the understanding of the above trend. As the temperature is increased the unit cell expands giving an increase in the average interatomic separation, R. From equations 2.33 and 2.34 we see the real part of expression will decrease if R increases and subsequently the real frequencies will also decrease. Therefore, the summing of the ground state mode frequencies will be less than for lower temperatures. Also, the greater the number of modes (i.e. ions in the unit cell), the larger the ZPE. Pyrope with the largest number of ions in its unit cell has the largest ZPE, and correspondingly, α-quartz the smallest. The ZPE(O^{18}) is always less than the ZPE(O^{16}) because, as stated earlier, an increase in mass gives a decrease in frequency and, hence, sum of ground state frequencies. Figures 3.2a and 3.2b show the variation of ZPE(O^{16})-ZPE(O^{18}) with temperature. This property reduces with increasing temperature for all the silicates. Once again, this cannot be explained purely from the relationships in our model. In other words, the intrinsic anharmonic contributions to both O^{16} and O^{18} cases are not necessarily different.

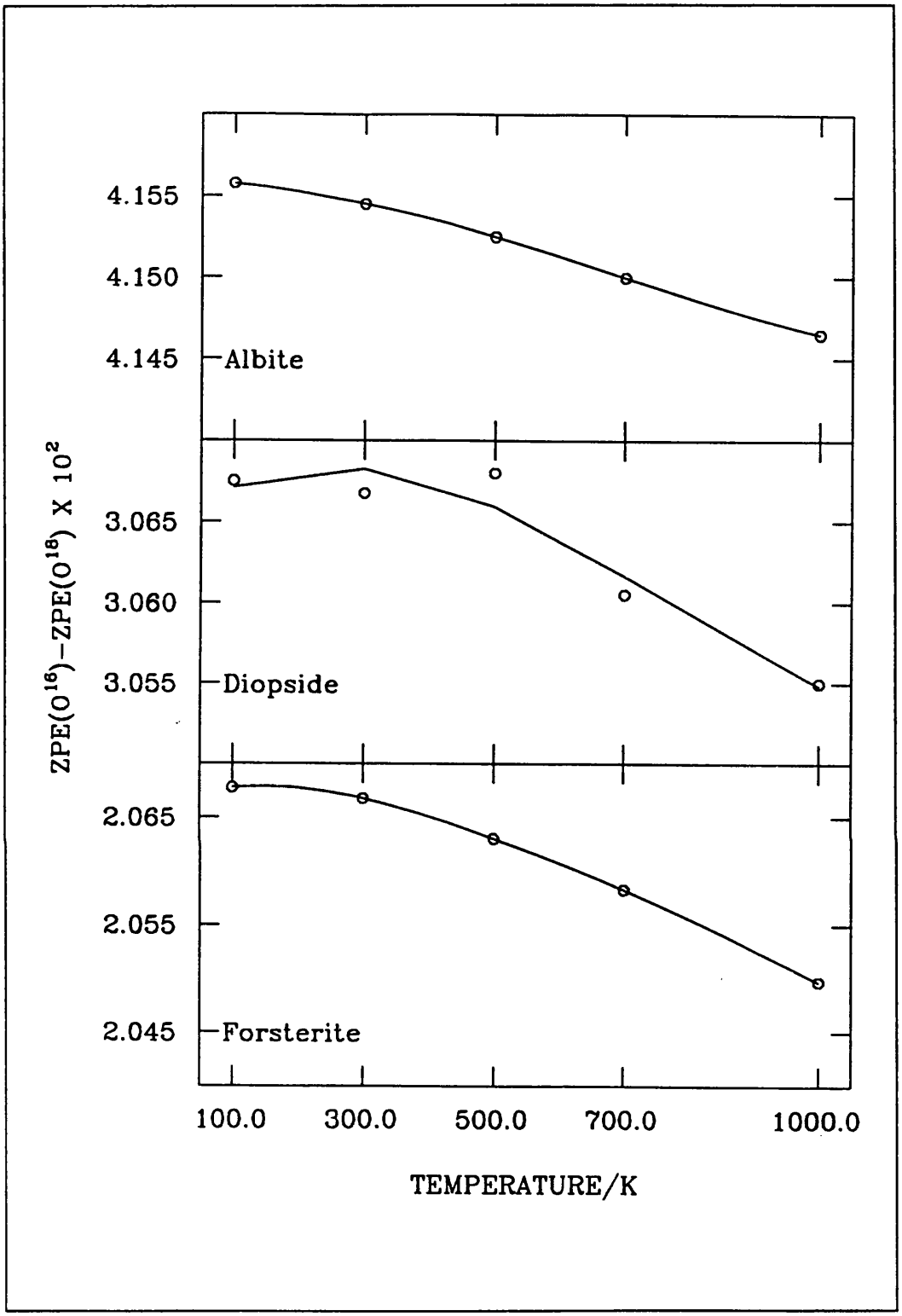

Figure 3.2a Isotopic zero-point energy differences against temperature for albite, diopside and forsterite

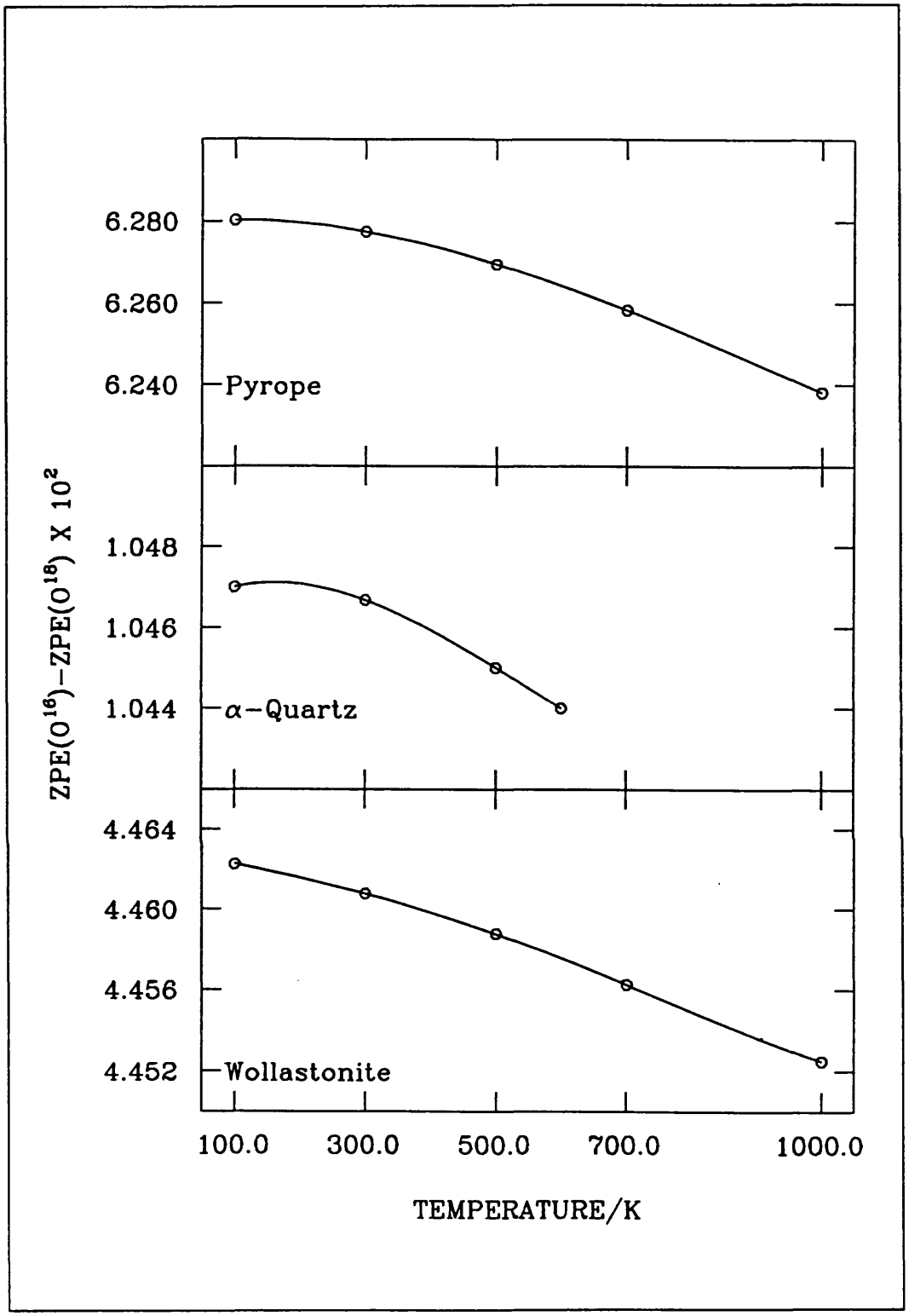

Figure 3.2b Isotopic zero-point energy differences against temperature for pyrope, α-quartz and wollastonite

The important thermodynamic quantity of heat capacity at constant volume, C_V, is directly related to the sum of the normal modes of vibration (see equation 2.45). The calculated values are presented in Tables 3.9a and 3.9b and we see that they increase with temperature as expected. The integrand (without the density of states function) in equation 2.45 tends to e^{-x} as x tends to infinity, implying that for a smaller x (i.e. smaller frequency at constant temperature) the calculated heat capacity would be larger. This is exactly what we discover for $C_V(O^{18})$ where a larger mass substituted gives smaller frequencies for the modes of vibration. Obviously, for a greater number of modes of vibration, the larger the heat capacity, but this does not explain why the difference in heat capacities, $C_V(O^{18})$-$C_V(O^{16})$, should also follow this correlation (see Figures 3.3a and 3.3b). In Debye theory, we see that the heat capacity approaches the Dulong-Petit limit of 3NR, where N is the number of atoms in the formula unit and R is the universal gas constant. Therefore, the increase in heat capacity will diminish at high temperatures, thus explaining the reduction in $C_V(O^{18})$-$C_V(O^{16})$ as the temperature increases. An interesting feature we see in Figures 3.3a and 3.3b is that the curves all have a maximum around 250 to 300K. This suggests that at this temperature:

$$d/dT(C_V(O^{18})-C_V(O^{16}) = 0 \qquad (3.5)$$

or

$$d/dT(C_V(O^{18})) = d/dT(C_V(O^{16})), \qquad (3.6)$$

where T is the temperature. Therefore, on the normalised heat capacity curves with temperature we should find the gradients of all silicates and both isotopes to be identical at the above specified temperature range. It would be interesting to see if experiment confirms this.

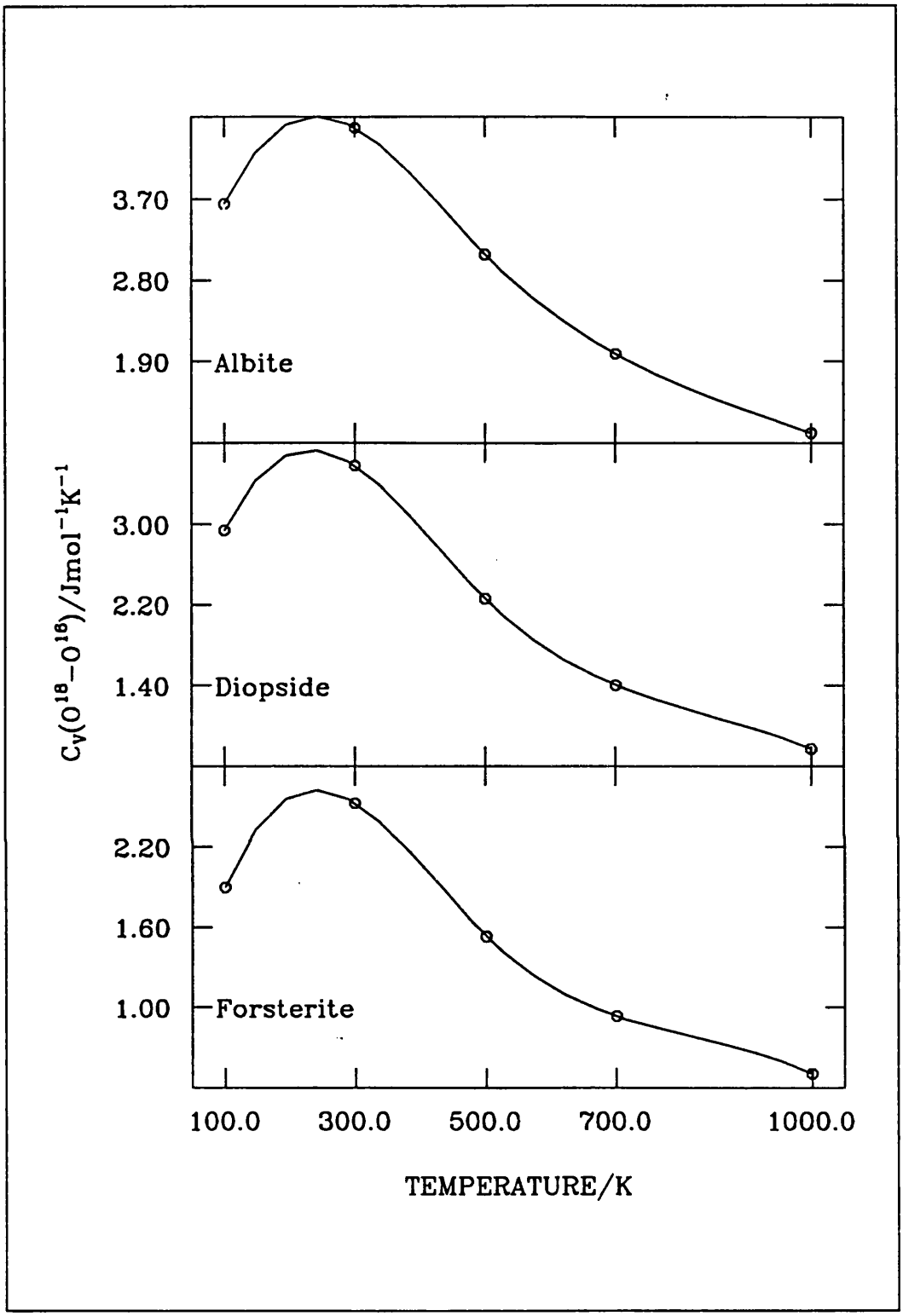

Figure 3.3a Isotopic heat capacity differences vs. temperature for albite, diopside and forsterite

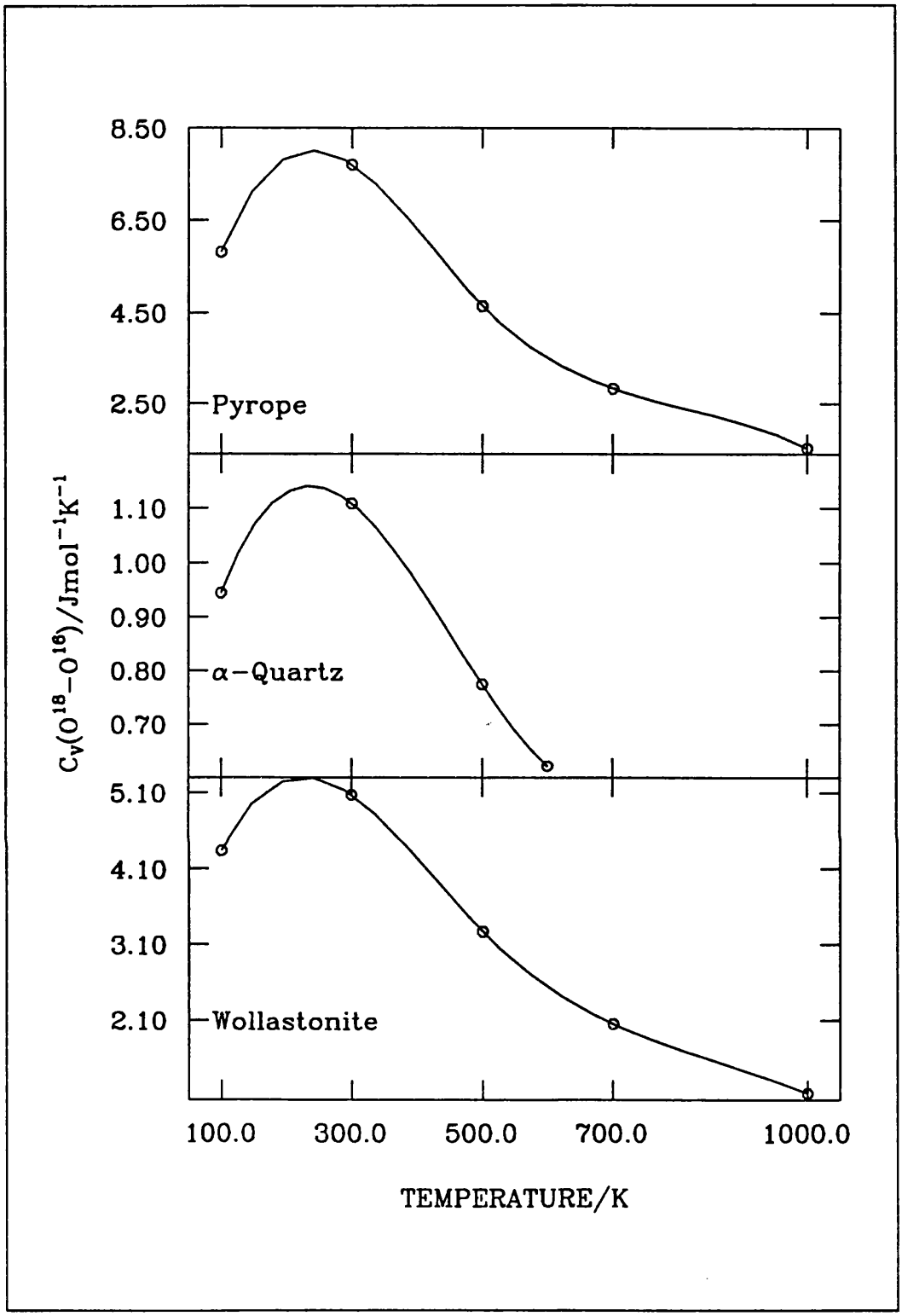

Figure 3.3b Isotopic heat capacity differences vs. temperature for pyrope, α-quartz and wollastonite

Table 3.9a Calculated lattice energies, Gibbs free energies and heat capacities at constant volume for the O^{16} silicates

	T/K	U_{LAT}/eV	G/eV	C_V/Jmol^{-1}K^{-1}
Albite	100	-481.5446	-480.3563	81.8532
	300	-481.5427	-480.6282	206.5180
	500	-481.5394	-481.1863	264.2432
	700	-481.5343	-481.9658	289.7440
	1000	-481.5233	-483.4506	306.1591
Diopside	100	-337.3292	-336.4580	54.9470
	300	-337.3278	-336.6393	166.0620
	500	-337.3249	-337.0490	208.5640
	700	-337.3204	-337.6341	226.2400
	1000	-337.3103	-338.7587	237.3660
Forsterite	100	-212.4672	-211.8547	33.0575
	300	-212.4657	-211.9671	116.2175
	500	-212.4622	-212.2383	146.7487
	700	-212.4563	-212.6337	158.9917
	1000	-212.4430	-213.4025	166.5643

Table 3.9a Continued

	T/K	U_{LAT}/eV	G/eV	C_V/ $Jmol^{-1}K^{-1}$
Pyrope	100	-674.2107	-672.3910	83.6080
	300	-674.2068	-672.6807	323.0940
	500	-674.1986	-673.4093	414.8600
	700	-674.1853	-674.4874	451.7880
	1000	-674.1554	-676.6007	474.6200
α-Quartz	100	-128.6494	-128.3532	15.5625
	300	-128.6490	-128.4056	45.2973
	500	-128.6482	-128.5204	59.6178
	600	-128.6476	-128.5972	63.4377
Wollastonite	100	-499.1314	-497.8923	101.6625
	300	-499.1296	-498.2178	256.4835
	500	-499.1262	-498.9000	315.6390
	700	-499.1212	-499.8478	340.7355
	1000	-499.1114	-501.6404	356.6790

Table 3.9b Calculated lattice energies, Gibbs free energies and heat capacities at constant volume for the O^{18} silicates

	T/K	U_{LAT}/eV	G/eV	C_V/Jmol^{-1}K^{-1}
Albite	100	-481.5446	-480.3991	85.4945
	300	-481.5428	-480.6829	210.9991
	500	-481.5394	-481.2594	267.3333
	700	-481.5343	-482.0601	291.7291
	1000	-481.5234	-483.5789	307.2693
Diopside	100	-337.3293	-336.4894	57.8870
	300	-337.3278	-336.6793	169.6390
	500	-337.3249	-337.1031	210.8220
	700	-337.3204	-337.7043	227.6410
	1000	-337.3103	-338.8544	238.1350
Forsterite	100	-212.4673	-211.8758	34.9510
	300	-212.4657	-211.9937	118.7424
	500	-212.4622	-212.2743	148.2789
	700	-212.4564	-212.6804	159.9227
	1000	-212.4430	-213.4662	167.0676

Table 3.9b Continued

	T/K	U_{LAT}/eV	G/eV	C_V/ $Jmol^{-1}K^{-1}$
Pyrope	100	-674.2108	-672.4549	89.4220
	300	-674.2070	-672.7607	330.8080
	500	-674.1988	-673.5172	419.5160
	700	-674.1855	-674.6275	454.6140
	1000	-674.1556	-676.7920	476.1460
α-Quartz	100	-128.6494	-128.3640	16.5072
	300	-128.6490	-128.4194	46.4049
	500	-128.6482	-128.5387	60.3921
	600	-128.6476	-128.6181	64.0587
Wollastonite	100	-499.1314	-497.9382	105.9990
	300	-499.1297	-498.2774	261.5490
	500	-499.1263	-498.9808	318.9045
	700	-499.1213	-499.9528	342.7830
	1000	-499.1114	-501.7839	357.8085

Also listed in Tables 3.9a and 3.9b are the static lattice energies, U_{LAT}. As temperature increases the lattice energies increase slightly, i.e. they become less negative. On inspection of equation 2.30, we see that the lattice energy is independent of temperature and so the effect we are picking up is from a change in volume. The Coulombic term (equation 2.1) has the greatest contribution to the lattice energy and it is easy to see that if the volume expands the average distances between ions will become larger giving a less negative electrostatic term. Note that in the Ewald sum, there are contributions from the interactions between like and unlike ions. However, the nearest-neighbour ions are usually oppositely charged species resulting in an overall negative Coulombic term. If the electrostatic component becomes less negative with increasing temperature then this is the dominant effect in the static lattice energy. The O^{18} isotope silicate gives a smaller volume, as discussed earlier, and therefore, a more negative lattice energy from the above reasoning.

We are now in a position to discuss the equilibrium isotope effects on enthalpy which are presented in Tables 3.8a and 3.8b. The positive terms of the vibrational energy and pressure-volume increase with temperature and so we observe the consistent trend of enthalpy becoming less negative. If the mass of an ion is increased, the vibrational energy is less positive, the lattice energy is more negative and the volume is smaller giving the overall effect of a more negative enthalpy for the O^{18} isotope silicates.

The average Grüneisen parameters, γ, are presented in Tables 3.10a and 3.10b and we see that they generally decrease with temperature. This is difficult to account for as there are opposing effects in the overall contribution to γ via equation 2.49.

Table 3.10a Predicted average Grüneisen parameter, isothermal bulk modulus and thermal expansion coefficient for the O^{16} isotope silicates

	T/K	γ	K_T/kbar	$\beta/x10^{-5}K^{-1}$
Albite	100	1.04639	694.75420	1.1640
	300	0.61257	685.92957	1.7348
	500	0.52360	675.74340	1.9171
	700	0.49664	664.88090	2.0164
	1000	0.48255	648.28372	2.1065
Diopside	100	0.77204	1178.78456	0.53103
	300	0.70513	1161.38329	1.4844
	500	0.65465	1137.51547	1.7614
	700	0.63844	1111.13622	1.9006
	1000	0.63379	1068.62531	2.0461
Forsterite	100	1.26065	1519.63181	0.61696
	300	1.08654	1494.47448	1.8952
	500	1.00938	1461.04051	2.2638
	700	0.99189	1423.84917	2.4603
	1000	1.00158	1362.08125	2.6972

Table 3.10a Continued

	T/K	γ	K_T/kbars	$\beta/x10^{-5}K^{-1}$
Pyrope	100	1.53774	2070.50921	0.56633
	300	1.09905	2046.32623	1.5789
	500	1.01476	2014.86397	1.8943
	700	0.99464	1980.50207	2.0488
	1000	0.99682	1925.51213	2.2040
α-Quartz	100	0.64836	443.69210	1.0185
	300	0.51306	440.47024	2.3541
	500	0.46492	436.34448	2.8184
	600	0.45255	434.26782	2.9238
Wollastonite	100	0.83013	880.74007	0.77355
	300	0.62786	868.07142	1.4932
	500	0.55680	852.75887	1.6528
	700	0.52582	836.85726	1.7101
	1000	0.49581	813.68006	1.7259

Table 3.10b Predicted average Grüneisen parameter, isothermal bulk modulus and thermal expansion coefficient for the O^{18} isotope silicates

	T/K	γ	K_T/kbar	$\beta/x10^{-5}K^{-1}$
Albite	100	1.00308	694.94330	1.1652
	300	0.60216	686.08459	1.7420
	500	0.51856	675.88858	1.9205
	700	0.49416	664.97352	2.0199
	1000	0.48131	648.35018	2.1085
Diopside	100	0.75414	1179.48048	0.54621
	300	0.69683	1161.87852	1.4980
	500	0.65067	1137.87305	1.7692
	700	0.63617	1111.41166	1.9052
	1000	0.63258	1068.83051	2.0484
Forsterite	100	1.24676	1520.38883	0.64488
	300	1.07333	1494.99407	1.9124
	500	1.00281	1461.42296	2.2720
	700	0.98813	1424.14296	2.4649
	1000	0.99948	1362.31475	2.6993

Table 3.10b Continued

	T/K	γ	K_T/kbars	$\beta/x10^{-5}K^{-1}$
Pyrope	100	1.48767	2071.33314	0.58583
	300	1.08466	2047.29964	1.5948
	500	1.00847	2015.28488	1.9034
	700	0.99115	1980.82435	2.0541
	1000	0.99497	1925.75294	2.2068
α-Quartz	100	0.65790	443.83168	1.0962
	300	0.51068	440.53915	2.4005
	500	0.46220	436.40117	2.8382
	600	0.45650	434.11693	2.9795
Wollastonite	100	0.80644	881.08227	0.78331
	300	0.61942	868.33522	1.5019
	500	0.55312	852.94725	1.6585
	700	0.52374	837.01259	1.7133
	1000	0.49487	813.76819	1.7279

Also listed in Tables 3.10a and 3.10b are the thermal expansion coefficients, β, which consistently increase with temperature. This is a consequence of the asymmetric potential energy curve (see Figure 2.3) where an increase in temperature results in an increase in the average interatomic separation. Hence, as we go higher up the potential well, the rate at which the volume expands also increases thus giving an increase in the thermal expansion coefficient. We stated at the beginning of this section that the potential energy distribution is not affected by a change in mass of an ion, therefore we would expect the rate of change of cell volume with respect to temperature to be similar for both oxygen isotope silicates. However, the volume for O^{18} silicate is smaller and so this would give a larger thermal expansion coefficient as $\beta = V^{-1}dV/dT$. This is precisely what is observed from our calculated results in Tables 3.10a and 3.10b.

The remaining property listed in Tables 3.10a and 3.10b is the isothermal bulk modulus, K_T. If we assume that the decrease of γ with temperature in negligible compared to the increase of C_V, β and V then we can see from inspection of equation 2.47 that K_T will decrease as the temperature increases. We can also observe that $K_T(O^{18})$ is consistently greater than $K_T(O^{16})$ (except for α-quartz at T=600K). On isotope substitution the effects to the properties in equation 2.47 are opposing, making it difficult to explain the definite trend.

With all the isotopic effects on the quantities that contribute to the anharmonic term (see equation 2.24) accounted for, it is now possible to look at the heat capacity at constant pressure. Our calculated values are presented in Tables 3.7 and 3.11. As the temperature rises the anharmonic term becomes more significant and C_P tends away from the Dulong-Petit limit. This is clearly observed for all silicates and, also, if we assume the product of βK_T is more dominant than the change in volume then this explains the fact that $C_P(O^{18})$ is greater than $C_P(O^{16})$ at any of the predicted temperatures.

Table 3.11 Predicted heat capacity and entropy for the O^{18} isotope silicates

	T/K	C_p/Jmol^{-1}K^{-1}	S/Jmol^{-1}K^{-1}
Albite	100	85.5946	54.6611
	300	211.6634	213.8825
	500	268.6645	337.3565
	700	293.7675	432.2565
	1000	310.3880	540.3281
Diopside	100	57.9110	28.7770
	300	170.1703	152.9140
	500	212.0358	251.3470
	700	229.5732	325.9150
	1000	241.2211	410.1420
Forsterite	100	34.9790	15.2880
	300	119.4739	98.9667
	500	149.9687	168.4305
	700	162.6492	221.2497
	1000	171.5749	281.1242

Table 3.11 Continued

	T/K	C_p/Jmol^{-1}K^{-1}	S/Jmol^{-1}K^{-1}
Pyrope	100	89.5000	36.2500
	300	332.5240	263.0840
	500	423.5420	457.9680
	700	461.0940	607.2900
	1000	486.6000	776.7440
α-Quartz	100	16.5189	9.6657
	300	46.5756	43.2195
	500	60.7881	70.8246
	600	64.5816	82.2678
Wollastonite	100	106.0665	58.8555
	300	262.2780	260.7840
	500	320.3670	410.6085
	700	344.9355	522.8700
	1000	360.8685	649.0215

The entropy is related to the integral of the heat capacity at constant pressure over temperature and so is directly proportional to the magnitude of C_P. This corresponds precisely with our calculated results (see Tables 3.7 and 3.11) and shows exactly the same trends as C_P.

Finally, to conclude this section we turn our attention to the Gibbs free energy, G, which were shown earlier in Tables 3.9a and 3.9b. The free energies become more negative with temperature because the entropic term rises rather steeply with increasing temperature. For the reason that the $S(O^{18})$ is greater than $S(O^{16})$, the $G(O^{18})$ is more negative than $G(O^{16})$. It is the Gibbs free energies we require to investigate the reaction of oxygen isotope fractionation between silicates.

3.5 Oxygen Isotope Partitioning.

Isotope partitioning is important geologically because it can reveal information about the temperature of formation of rocks in the Earth's crust and mantle. In this section we discuss the reasons for the occurrence of isotope fractionation and the theory we use to model it. A brief summary of alternative theoretical models to calculate fractionation factors is presented, and the possibility of applying the results to stable isotope thermometry is discussed. We also discuss the problems encountered in performing laboratory experiments to establish an isotope exchange reaction, and the temperature dependency of the fractionation factors with respect to our calculated results.

The theory for isotope exchange reactions was first developed by Urey (1947) and Bigeleisen and Mayer (1947), where they used a statistical mechanics approach to treat a general polyatomic gas. O'Neil (1986) states that this method can be extended to condensed phases if we consider a crystalline structure to be treated as giant molecules consisting of N atoms held together by elastic forces. We have adopted this approach to investigate oxygen isotope exchange reaction between silicates. Consider the following isotope exchange reaction between phases

A and B,

$$aA_1 + bB_2 = aA_2 + bB_1 . \quad (3.7)$$

The subscripts 1 and 2 indicate that the phase contains only the light and the heavy isotopes respectively. The equilibrium constant, K, for this reaction can be written as:

$$K = [Q(A_2)]^a[Q(B_1)]^b/[Q(A_1)]^a[Q(B_2)]^b = (Q_2/Q_1)_A{}^a/(Q_2/Q_1)_B{}^b, \quad (3.8)$$

where Q is the partition function, a statistical mechanics quantity which contains all the energy information of the phase. The fractionation factor, α, is related to K in the following way:

$$\alpha = K^{1/n}, \quad (3.9)$$

where n is the number of atoms exchanged in reaction (3.7). The equilibrium constant can be linked to a common thermodynamic property (such as the Gibbs free energy) by using the following expression:

$$\Delta G = -RT\ln K, \quad (3.10)$$

where ΔG is the change in Gibbs free energy for the exchange, R is the universal gas constant and T is the absolute temperature.

Like all equilibrium constants, K for an isotope exchange reaction is temperature dependant. This is the basis for its use in thermometry. The energy changes in isotopic exchange reactions are of the order of a few joules per mole and thus too small to be measured calorimetrically (Clayton 1981). Direct measurement by exchange reactions is difficult, particularly at low temperatures, because the driving force for the reaction is small. Therefore experiments must frequently be performed at high temperatures and the data obtained must be

extrapolated to lower temperatures. In the range of temperatures of geologic interest, extrapolation laws are not well understood. O'Neil (1986) notes that according to Urey's (1947) theory the sign of the fractionation factor can change ('crossover') with changing temperature and so expressions which describe the temperature dependency of α (like $\ln\alpha = A + B/T$ or $\ln\alpha = A + B/T + C/T^2$, where A, B and C are constants) are only useful for interpolating data, and should not to be used to extrapolate data, as they do not account for any unusual temperature dependencies (crossovers, maxima, minima and points of inflection) of α, and could lead to inferences which may be seriously in error.

Experimentally, there have been many studies of stable isotopes in either synthetically made minerals or natural samples. Thermometry is a necessary tool in geology for determining the temperature of formation of assemblages, establishing the pressure-temperature conditions of metamorphic rocks and estimating temperatures of geothermal reservoirs and of ore deposition. Fractionation in natural samples are usually described by thermometry equations similar to those described above and is related to the per mil concentrations of the O^{18} ($\delta^{18}O$) isotope in the following way;

$$1000\ln\alpha_{X\text{-}Y} = A_{X\text{-}Y}(10^6/T^2) + B_{X\text{-}Y} = \delta_X\text{-}\delta_Y, \qquad (3.11)$$

where the partitioning is between the isotopes O^{16} and O^{18} in substances X and Y. $A_{X\text{-}Y}$ and $B_{X\text{-}Y}$ are constants for the isotope exchange reaction between X and Y, $\alpha_{X\text{-}Y}$ is the fractionation factor for this reaction, δ^X and δ_Y are the per mil concentrations of the O^{18} isotope in X and Y respectively. The validity of expression 3.11 is based upon three assumptions; the exchange reaction must have reached equilibrium, the isotopic compositions were not altered subsequent to the establishment to the equilibrium, and the temperature dependence of the fractionation factors is known from experimental determinations. From our earlier discussions on the temperature dependency of α, we know that equation 3.11 does not allow for any unusual temperature dependencies. Bottinga and Javoy (1973) have extended the work of Bigeleisen and Mayer (1947) to theoretically derive

equation 3.11. They emphasize that the equation is only valid for high temperatures (T > 800K).

Kieffer (1982) has investigated the microscopic origins of isotope partitions, and has devised a model where one can predict thermodynamic properties of minerals such as heat capacities, entropies and Helmholtz free energies from elastic, structural and spectroscopic data. In order to carry out a Kieffer model calculation, however, one has to assume or construct the form of the density of states function. The calculated isotope equilibria presented by Kieffer (1982) are, however, in good agreement with experimental values. More recently, Schütze's (1980) increment method has been applied to oxygen isotope fractionation for mineral-water systems by Richter and Hoernes (1988). Two empirically derived factors are used in order to simplify the method. The first factor is used to multiply the O^{18} increments of the weakly bonded cations and the second factor is the value of $1000\ln\alpha_{water}$ which is a mean value based on experimental data taken from a whole variety of sources. The results are presented in the form of calibration curves ie. $1000\ln\alpha_{mineral\text{-}water} = A + B \times 10^3/T + C \times 10^6/T^2$, where the coefficients A, B and C are calculated for each mineral-water system. Smyth (1989) has also computed the electrostatic binding energies at various sites in mineral structures from accurately measured crystallographic data. He has found that the differences in the potentials for various sites between different structures is strongly correlated with observed oxygen isotope fractionation between minerals, and future work may predict fractionation factors from electrostatic site potentials of anion sites.

In our study, we used PARAPOCS to calculate the free energy of isotopically distinct silicates as a function of temperature. Thus, for a pair of minerals, by calculating the free energy of the four species in the exchange reaction 3.7, we can calculate the overall change in free energy for the reaction and hence α by using 3.10 and 3.9. As stated earlier, quartz has not been included in this part of the study because simulations at temperatures above 600K would approach a displacive phase transition and this is not accommodated by the model used in PARAPOCS. The predicted temperature dependency of α for each mineral-mineral

system is displayed in Figure 3.4. Not only is the correct 'sense' of each reaction predicted (for example, O^{16} prefers albite rather than diopside and not vice versa) but the fractionation factors also tend to 1.0 with increasing temperature, which we would expect from equation 3.10. It should be noted that from our calculations the diopside-pyrope and diopside-forsterite systems show a crossover of the fractionation factor. This behaviour is as yet not understood. Kieffer (1982) suggests that crossovers would be unlikely in sets of minerals with comparable compositions (such as anhydrous silicates) because of the regularity in behaviour of vibrational modes with degree of polymerization of the Si-O bonds and the monotonic dependence of the partition function on this behaviour. Such behaviour has not yet been observed for mineral-mineral systems either from natural data or from laboratory data but has been clearly seen in mineral-fluid and melt-fluid experiments (see for example, O'Neil and Taylor 1967, and Matsuhisa el al. 1979). Clearly, this type of behaviour is as yet unresolved and a matter of considerable debate.

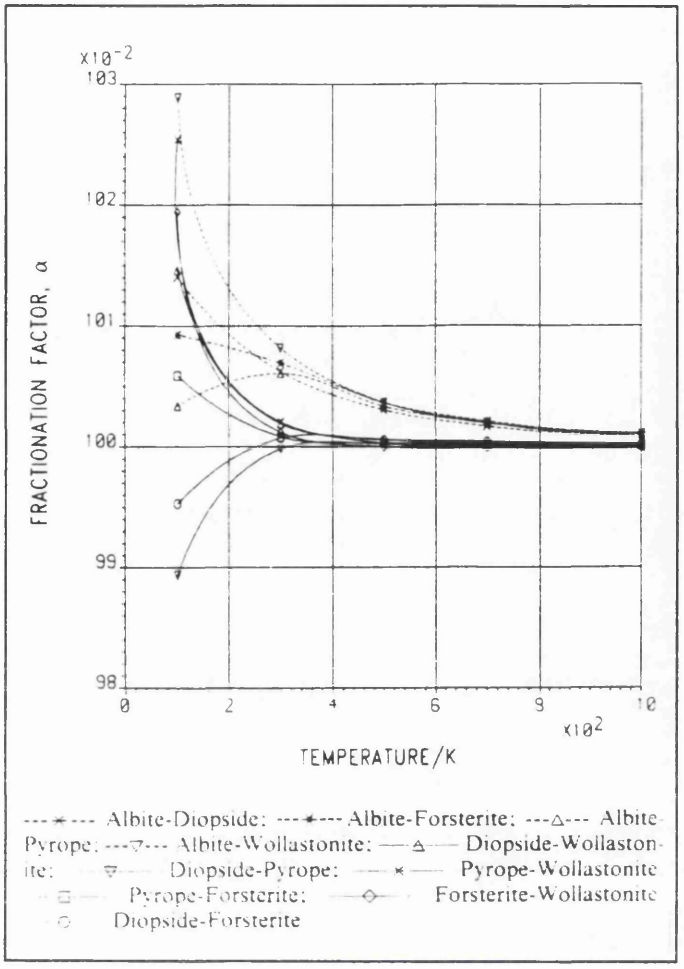

Figure 3.4 The temperature dependency of the fractionation factor

We have compared our calculated fractionation factors to experimental values, where they exist, and are shown in Table 3.12. The observed values which do not have uncertainty limits are for exchange reactions between generic members. Clearly, agreement is rather poor and the best values are for the diopside-pyrope system where the calculated values are underestimated by 30%. From these results, it is not clear where the source of divergency arises. Hence, we have studied the isotope effects for each individual silicate by calculating the reduced partition function ratio, f, as a function of temperature, T, from the following expression:

$$\ln f = (-(F^*-F)/kT) + (3r/2 \times \ln(m/m^*)), \qquad (3.12)$$

where m and m^* are the masses of the exchanging isotopes, F is the Helmholtz free energy, r is the number of atoms of the element undergoing exchange and k is Boltzmann's constant. Note that our simulations are at zero pressure and so the Gibbs and Helmholtz free energies are equal. In Table 3.13 we have compared our calculated values of $1/r1000\ln f$ from 300 to 1000K with Kieffer's (1982). Forsterite gives the best agreement where the percentage difference from Kieffer's (1982) values varies from less than 0.1% at 300K to a maximum of 5.6% at 500K. Diopside and pyrope have comparable differences ranging from a minimum 1.2% (diopside at 1000K) to 12.8% (diopside at 700K). Albite gives the worst agreement where the average percentage difference is 13%. These differences in agreement correlates very well with the performance of the potential models in predicting the structure and thermodynamics of each mineral. If we refer back to the structure data in Tables 3.3 and 3.4 and also the thermodynamic data in Table 3.7 we see that forsterite gives the best agreement in cell parameters, volume, heat capacity and entropy and albite has the poorest simulated structure. This implies that the prediction of isotope effects are critically dependant on the accuracy of the simulated structures, lattice dynamics and thermodynamics. Hence, the slightest inaccuracy in the potential parameters will lead to poor values for isotope effects. This is confirmed if we look at the component energies which add to give the Gibbs free energy potential, G:

Table 3.12 Predicted and observed fractionation factors

	T/·C	α_{pre}	α_{obs}
Albite-Diopside	600	1.00100	1.00313 +/- 0.00140
	700	1.00090	1.00287 +/- 0.00115
Albite-Pyrope (Plagioclase-Garnet)	500	1.00163	1.00320
	600	1.00129	1.00251
	700	1.00109	1.00202
Albite-Forsterite	600	1.00141	1.00405 +/- 0.00141
	700	1.00118	1.00379 +/- 0.00116
Albite-Wollastonite	600	1.00140	1.00301 +/- 0.00140
	700	1.00120	1.00276 +/- 0.00115
Diopside-Pyrope (Pyroxene-Garnet)	500	1.00025	1.00035
	600	1.00021	1.00028
	700	1.00018	1.00022
Diopside-Forsterite	600	1.00032	1.00223 +/- 0.00142
	700	1.00027	1.00199 +/- 0.00117
Diopside-Wollastonite	600	1.00020	1.00143 +/- 0.00131
	700	1.00015	1.00118 +/- 0.00106

Note: References: Chiba et al. (1989); Matthews et al. (1983); Bottinga and Javoy (1975)

Table 3.13 Reduced partition function ratios of the silicates studied

Mineral	T/K	1/r1000ln*f*	
		Calculated	Kieffer (1982)
Albite	300	88.5	98.8
	500	36.1	40.0
	700	19.1	23.2
	1000	9.3	10.8
Diopside	300	81.5	85.6
	500	32.2	34.8
	700	17.1	19.6
	1000	8.5	8.4
Forsterite	300	80.7	80.0
	500	31.6	31.6
	700	16.6	17.6
	1000	8.2	8.0
Pyrope	300	81.1	85.6
	500	32.3	33.6
	700	16.9	18.8
	100	8.3	8.0
Wollastonite	300	80.4	
	500	31.2	
	700	16.3	
	1000	8.2	

$$G = E - TS + PV, \quad (3.13)$$

where E is the total energy of the crystal, T is the absolute temperature, S is the entropy, P is the pressure and V is the volume. In our calculations P = 0.001kbars and so there is very little contribution from the pressure-volume term. (Incidentally, the isotope exchange experiments were performed between 1 and 24kbars pressure (see for example, Chiba et al. 1989), however, pressure effects are assumed to be negligible, and this has been shown experimentally by Clayton et al. (1975). Therefore, comparison of observed data with the results from our calculations is valid). Hence the precision of G is dependant on the accuracy of both E and S which, as explained earlier, are both calculated from the potentials. The study of such subtle effects (energies of a few joules per mole) reveals the limitation of our methodology and potential models.

3.5 Summary

We have reported free energy minimisation studies for a wide variety of silicate minerals where the calculations were based on a lattice dynamics model to the quasi-harmonic level of approximation. Overall, we can conclude that the model works very well, although the calculated fractionation factors are not yet sufficiently accurate to be practically useful. The predicted structure and bulk thermodynamics of the silicates however are excellent and this clearly shows, along with other applications of the model (see, for example, Jackson and Catlow 1988, and Winkler et al. 1990), that the type of model potentials used in this chapter are genuinely transferable, and can be applied to a wide variety of structural topologies (ortho-, chain-, layer- and framework-silicates). We suggest that the thermodynamic properties predicted from our fundamental, microscopic, atomistic models can now be considered as reliable as the predictions made by other bulk, phenomenological or empirical approaches. However, refinements of the potential parameters are necessary if we are to predict accurately the structures and thermodynamic properties (to within 0.1% of observed values) that appear to be required if our

approach is to be extended to the quantitative study of isotope effects, and rigorous testing of the temperature and pressure dependency of the fractionation factor.

We have seen in section 3.4 how important the anharmonic effects are at high temperatures and how our model, which is based on the quasi-harmonic approximation, only accounts for extrinsic anharmonicity. In the next chapter a detailed investigation of the intrinsic anharmonicity is given and quantitative estimates of these effects on geophysically important properties are also presented. It has also been shown that the nature of the interatomic potentials used also limit the reliability of our results, so in Chapter Five we outline a strategy whereby quantum mechanics can be used to study the nature of the electronic environment in the crystal structure.

CHAPTER FOUR

ANHARMONICITY AND THE BREAKDOWN OF THE QUASI-HARMONIC APPROXIMATION

4.0 Introduction

In this chapter we investigate the limit of the quasi-harmonic approximation (QHA) in the LDS model by simulating periclase (MgO) and $MgSiO_3$ perovskite from low to high temperatures and pressures. It is generally accepted that $MgSiO_3$ perovskite is the most abundant mineral in the Earth (about 40% of the total composition, and 80% of the lower mantle) and so a reliable theoretical approach to simulating its structure and physical properties is of great value. It is hoped that this work will pinpoint the future requirements for accurate modelling of the structure and thermodynamics so that the results obtained can be used to pinpoint the important geophysical parameters such as the thermal expansion coefficient, the melting temperature and the clarification of the phase diagram for the $MgSiO_3$ - $FeSiO_3$ system (see Figure 1.9). Work has already been carried out in this direction (see Matsui and Price 1992) where the polymorphs of $MgSiO_3$ have been studied using the MDS technique. Also related to these phase diagrams is MgO in the form of magnesiowüstite. Therefore, reliable simulations of periclase will provide an important preliminary step for future calculations of the magnesiowüstite system and further fine tuning of the predicted phase diagrams. The transport properties of minerals is another application of our simulation approach and so the determination of the limitations of this methodology will be useful for investigating the dynamic phenomena of electrical and thermal conductivity, diffusion and rheology of the mantle (see for example, Wall and Price 1989). We adopt the MDS technique to model the intrinsic anharmonic component which is not included in the LDS approach (see sections 2.2.2 and 2.3.1). By comparing the results obtained

from the two procedures it should be straightforward to ascertain the temperature and pressure conditions at which the QHA breaks down and therefore see what implications this has for modelling the various geological environments (i.e. upper and lower mantle).

In the next section we briefly review some of the recent research that has been carried out in the geosciences community on anharmonicity and this is followed by a discussion of the conditions and parameters input into the MDS and LDS codes in order to perform successful simulations of MgO and $MgSiO_3$. Following this, a detailed discussion of our results is given and we investigate the effects of anharmonicity on geologically important parameters such as molar volume, thermal expansion coefficient, isothermal bulk modulus and the average Grüneisen parameter. We conclude this discussion by estimating the percentage corrections one would have to allow for to the above properties, at a variety of temperatures and pressures, if the LDS model was used. Finally, a summary of the chapter is given.

4.1 Review of recent literature on anharmonicity

We have already mentioned in Chapter Two the hypothesis proposed by Hardy (1980) which states that the intrinsic anharmonicity of a crystal will reduce as the applied hydrostatic pressure is increased. This can be understood by the following qualitative reasoning. As the external pressure is applied and the temperature is kept fixed, the cell volume reduces, i.e. the average interatomic separation becomes smaller, and the atoms or ions feel a stronger repulsive force from the forcing together of the electron clouds which is forbidden by the Pauli exclusion principle. Therefore, the ions would not only find less space in which to move but also feel a stronger force keeping them to their equilibrium positions. Hence, at high pressures there would be small displacements about the equilibrium positions even at large temperatures, thus following the symmetric or harmonic part of the potential energy curve.

In Chapter Three we saw how the QHA overestimates the phonon pressure at high temperatures and this understanding has been brought about by the work of Boyer (1981). He has used Gordon-Kim (1972) type pair potentials in quasi-harmonic equation-of-state calculations for alkali halides and the relevant results are shown in Figure 4.1 where isothermal curves of vibrational pressure for sodium fluoride are plotted along with the static pressure contour. We see that an instability arises in the QHA at high temperatures (T=1200 for NaF) and this would have the consequence of predicting imaginary frequencies for the modes of vibration (see equation 2.38) in the LDS model. We will be referring to this point many times in our discussions as it pinpoints the precise limitations of the QHA. Boyer and Hardy (1981) have extended the work to investigate the structural phase transition in $RbCaF_3$ which led to the study of the analogue perovskite structure $CsCaF_3$ (see Boyer 1984).

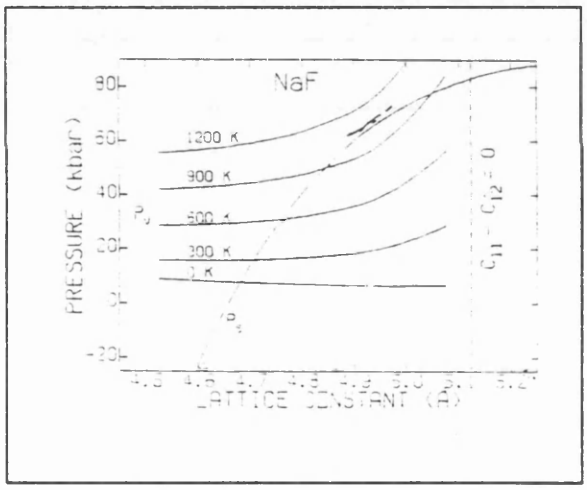

Figure 4.1 Plot of static pressure and vibrational pressure (for selected temperatures) as a function of lattice constant. The arrows on the abscissa indicate measured volumes of the solid at 0 K and T_m, and of the liquid at T_m. (After, Boyer 1981)

Gillet and his co-workers have produced some excellent experimental work on high temperature and high pressure Raman spectroscopic studies on the olivine structures (see for example, Gillet et al. 1989 and 1991; Reynard et al. 1992). They have demonstrated that it is possible to calculate intrinsic anharmonic parameters from the change in mode frequency with temperature or pressure. Their current experimental arrangement has constrained them to looking either at temperature or pressure dependency however they are currently working on the simultaneous variation of both parameters.

O. L. Anderson has been keenly interested in the effects of anharmonicity on geological materials for many years (see for example, O. L. Anderson et al. 1990; O. L. Anderson and Suzuki 1983). The work consists of investigating the high temperature effects on the Hildebrand equation-of-state for simple solids like LiF, NaCl and MgO. He has also compared the effects on the average Grüneisen parameter, thermal pressure and heat capacity at constant volume and for the minerals forsterite, fayalite and periclase. The results illustrated that the effects are not necessarily consistent in each case and that opposite trends can be observed. Finally, there has been the development of what is now called the Anderson-Grüneisen parameter which is constant over any temperature range within the assumptions of its derivation. Experimental data for the garnets, forsterite, MgO and iron have confirmed this and so have theoretical calculations (see Reynard and Price 1990). We will also calculate this parameter for our case studies to see if we arrive at the same conclusion.

The next section gives the essential parameters input into the LDS and MDS models for energy simulations of the chosen test minerals.

4.2 Input for the simulation models

In this study we have simulated the physical properties of MgO (periclase) and $MgSiO_3$ perovskite in order to investigate the effects of anharmonicity. To

show that our methodology is independent of the potential model we have used a fully ionic (FI) and partial ionic (PI) charge models for MgO. We will denote each of these as MgO.FI and MgO.PI respectively. The potential parameters are listed in Table 4.1. Note that we are using a rigid-ion model, i.e. we assume that the charge distribution of an ion is not significantly disturbed when brought into the proximity of other ions. Hence, only two-body interactions are considered and the total expression for the potential energy is given by equation 2.6. The potential parameters employed have given successful and accurate simulations previously (see, Lewis and Catlow 1985; Matsui 1988 and 1989), therefore, we have not compared our predicted results with observed data as we feel that this prerequisite has already been established. In Figures 4.2a, b and c the experimental high pressure and temperature data is presented for MgO and $MgSiO_3$. In Figures 4.2a and b the observed values are compared with the MDS calculations performed by Matsui (1989) for MgO using the same partial-ionic potentials as listed in Table 4.1. Figure 4.2c shows, not only the experimental data for the P-V-T relations of perovskite (Mao et al. 1991), but also their calculated equations of state. For comparison with the calculated $MgSiO_3$ data see the Appendix where the values for volume and enthalpy are presented in tabulated format.

We set the lattice parameter for MgO (FI and PI) in the LDS model to 4.23Å (L_1) and, subsequently, the short-range potential cut-off to $2.61L_1$. The maximum magnitude of the phonon wavevector equals L_1 and a ten special-point set of Chadi and Cohen (1973) was employed to sample the Brillouin zone. Similarly, for $MgSiO_3$ the lattice parameter, L_2 = 4.78Å and the short-range potential cut-off = $2.5L_2$. The maximum magnitude of the phonon wavevector was also L_2 but the reciprocal space sampling equation 3.1 (27 points) was used in this case.

Table 4.1 Potential parameters used for MgO and $MgSiO_3$

Interaction	Potential Parameters			Ref.
	A/eV	ρ/Å	C/eVÅ^{-6}	
MgO Full Ionic Charge Model				
O^{2-} - O^{2-}	22764.0	0.1490	27.8800	1
Mg^{2+} - O^{2-}	812.07	0.3242	0.0	2
MgO Partial Ionic Charge Model q/l el: Mg = +1.4; O = -1.4				
O - O	2145.69	0.3000	30.2220	3
Mg - O	9892.16	0.2020	0.0	3
Mg - Mg	1309336.7	0.1040	0.0	3
$MgSiO_3$ Partial Ionic Charge Model (MAMOK) q/l el: Mg = +1.565; Si = +2.339; O = -1.298				
O - O	1621.68	0.3000	30.2220	4
Mg - O	8035.12	0.2020	0.0	4
Si - O	7363.45	0.1900	0.0	4
Mg - Mg	1309336.7	0.1040	0.0	4
Mg - Si	2325826.6	0.0920	0.0	4
Si - Si	5005903.5	0.0800	0.0	4

Note: 1 Sanders et al. 1984; 2 Lewis and Catlow 1985; 3 Matsui 1989; 4 Matsui 1988

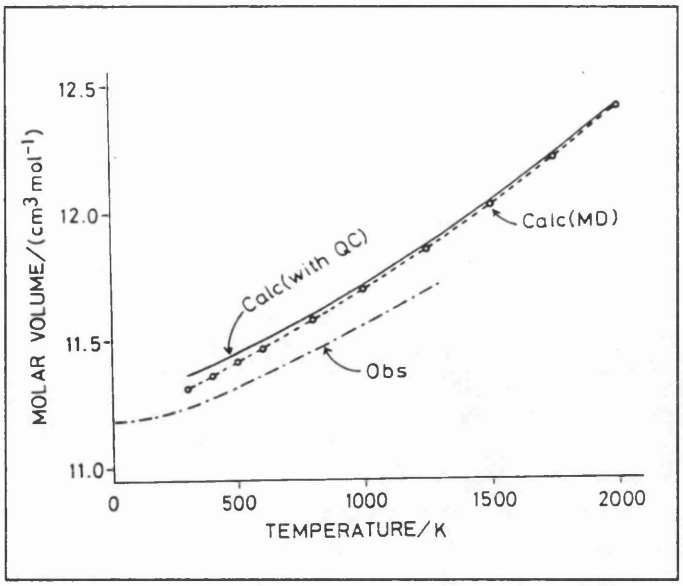

Figure 4.2a Temperature dependence of the molar volume of MgO at zero pressure. Solid line is the calculation including the quantum corrections. Observed data from Anderson and Suzuki (1983). (After, Matsui 1989)

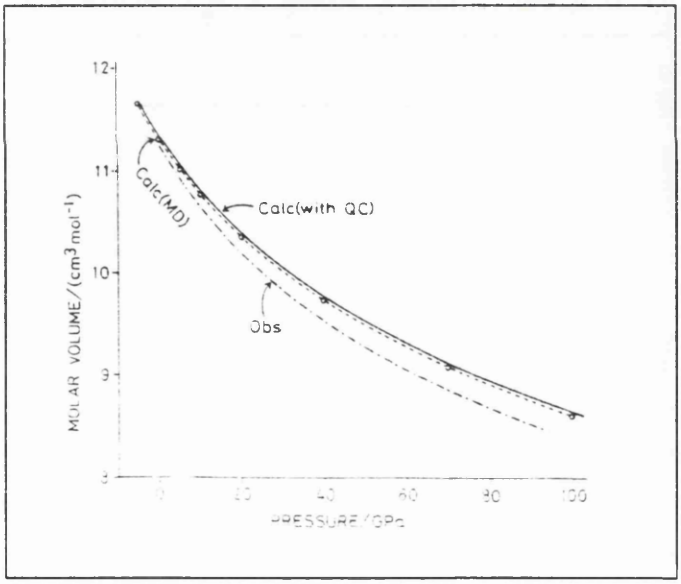

Figure 4.2b Pressure dependence of the molar volume of MgO at 300K. Same notation as in above figure. The experimental data is from Mao and Bell (1979). (After, Matsui 1989)

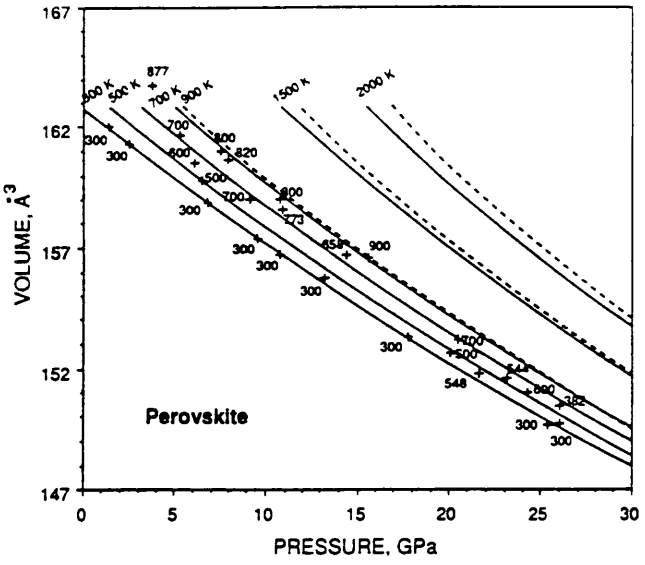

Figure 4.2c The P-V-T relations of perovskite. Crosses represent the experimental data and the lines are the calculated EOS. The numbers indicate the temperatures in Kelvin. (After, Mao et al. 1991)

Obviously, the MDS input takes a slightly different format as we are dealing with a different physical model. For MgO, the size of the MDS cell was 4 x 4 x 4 (i.e. 64) unit cells but for $MgSiO_3$ an MDS cell of 3 x 3 x 3 , 27 unit cells was chosen due to computational constraints. The same timestep of 1.0fs was used for both minerals and sufficient timesteps (around 4000 to 6000) were performed in each simulation for "aging" purposes allowing sufficient time for equilibration. A further 5000 timesteps are the carried out for the averaging of the physical properties. There are two adjustable parameters, Q and W (see equation 2.9) which emerge from the constant temperature (Nosé 1984) and constant pressure (Parrinello and Rahman 1981) routines and these have been set as following; Q = 10.0kJmol^{-1}ps^2 for MgO and $MgSiO_3$, W = 40.0gmol^{-1} for MgO and, finally, W = 100.0gmol^{-1} for $MgSiO_3$. These two parameters determine the timescale of the temperature and volume fluctuations, respectively, but they have no effect on the trajectory averages calculated from a simulation (Haile and Graben 1980; Nosé 1984). Having fixed the main input parameters the code initiates the usual periodic boundary condition. It is important to note that no symmetry constraints are imposed as the success of a simulation is determined by the prediction of the

correct crystal structure. Recent developments applied to the MDS code (see Parker and Watson 1992) have eliminated the problem of having to set energy convergent values for two parameters used in the Ewald summation for the potential energy (see sections 2.1). It has been shown (Parker and Watson 1992) that the new procedure (which can be initiated by a default value) is in accordance with the Ewald methods of THBREL and PARAPOCS and affects the cell volume by approximately 1 per cent. We have not recalculated our MDS enthalpies and volumes because we feel that such small changes to the absolute values will not affect the calculated trends significantly. We now discuss the results of our simulations.

4.3 The effects of intrinsic anharmonicity on key geophysical properties

From the simulated volume and enthalpy at various temperatures and pressures it is possible to calculate the thermal expansion coefficient, isothermal bulk modulus and heat capacity at constant pressure from their temperature and pressure derivatives. Hence, it is then possible to predict other thermodynamic properties such as the average Grüneisen parameter and heat capacity at constant volume. We have performed simulations to high temperatures (~3000 to 4000K) and high pressures (either to 500 or 1000kbars). The temperature and pressure derivatives were obtained from regression fits of the enthalpy and volume data. The limitations of this approach will we discussed as we progress through this section.

We start by investigating the effects of intrinsic anharmonicity on the molar volume. We see from Figures 4.3a, b and c that the calculated volume rises with temperature and decreases with pressure as expected. For all cases (i.e. MgO.FI, MgO.PI and $MgSiO_3$) at the higher temperatures V(LDS) is larger then V(MDS) except at high pressures where they converge. From our earlier discussions on Boyer's (1981) work we see that these results are entirely as we would expect. The QHA overestimates the vibrational pressure at high temperatures, thus giving a higher than normal value for the cell volume. However, if we increase the external

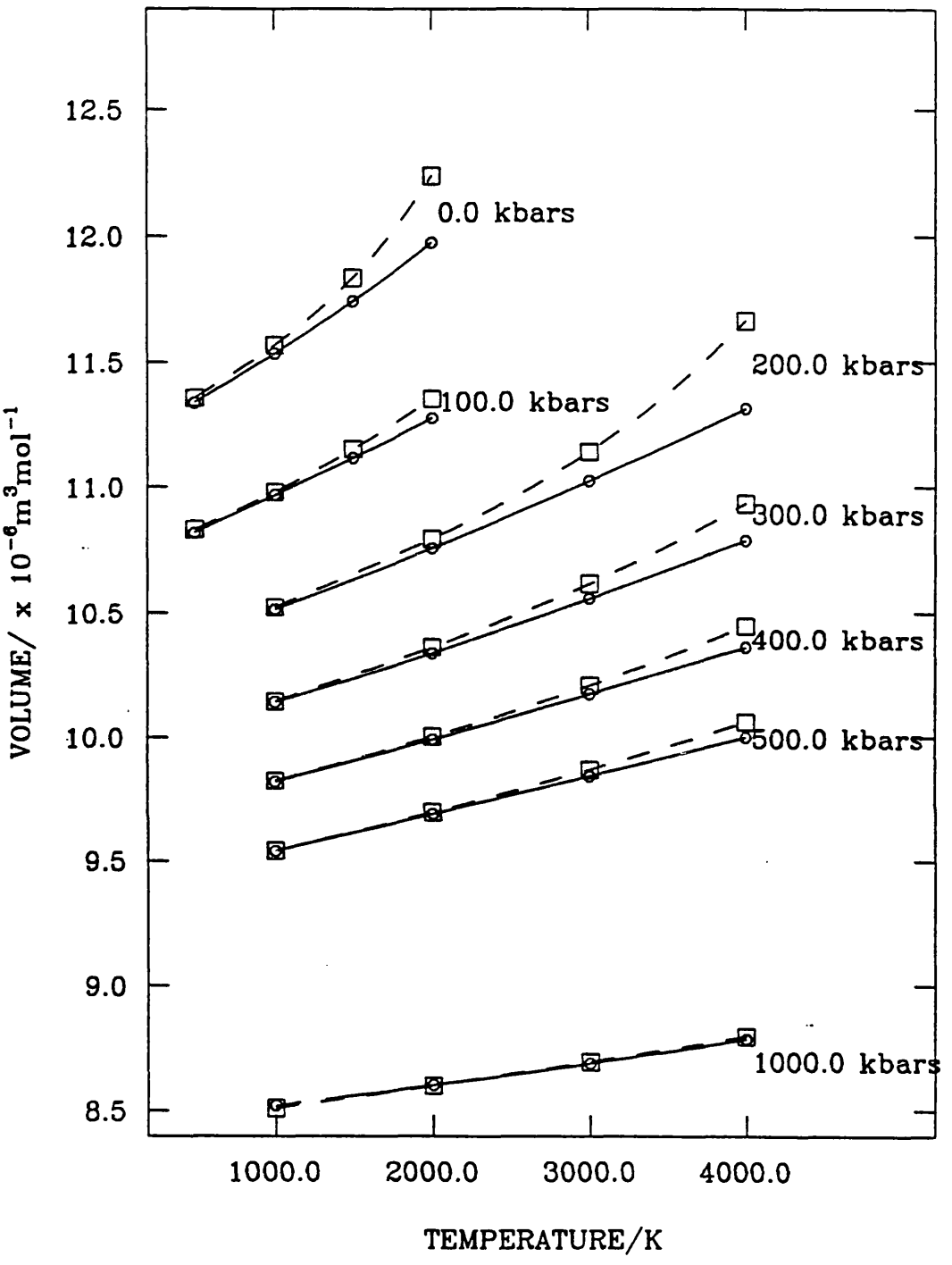

Figure 4.3a Calculated molar volumes for MgO.FI (LDS = ------)

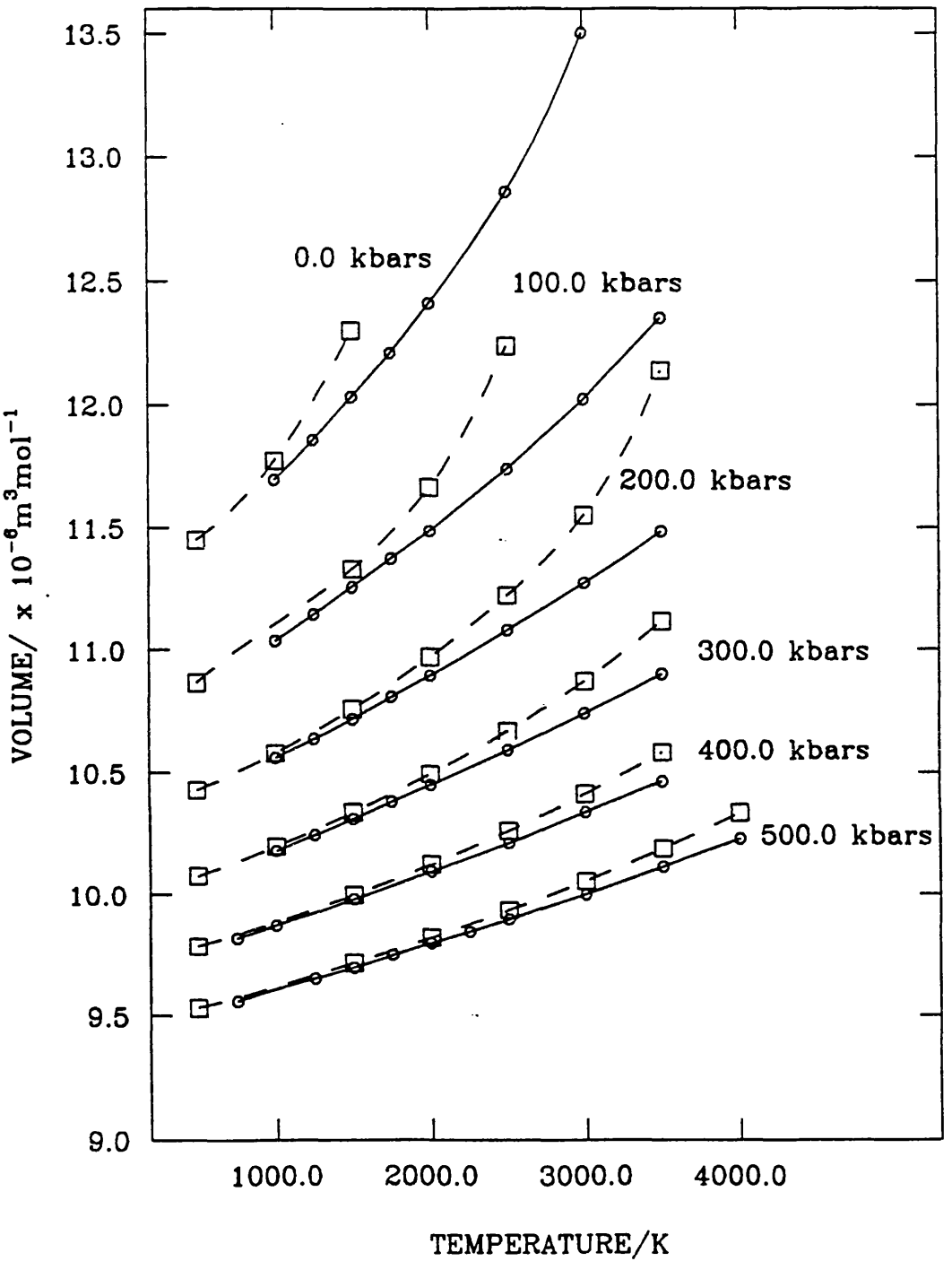

Figure 4.3b Calculated molar volumes for MgO.PI (LDS = ------)

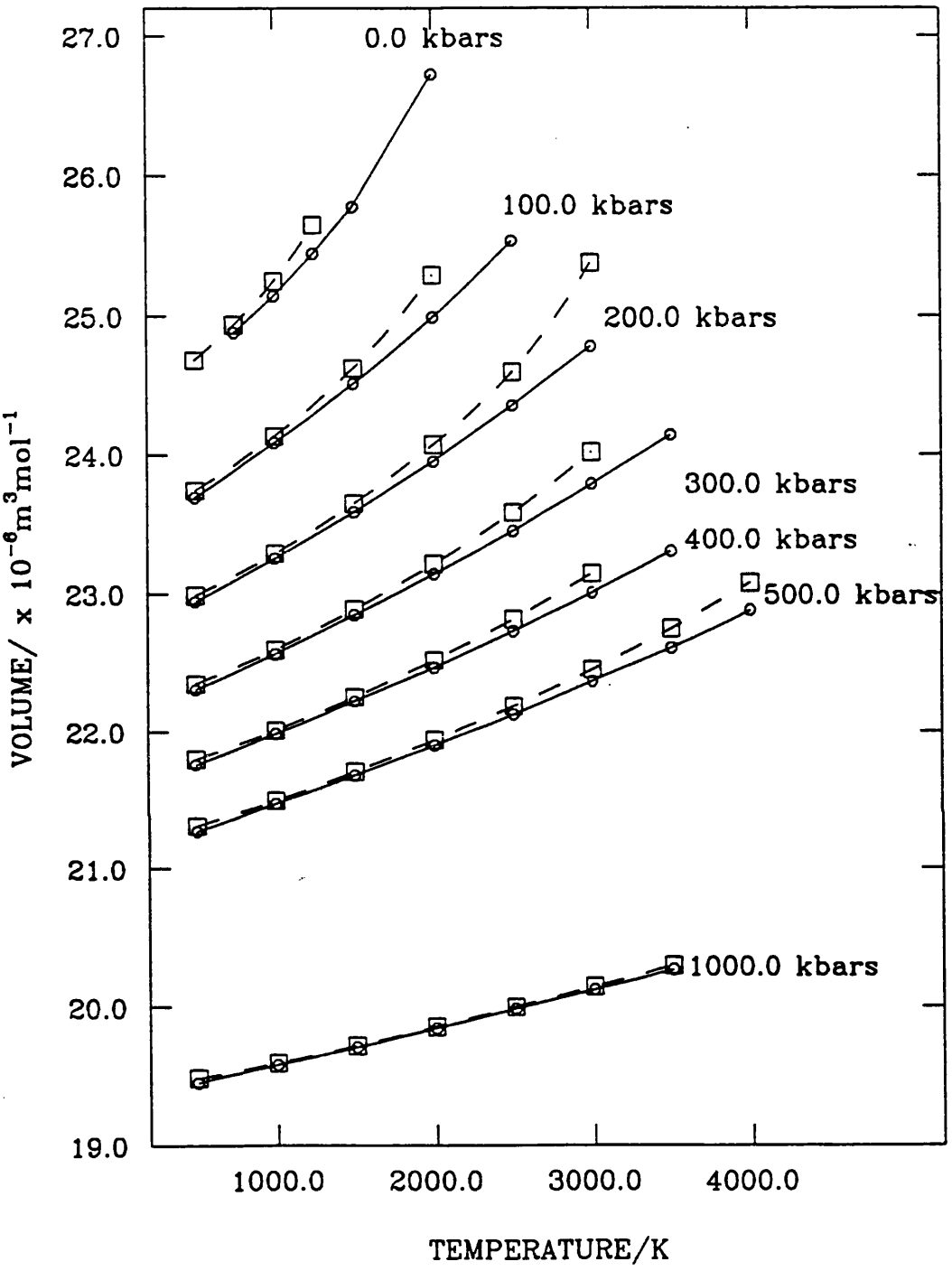

Figure 4.3c Calculated molar volumes for $MgSiO_3$ (LDS = ------)

pressure the QHA has a greater field of stability (see Figure 4.1) and subsequently does not break down. In other words, the intrinsic anharmonic effects become less with increasing pressure and the MDS results tend to the values obtained by the QHA.

The enthalpy, H, is a measure of the internal energy of a crystal plus a pressure-volume term. From inspection of Figures 4.4a, b and c we see that the trends are identical to the volume curves except that the relative differences are smaller. Once again H(LDS) is greater (i.e. less negative) than H(MDS) at high temperatures because the vibrational energy component of the internal energy is overestimated by the QHA as is the volume. Both of these facets give an additional positive contribution to the overall enthalpy. The enthalpies from the two modelling approaches converge at high pressures which, yet again, supports Hardy's (1980) hypothesis.

Figures 4.5a, b and c show the calculated thermal expansion coefficients, β, for the above stated temperature and pressure ranges. The values generally increase with temperature and the reasons for this were presented previously in section 3.4. However, there are some fluctuations from this trend at 200kbars for MgO.FI and $MgSiO_3$, and at the low pressures for MgO.PI. Although there are curvatures in the theoretical thermal expansion coefficient vs. temperature curve, we feel that this is what we are not seeing here. We can clearly see from the raw data of enthalpy and volume (presented in Appendix A) that for each pressure we have carried out calculations at only a few temperature points due to the restrictions in computational resources. Therefore, the polynomial fits to each dataset gives the general trend required but may not be of the closeness that is necessary when investigating the variations of differentials. Hence, the curvatures in Figures 4.4a, b and c are probably due to errors incurred from imprecise fitting. We would expect β to decrease with pressure because the slopes of the volume-temperature curves (Figures 4.2a, b and c) become less inclined with increasing pressure. It is easy to deduce that at a given temperature β(LDS) is greater than β(MDS) as the LDS volume-temperature slopes are steeper for each pressure except at the high

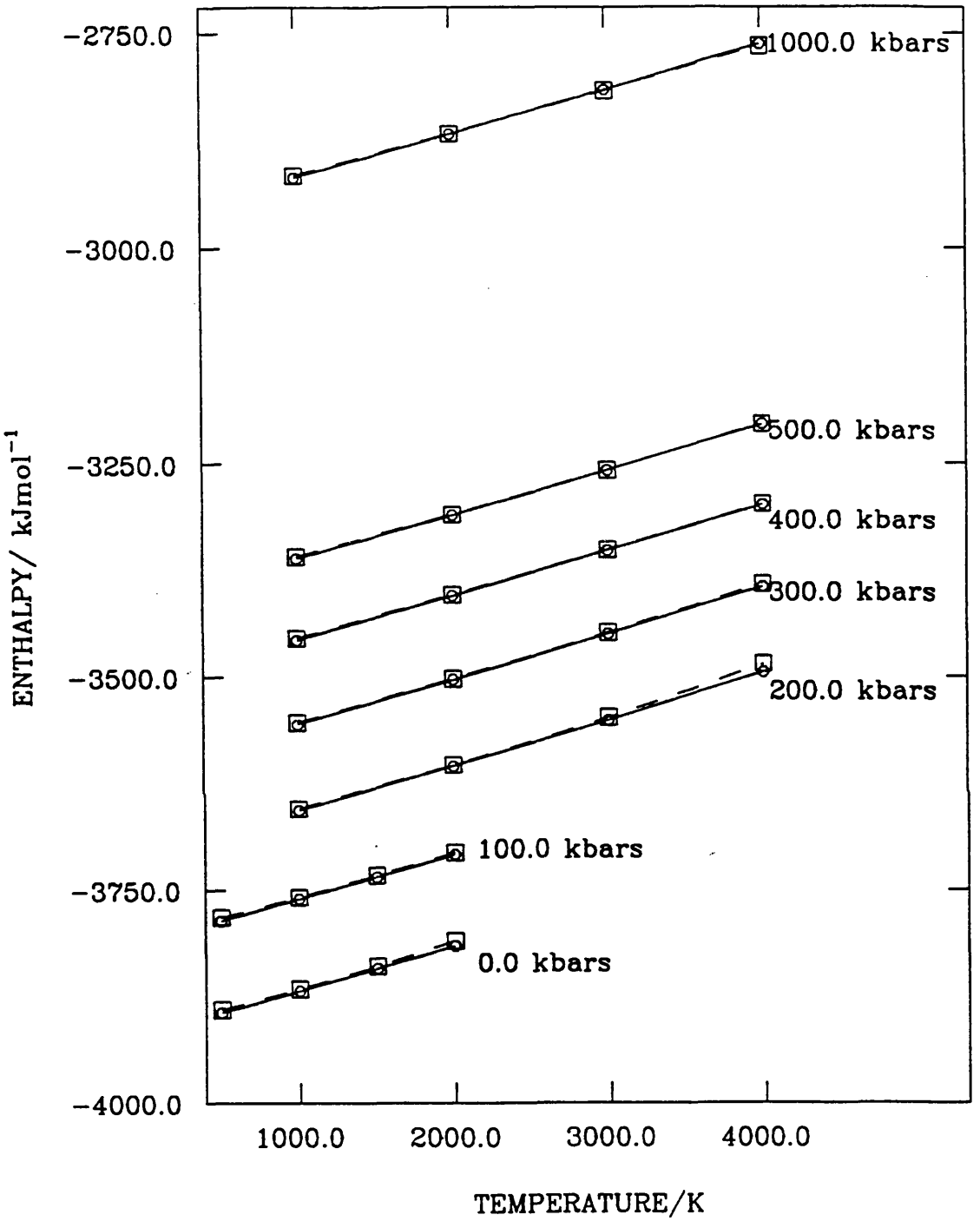

Figure 4.4a Calculated enthalpies for MgO.FI (LDS = ------)

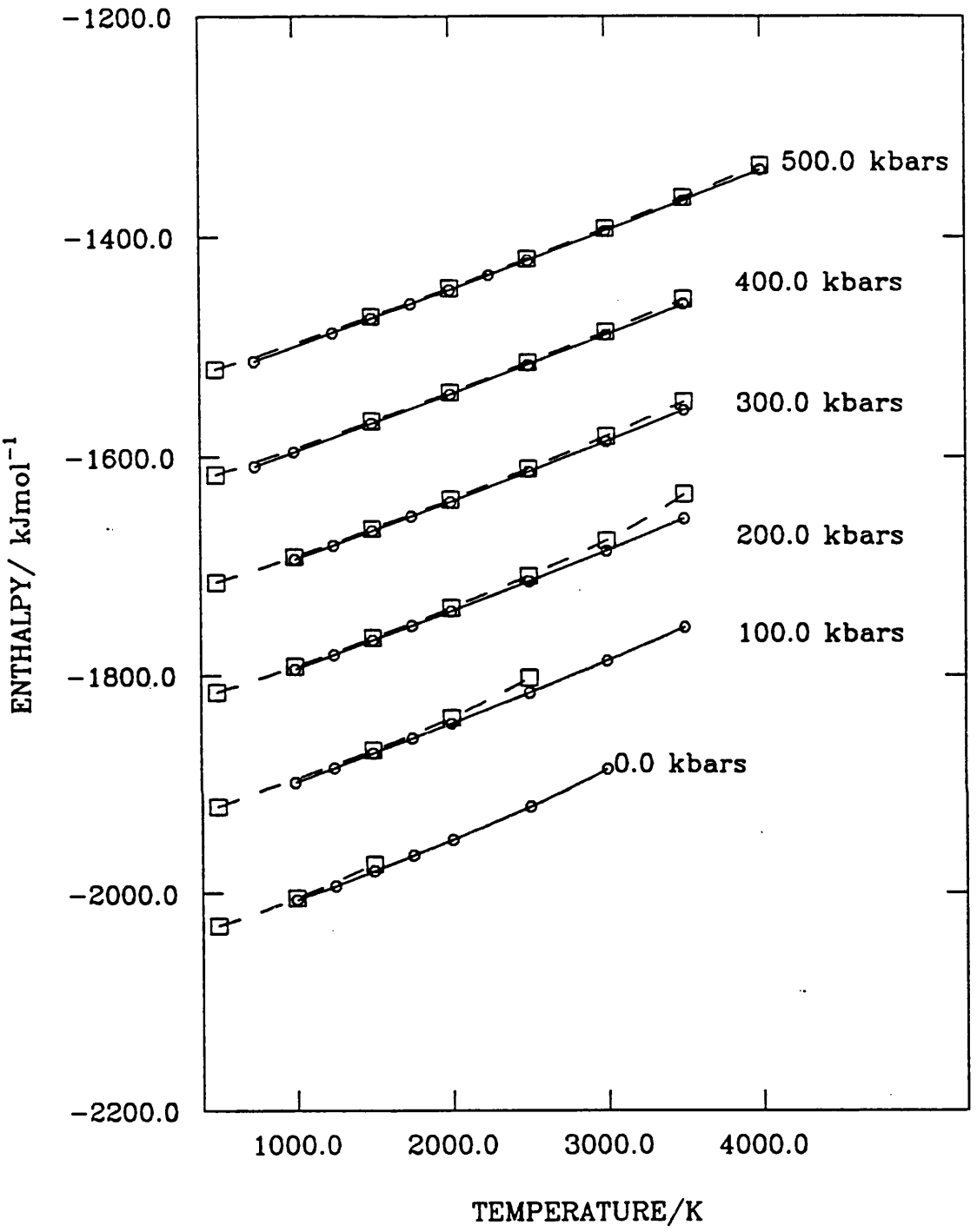

Figure 4.4b Calculated enthalpies for MgO.PI (LDS = ------)

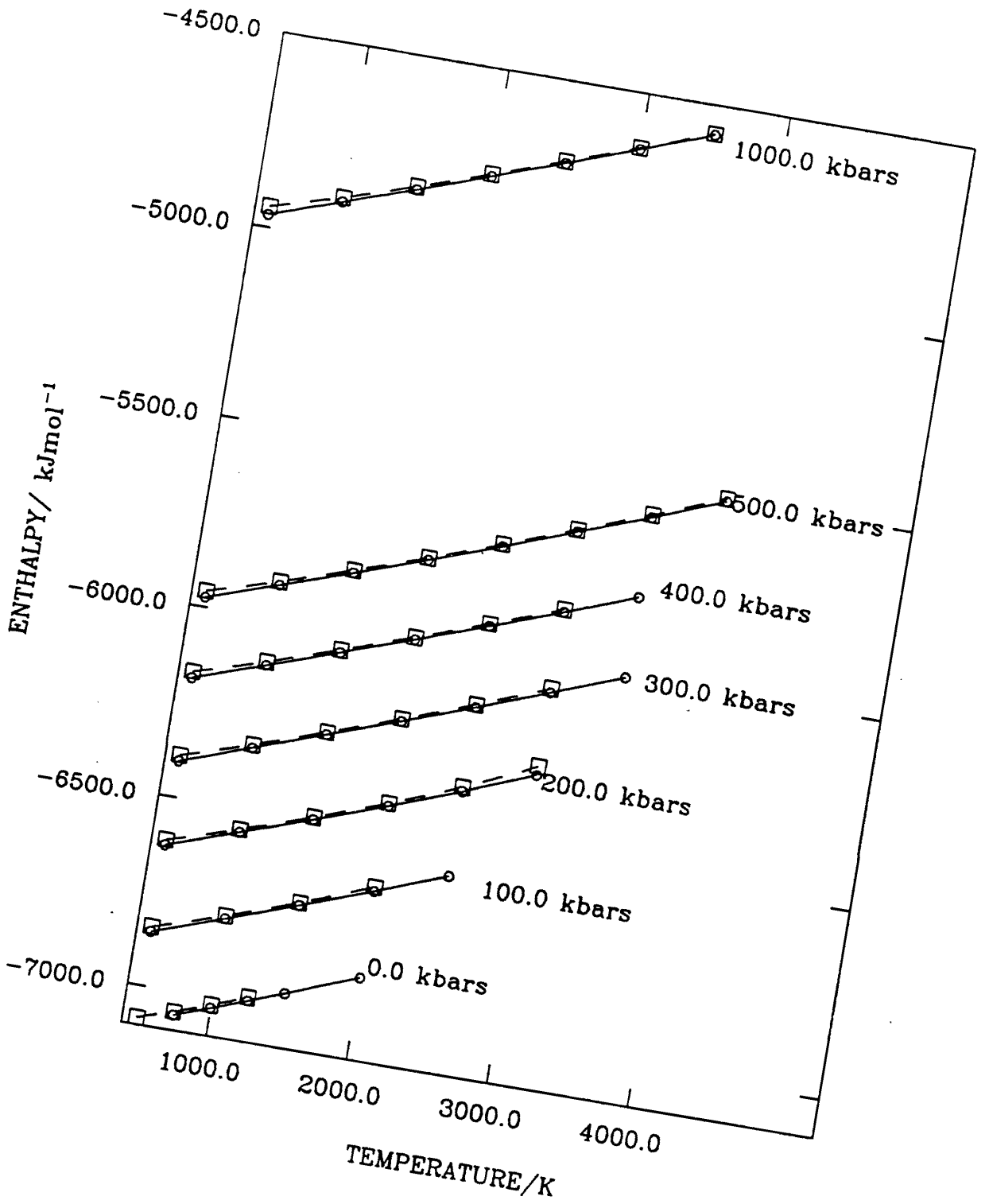

Figure 4.4c Calculated enthalpies for $MgSiO_3$ (LDS = ------)

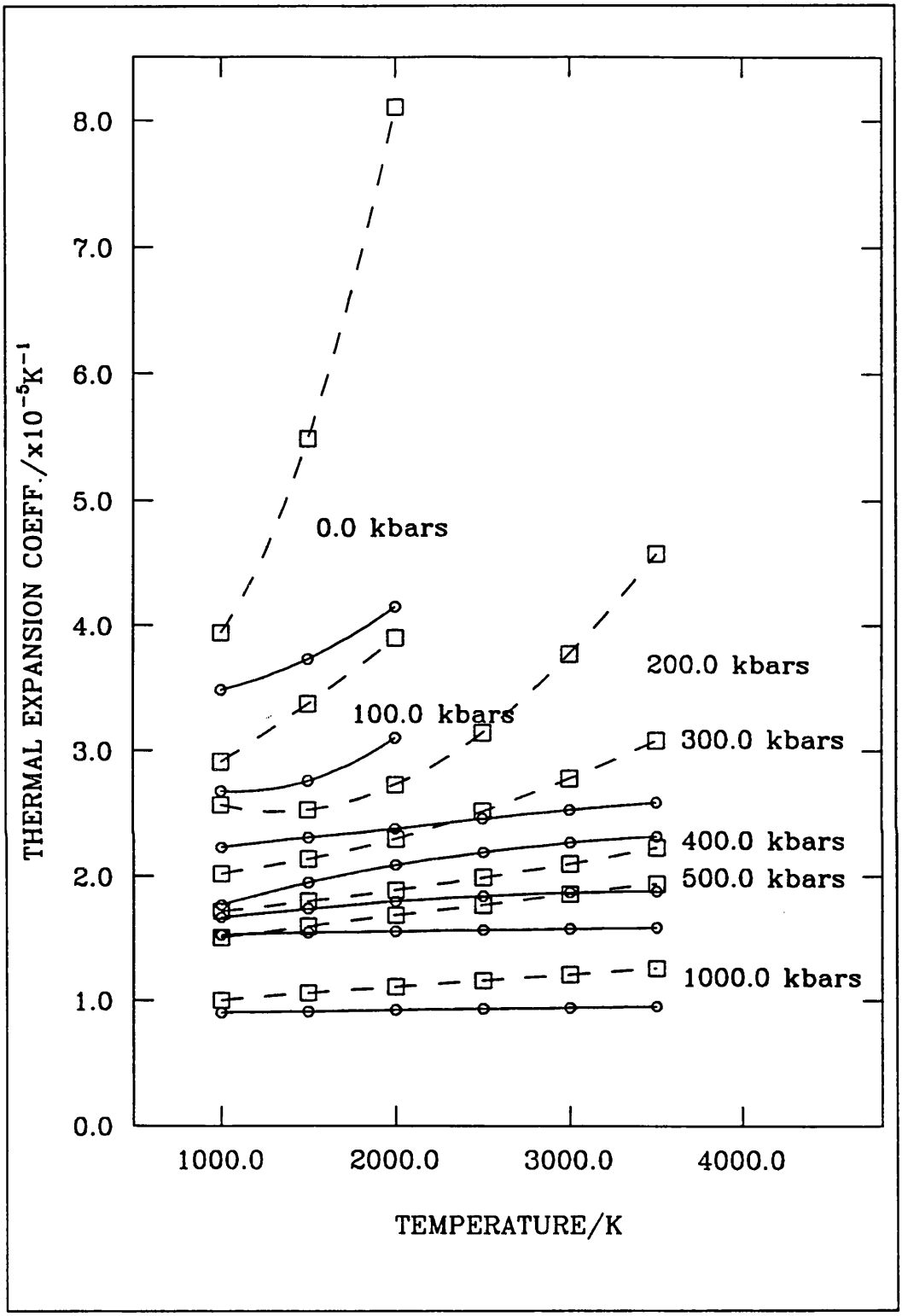

Figure 4.5a Calculated thermal expansion coefficients for MgO.FI (LDS = ------)

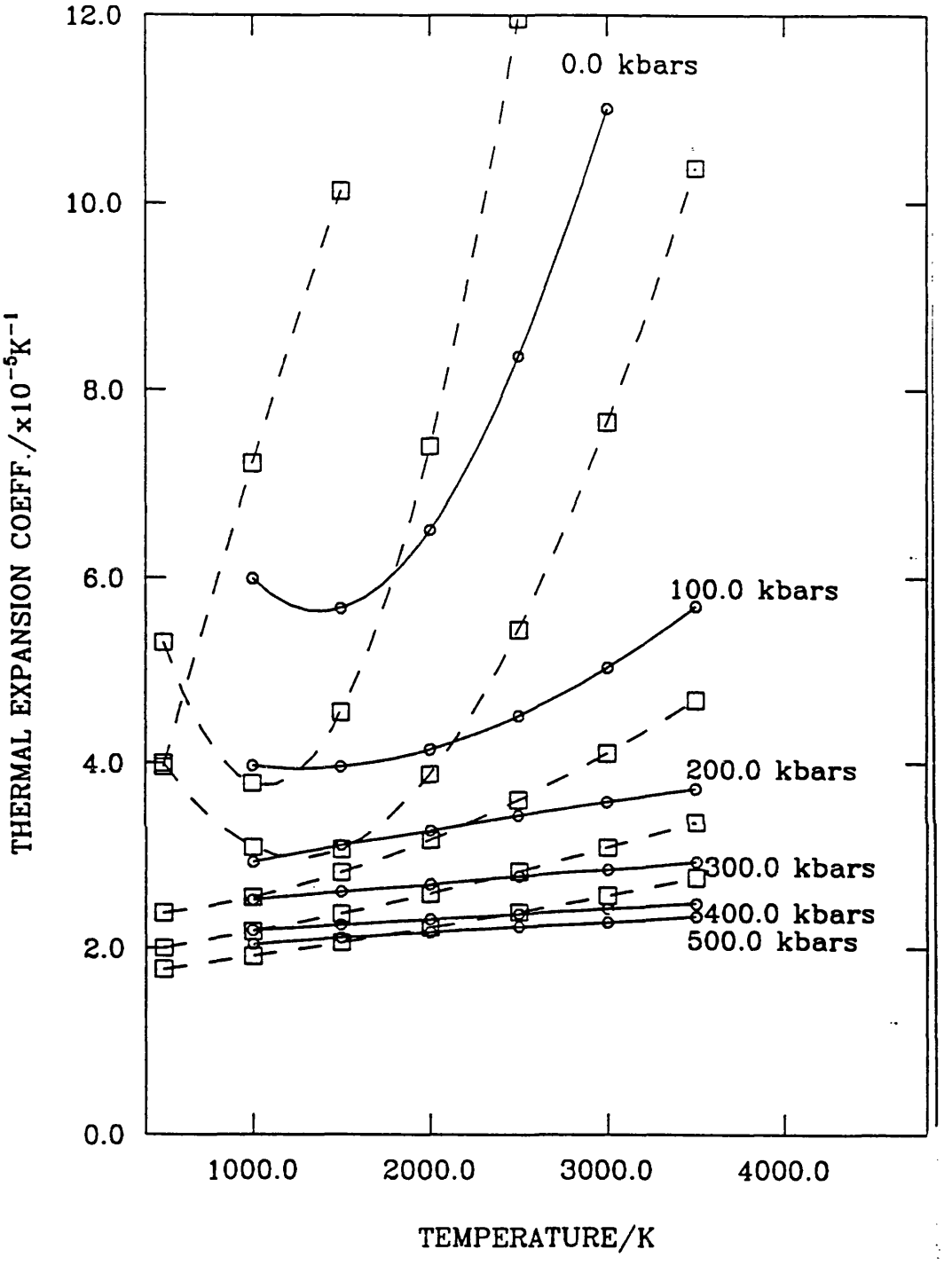

Figure 4.5b Calculated thermal expansion coefficients for MgO.PI (LDS = ------)

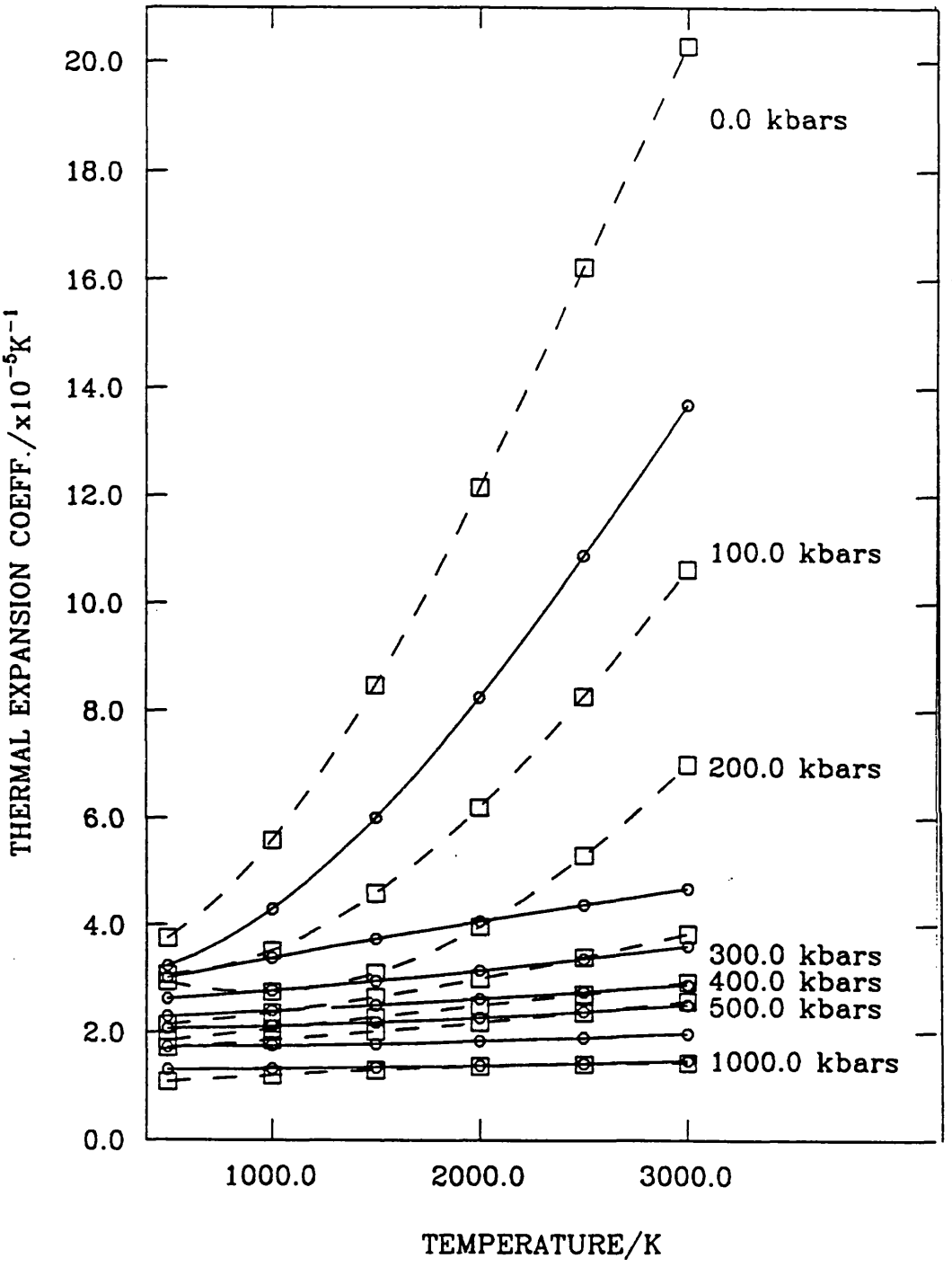

Figure 4.5c Calculated thermal expansion coefficients for $MgSiO_3$ (LDS = ------)

pressures where they meet with the MDS curves. It is for this reason that the thermal expansion curves should also meet at the high pressures, however, due to the uncertainties in the derived values, there is merely a coming together of the LDS and MDS curves and not a superimposition. It is interesting to note how the intrinsic anharmonicity affects the standard measure of extrinsic anharmonicity, namely, the thermal expansion coefficient.

An understanding of the effect of pressure on the thermal expansion of silicates is of great geophysical importance, as it is required in order to calculate mineral densities under mantle pressure and temperature conditions independently of the adiabatic gradient assumption. O. L. Anderson (1967) first showed that the thermal expansion can be related to density, ρ, by the following expression:

$$(\beta/\beta_0) = (\rho/\rho_0)^{-\delta T,} \qquad (4.1)$$

where the subscript 0 denotes room temperature and δ_T is the Anderson-Grüneisen parameter which is assumed to be independent of pressure and the material studied. Experimental and theoretical studies have placed the value of δ_T between 4 and 6, however, the values derived from seismic data give a lower estimate of 2 to 3 (see, Reynard and Price 1990 for references). Our calculated results are presented in Tables 4.2a, b and c, and we immediately see that the MDS values are significantly less than those calculated from the QHA (note we have taken the low temperature values, usually 1500K as our β_0 and ρ_0). Also, there are some "waywardly" high figures (see the low pressures for LDS in particular) and also some low estimates from the MDS model (500kbars MgO.FI, and 0.001 and 100kbars MgO.PI). As explained above, these fluctuations from the expected are probably due to inaccurate fitting, and the curvatures found in the predicted thermal expansion curves could account for some of these. On the whole, we can conclude that the average values for δ_T are 7 to 8 for the calculations based on the QHA and 3 to 4 for the MDS model. This implies that the QHA overestimates the Anderson-

Table 4.2a Calculated Anderson-Grüneisen parameters for MgO.FI

P/kbars	T/K	δ_T (LDS)	δ_T (MDS)
0.001	2000.0	12.75	4.71
100.0	2000.0	8.68	5.13
200.0	2000.0	2.32	2.93
	2500.0	5.04	2.78
	3000.0	6.69	2.65
300.0	2000.0	5.93	8.49
	2500.0	6.47	7.15
	3000.0	6.76	6.04
400.0	2000.0	5.08	4.35
	2500.0	5.18	3.70
	3000.0	5.24	3.12
500.0	2000.0	7.04	1.03
	2500.0	6.60	1.01
	3000.0	6.20	0.98
1000.0	2000.0	9.31	2.63
	2500.0	8.81	2.58
	3000.0	8.35	2.53

Table 4.2b Calculated Anderson-Grüneisen parameters for MgO.PI

P/kbars	T/K	δ_T (LDS)	δ_T (MDS)
0.001	2000.0	5.55	1.42
100.0	2000.0	13.70	1.10
200.0	2000.0	7.04	3.52
	2500.0	10.27	3.26
	3000.0	10.36	3.03
300.0	2000.0	7.67	2.57
	2500.0	7.64	2.43
	3000.0	7.39	2.31
400.0	2000.0	7.37	2.41
	2500.0	7.06	2.30
	3000.0	6.73	2.20
500.0	2000.0	7.36	2.85
	2500.0	7.02	2.72
	3000.0	6.69	2.60

Table 4.2c Calculated Anderson-Grüneisen parameters for $MgSiO_3$

P/kbars	T/K	δ_T (LDS)	δ_T (MDS)
0.001	2000.0	_	10.72
100.0	2000.0	12.07	4.96
200.0	2000.0	11.56	4.31
	2500.0	11.97	4.26
	3000.0	10.97	4.17
300.0	2000.0	8.92	3.67
	2500.0	8.52	3.62
	3000.0	8.02	3.56
400.0	2000.0	8.41	3.37
	2500.0	7.66	3.56
	3000.0	7.01	3.70
500.0	2000.0	8.15	2.99
	2500.0	7.82	3.18
	3000.0	7.47	3.33
1000.0	2000.0	9.85	3.20
	2500.0	8.05	3.47
	3000.0	6.51	3.71

Grüneisen parameters but our data lacks the sufficient accuracy to see if this overestimation is reduced with increasing pressure. Also, there is some definite confirmation that the seismic data are giving the correct order of parameter but refined MDS calculations need to be performed to resolve the debate on this matter. This confirms the statements of D. L Anderson (1987b,1989) that results obtained from laboratory conditions (i.e. moderate pressure and temperature relative to the lower mantle) cannot be extrapolated to the extreme conditions of the mantle. Recent ab initio calculations carried out by Isaak et al. (1992) also suggest that the an increase in pressure decreases the value for δ_S (δ_T). Clearly, these recent developments are favourable for the results obtained from the lateral variations in seismic wave velocities but it is rather early to draw any definite conclusions.

The bulk modulus is a measure of incompressibility and so the greater the magnitude, the bigger the force that is required to compress the crystal. Figures 4.6a, b and c show that the isothermal bulk modulus, K_T, decreases for each pressure. This is correct because as the temperature increases, the crystal expands and the repulsive contribution to the short-range potential is decreased (see equation 2.2), thus making the crystal easier to compress. Similarly, if the hydrostatic pressure is increased, the cell volume reduces and the repulsive interaction increases proportionally to the curvature on the potential energy distribution (see Figure 2.3), subsequently making the crystal more difficult to compress. We have seen that the volume is overestimated at high temperatures in the QHA implying it is easier to compress at these conditions. For this reason, $K_T(\text{LDS}) < K_T(\text{MDS})$ at high temperatures. This effect reduces with increasing applied pressure for the reasons given earlier.

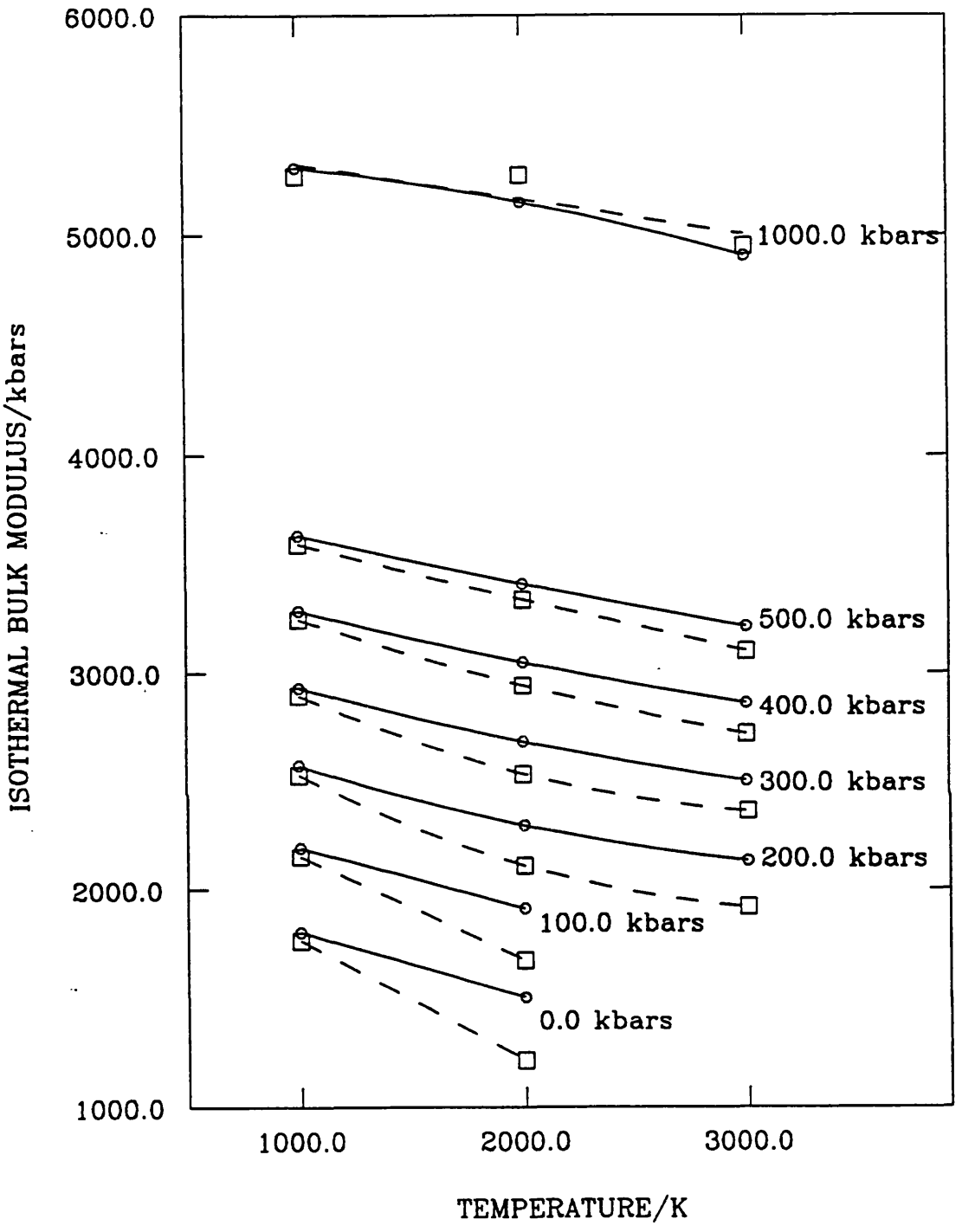

Figure 4.6a Calculated isothermal bulk moduli for MgO.FI (LDS = ------)

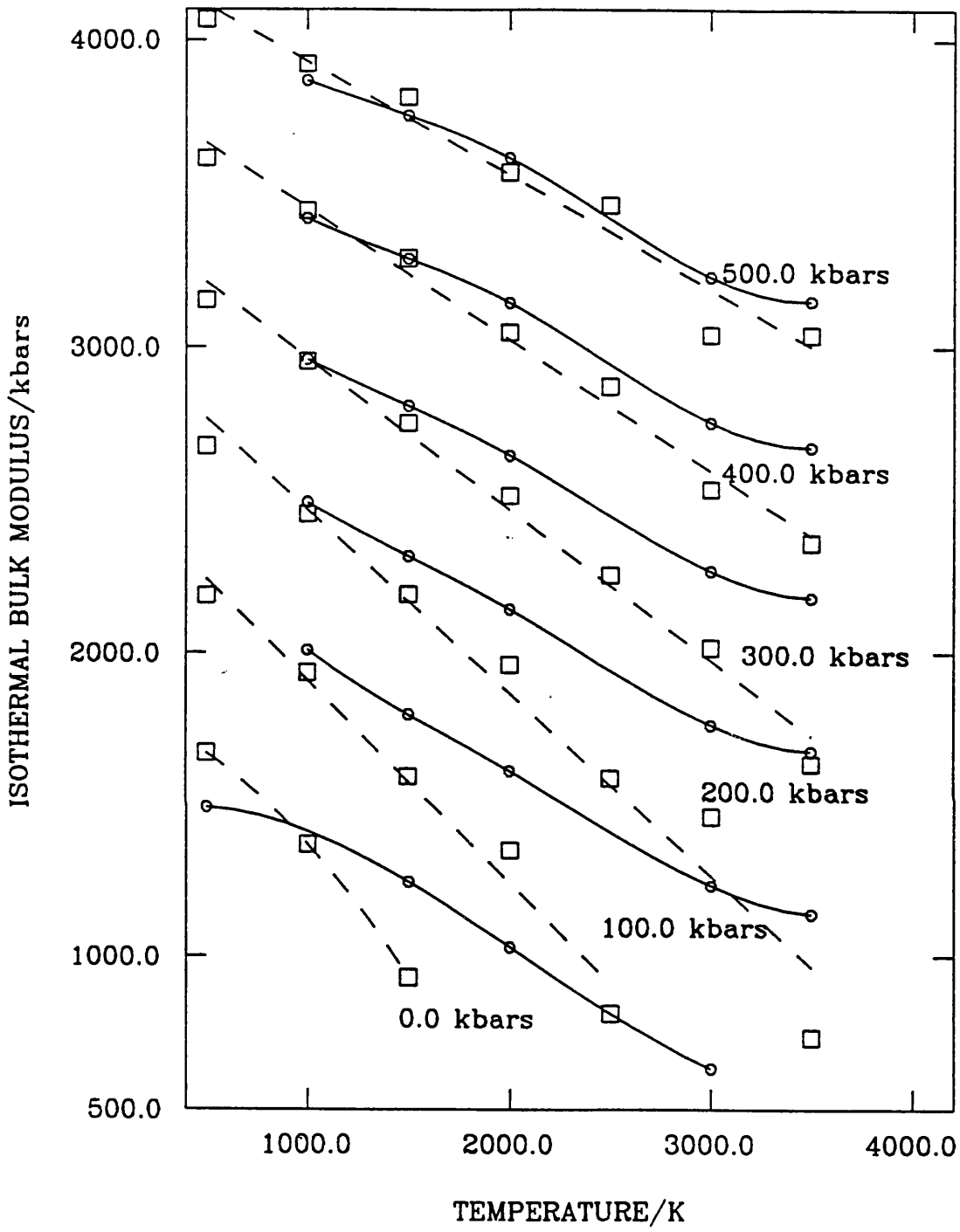

Figure 4.6b Calculated isothermal bulk moduli for MgO.PI (LDS = ------)

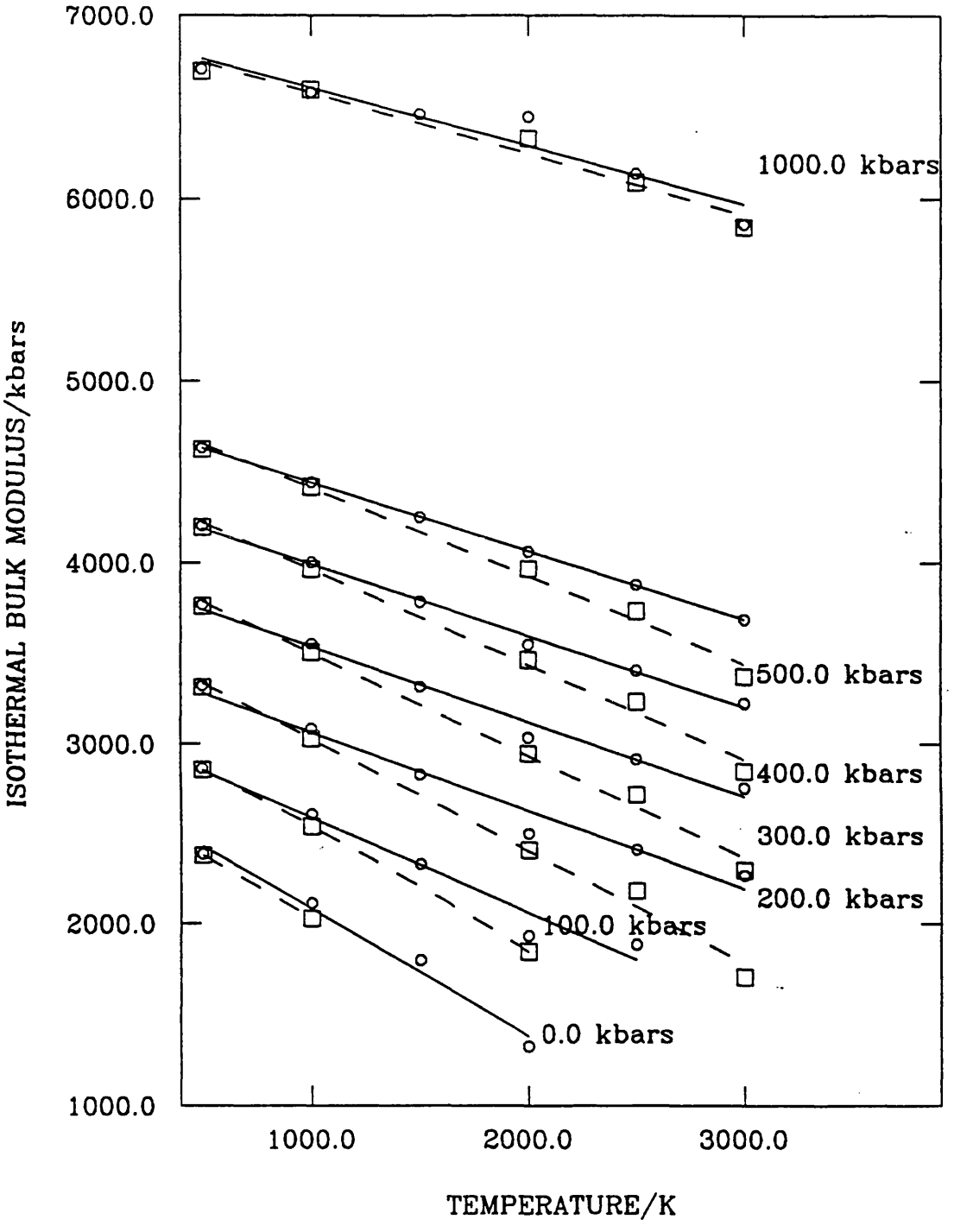

Figure 4.6c Calculated isothermal bulk moduli for $MgSiO_3$ (LDS = ------)

At absolute zero temperature the two heat capacities C_P and C_V are equal. Classically, C_V follows the Dulong-Petit law and takes the constant value of 3NR, where N is the number of species in the formula unit and R is the universal gas constant. Therefore, a useful stability check for a MDS run is to extrapolate the C_P data back to zero kelvin and see if it meets the 3NR limit. The 100kbar dataset for MgO.FI failed to do so and has been removed from Figure 4.7a. There have been other omissions due to "crossovers" which made it difficult to distinguish the individual curves. It must be stressed that the values for the C_P were calculated from the polynomial fitting to enthalpy-temperature data and the differentials involved small changes in enthalpy relative to the absolute values, making the results even more prone to uncertainties. This is obviously a limitation of our methodology and we can only comment on the general trends given by the data obtained from the derivatives, and not the fine details. We see from Figures 4.6a, b and c that C_P increases with T and decreases with pressure as expected from inspection of the enthalpy curves (see Figures 4.4a, b and c). Generally, the LDS data are greater than the MDS values for each pressure except at 1000kbars. Clearly, this follows the same trend as the physical properties studied above implying a reduction of intrinsic anharmonicity at high pressures.

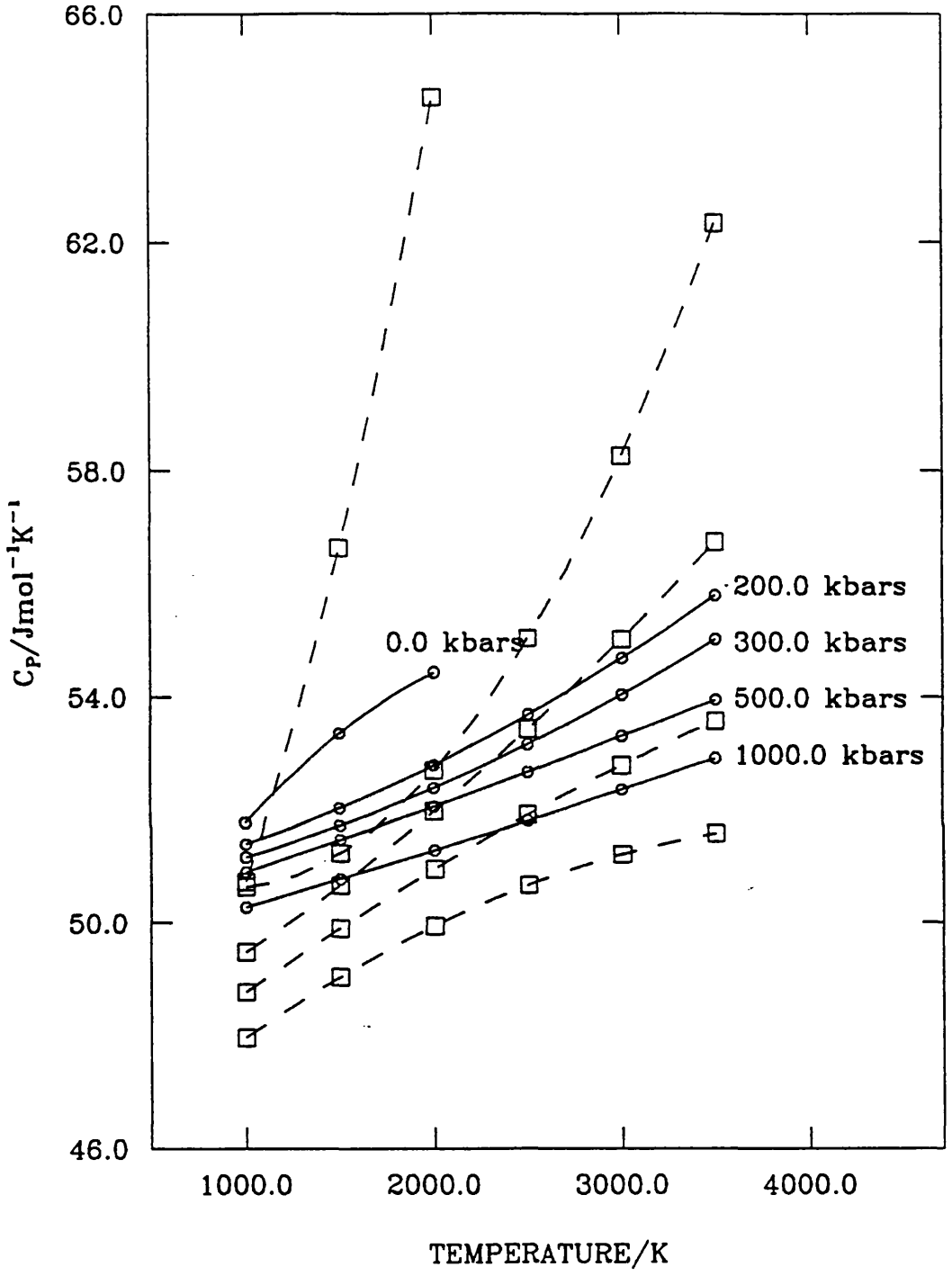

Figure 4.7a Calculated heat capacities at constant pressure for MgO.FI (LDS = ------)

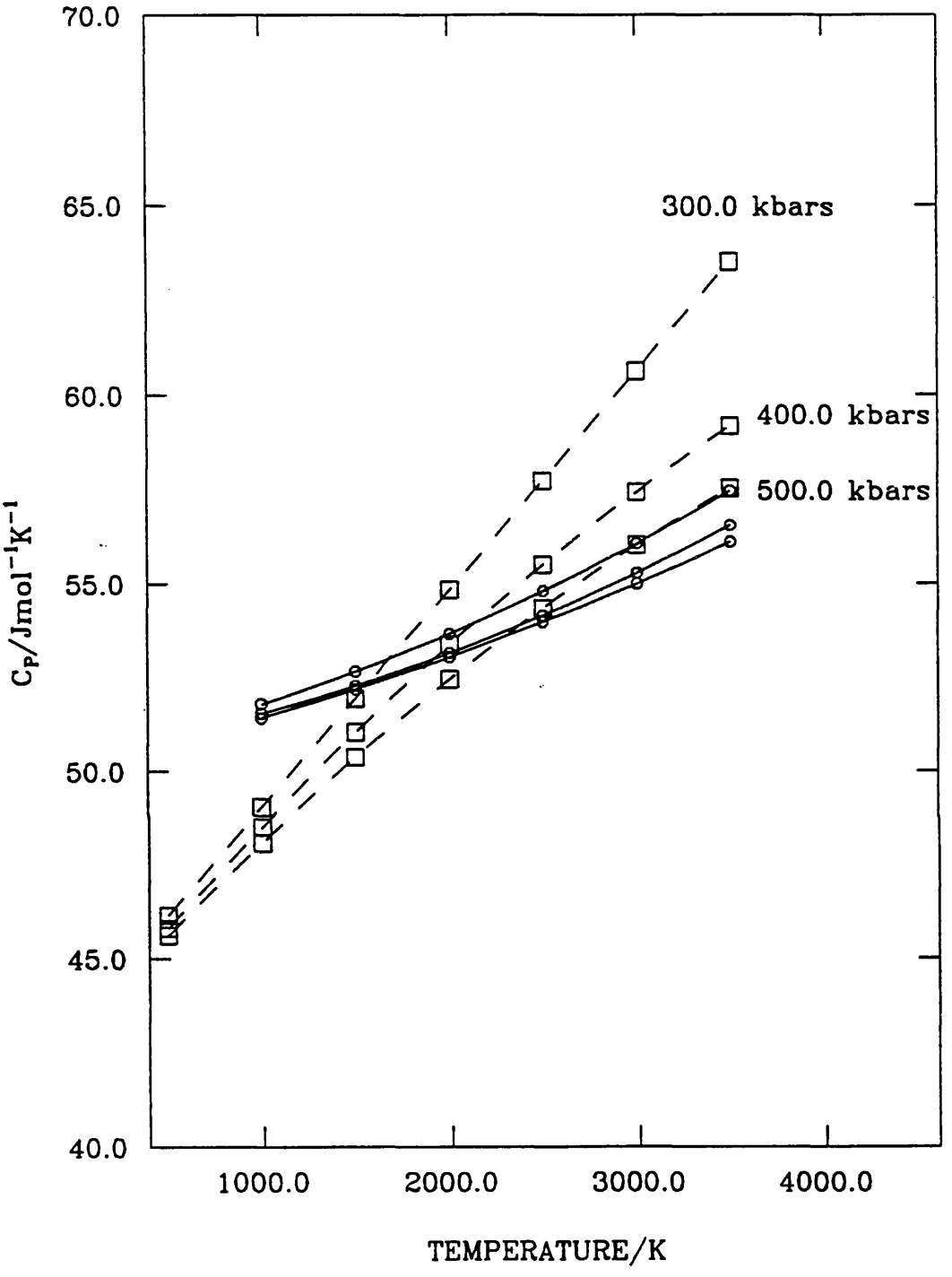

Figure 4.7b Calculated heat capacities at constant pressure for MgO.PI (LDS = ------)

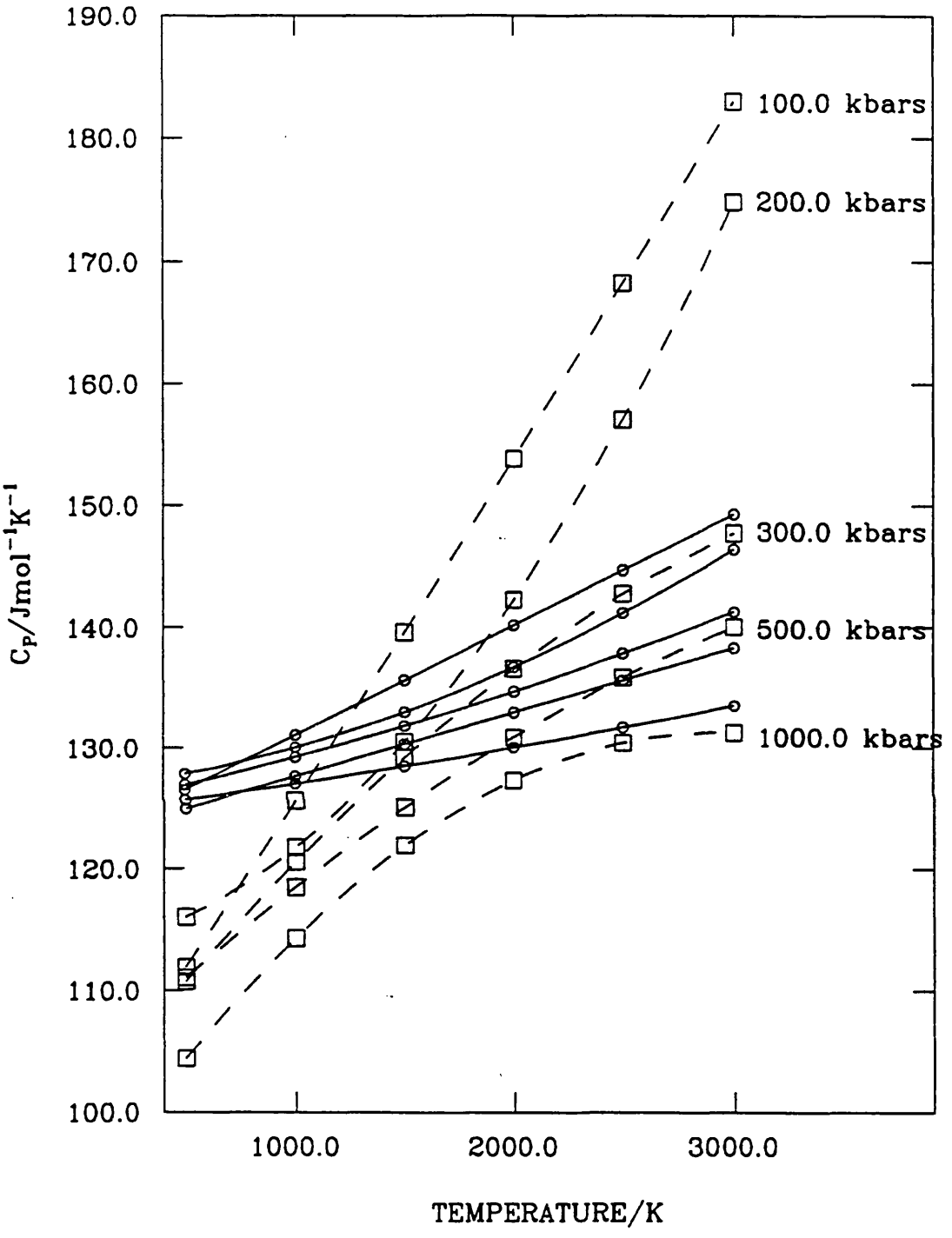

Figure 4.7c Calculated heat capacities at constant pressure for $MgSiO_3$ (LDS = ------)

To highlight the sort of errors involved in our procedure, we have plotted the LDS heat capacities, C_V, calculated from equation 2.45 and superimposed the values obtained from the polynomial fitting method (see Figures 4.8a, b, c and d). We see that agreement is not of the accuracy required for the study undertaken here. However, we have still presented the C_V data (Figures 4.9a, b and c) and the average Grüneisen parameters, γ, (Figures 4.10a, b and c), so that we can see the general trends. The C_V(MDS), on the whole, increase linearly at high temperatures which confirms the prediction from the theory of anharmonic oscillators (see for example, Brüesch 1982). Also, at the lower temperatures the C_V(LDS) tends to zero as expected from equation 2.45. Generally, the Grüneisen parameters decrease with pressure and this is difficult to account for rigorously as there are opposing effects in equation 2.47.

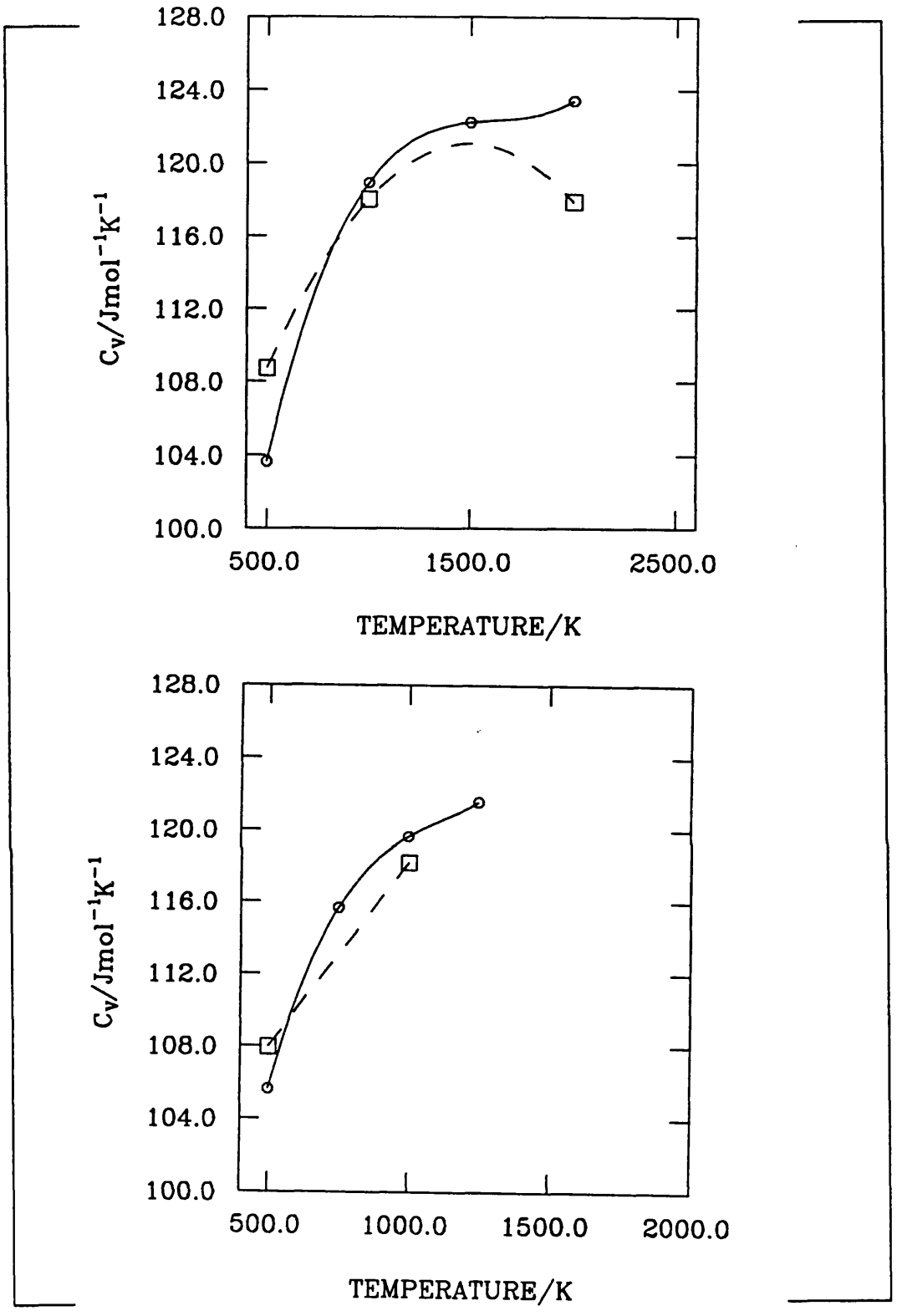

Figure 4.8a Comparison of the LDS calculated heat capacity at constant volume for $MgSiO_3$ at 0.001 and 100.0 (top plot) kbars pressure. Solid line is C_v calculated from Equation 2.45.

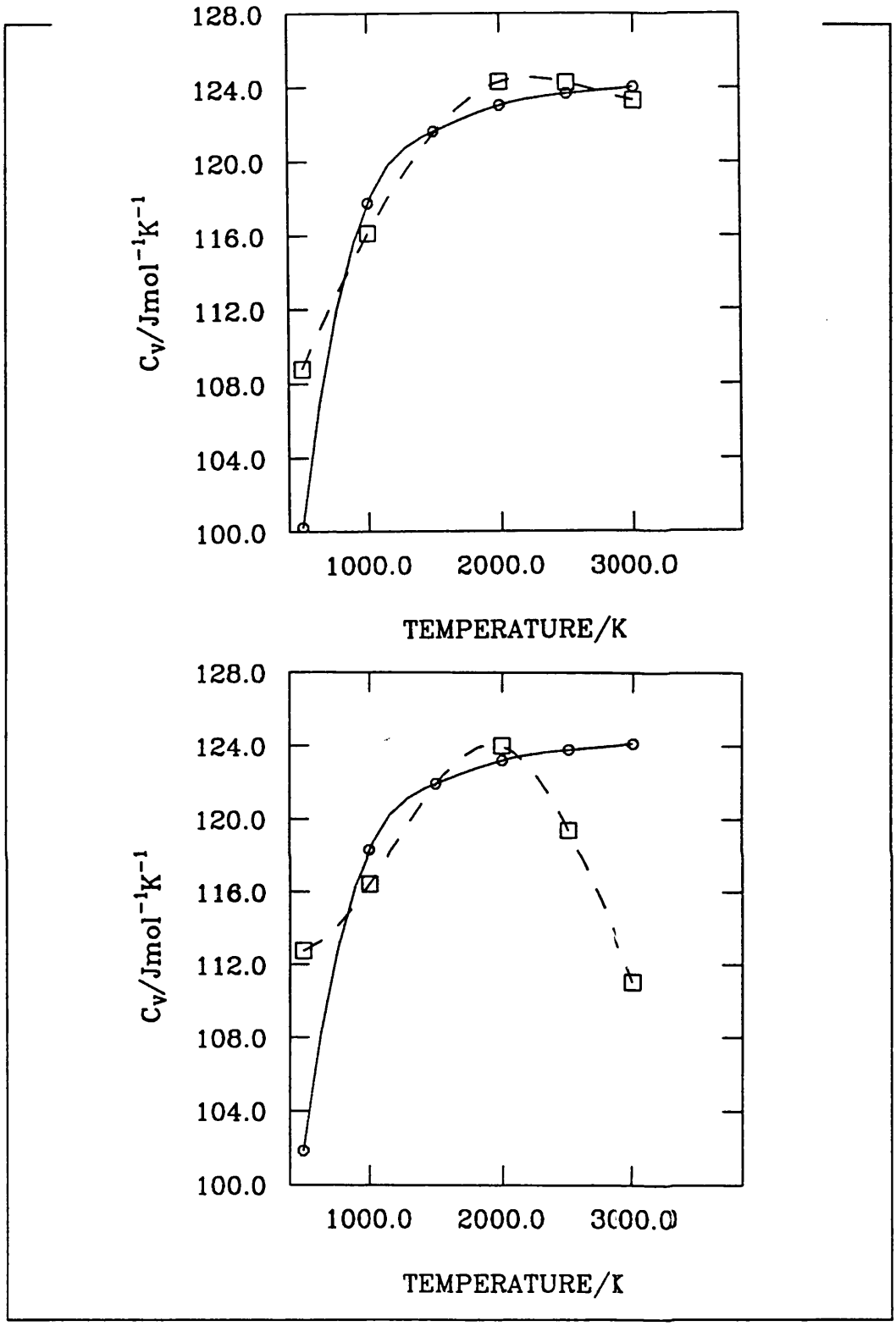

Figure 4.8b Comparison of the LDS calculated heat capacity at constant volume for $MgSiO_3$ at 200.0 and 300.0 (top plot) kbars pressure. Solid line is C_v calculated from Equation 2.45.

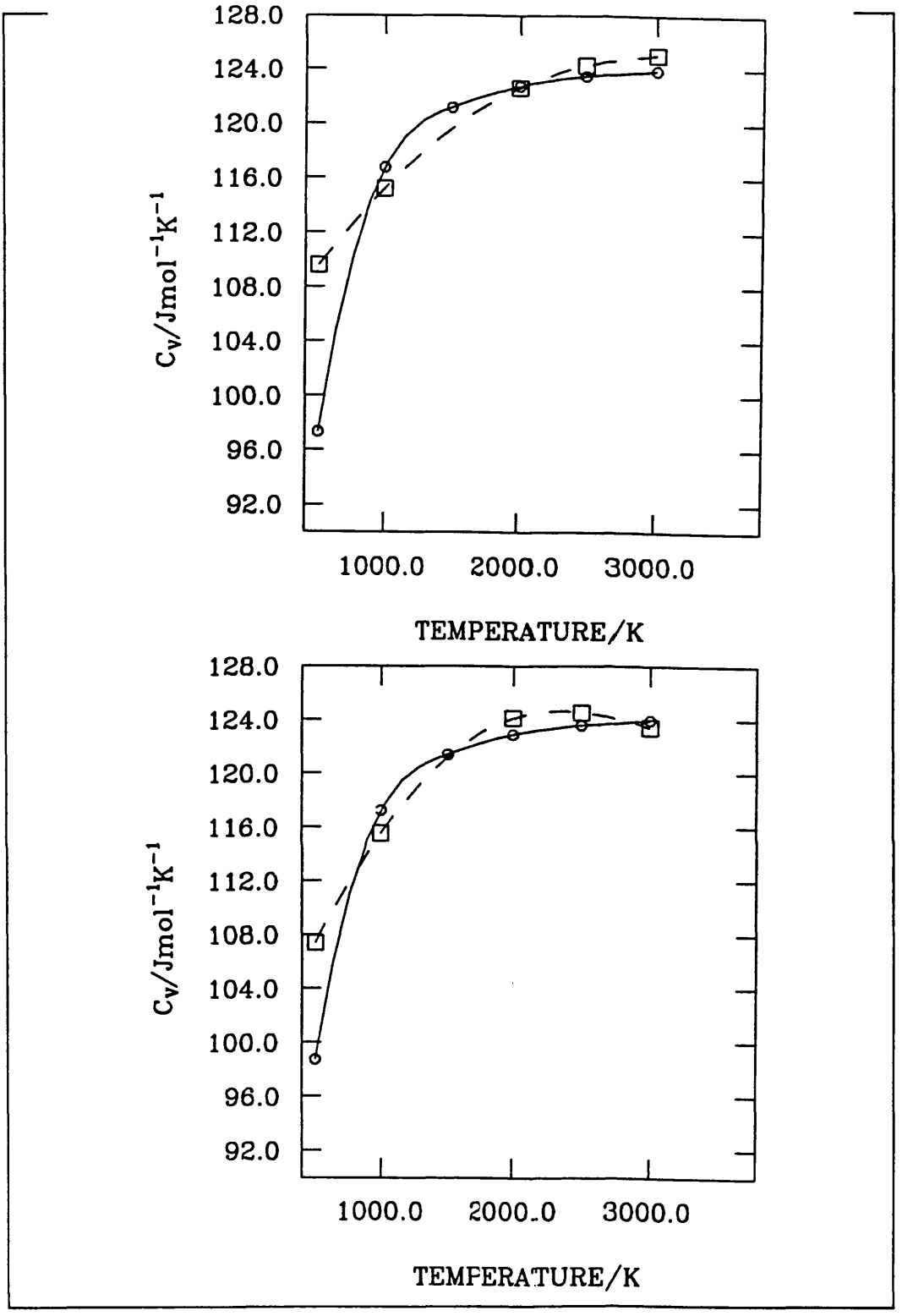

Figure 4.8c Comparison of the LDS calculated heat capacity at constant volume for $MgSiO_3$ at 400.0 and 500.0 (top plot) kbars pressure. Solid line is C_v calculated from Equation 2.45.

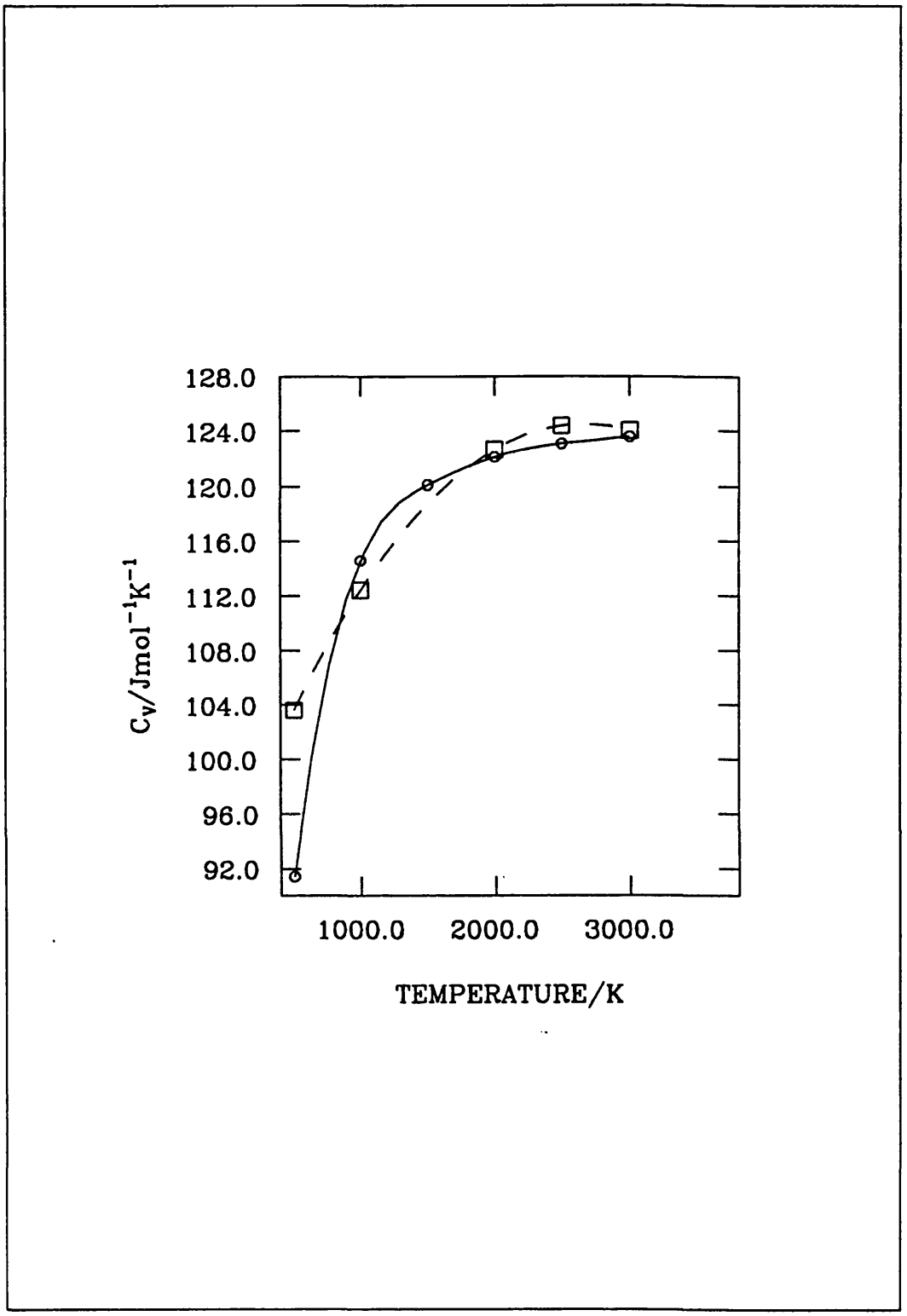

Figure 4.8d Comparison of the LDS calculated heat capacity at constant volume for $MgSiO_3$ at 1000.0 kbars pressure. Solid line is C_V calculated from Equation 2.45.

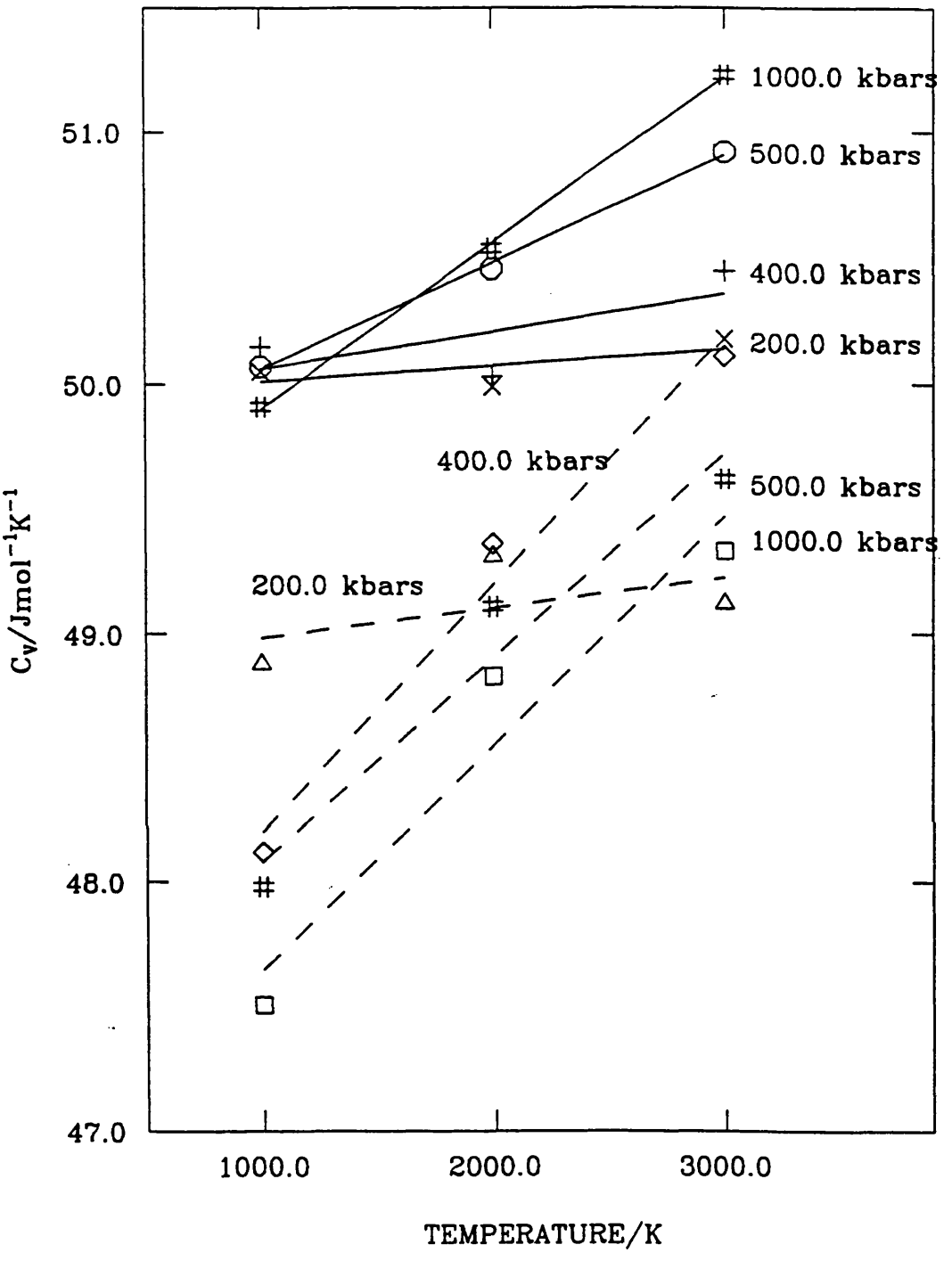

Figure 4.9a Calculated heat capacities at constant volume for MgO.FI (LDS = ------)

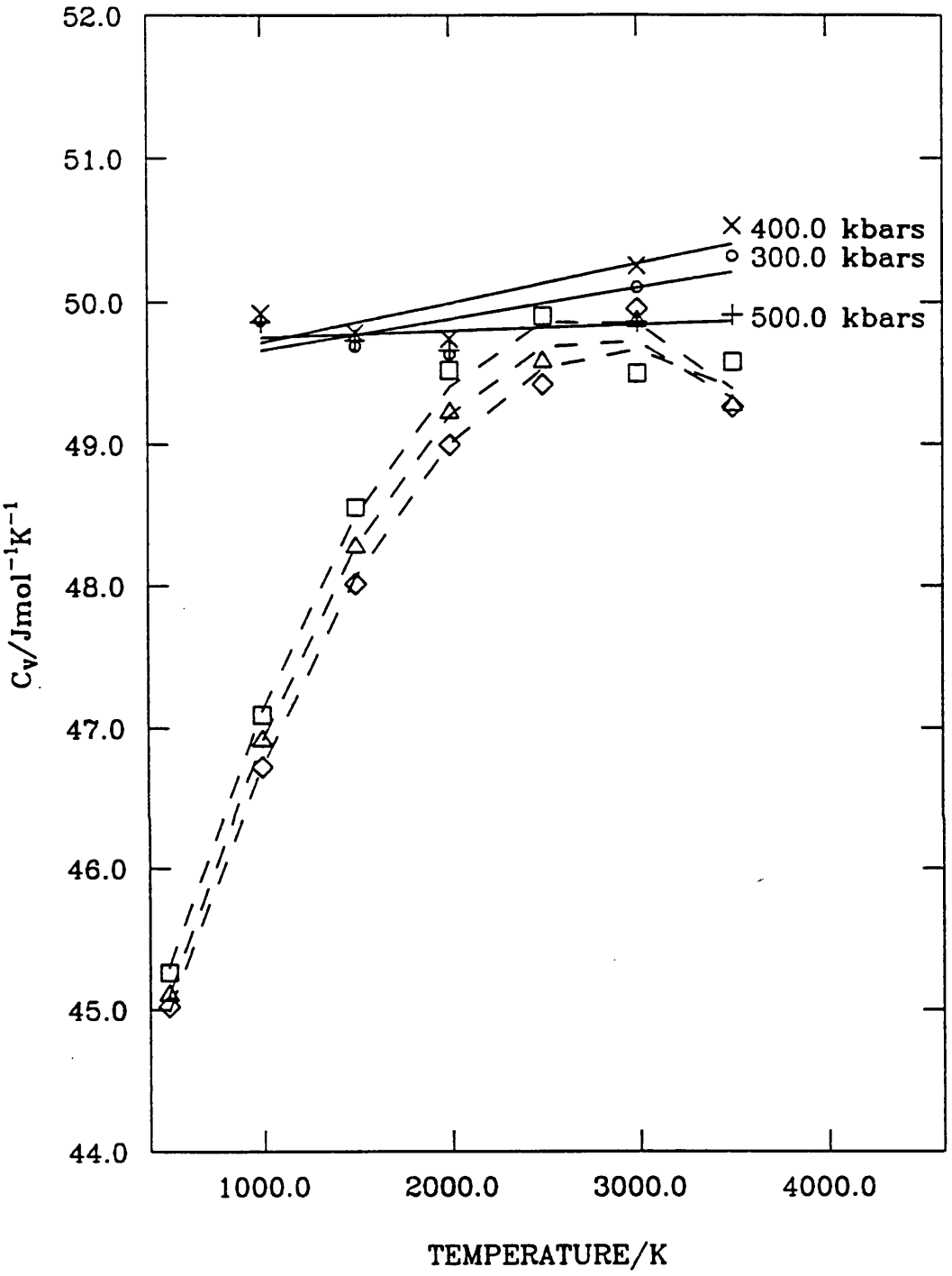

Figure 4.9b Calculated heat capacities at constant volume for MgO.PI (LDS = ------).
LDS: Squares = 300 kb, triangles = 400 kb and diamonds = 500 kb.

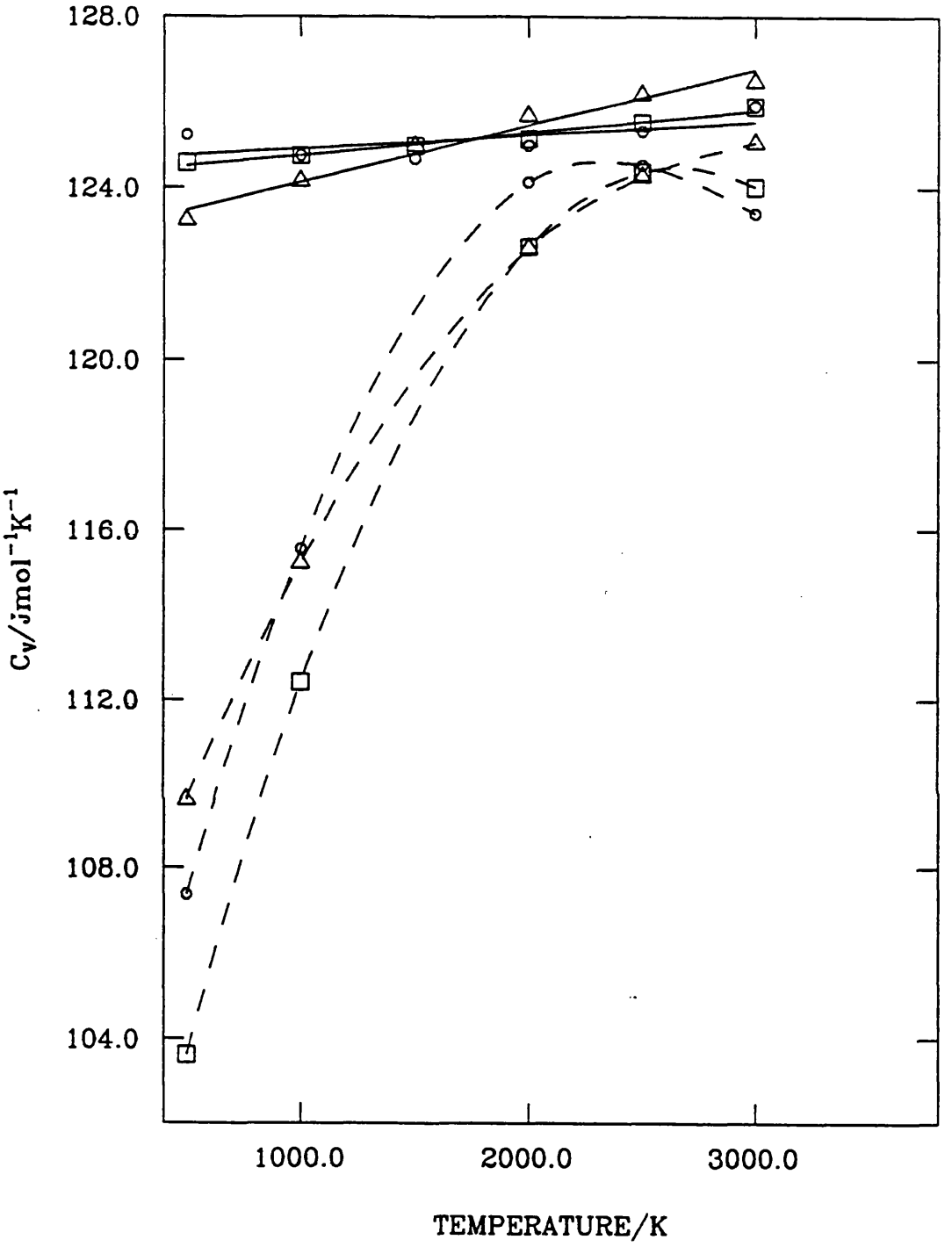

Figure 4.9c Calculated heat capacities at constant volume for $MgSiO_3$ (LDS = ------). Circles = 400 kb, triangles = 500 kb and squares = 1000 kb.

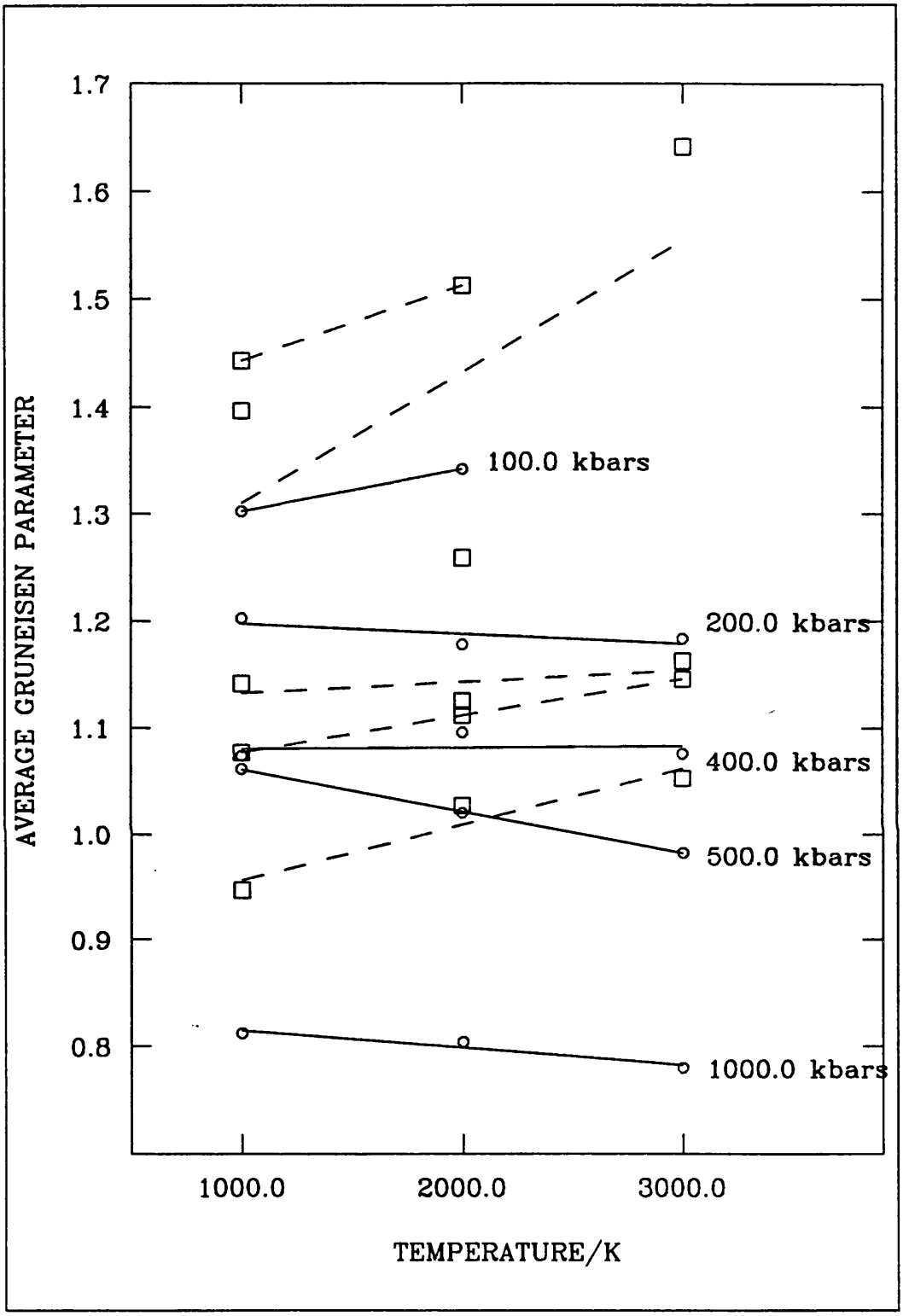

Figure 4.10a Calculated average Grüneisen parameters for MgO.FI (LDS = ------)

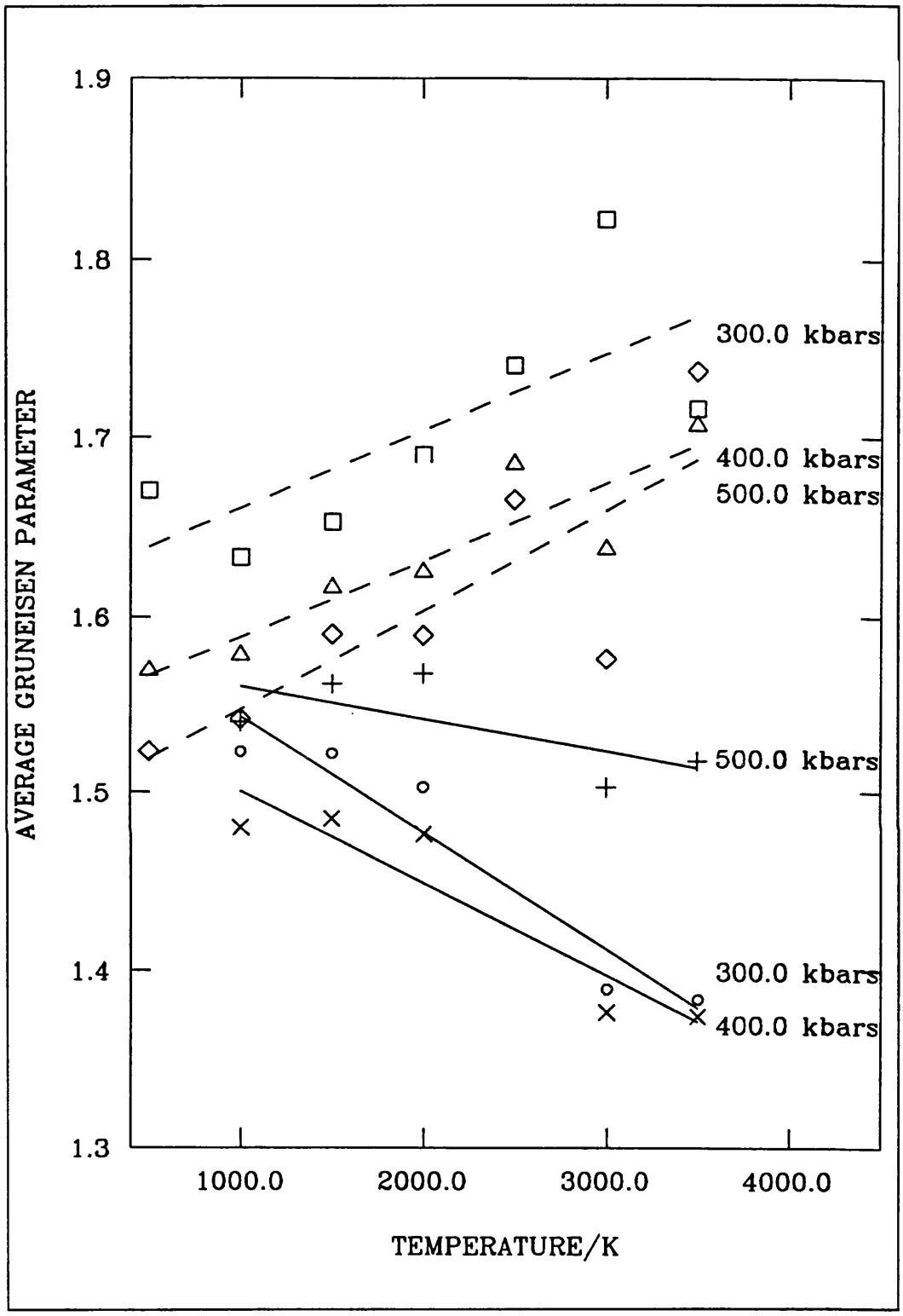

Figure 4.10b Calculated average Grüneisen parameters for MgO.PI (LDS = ------)

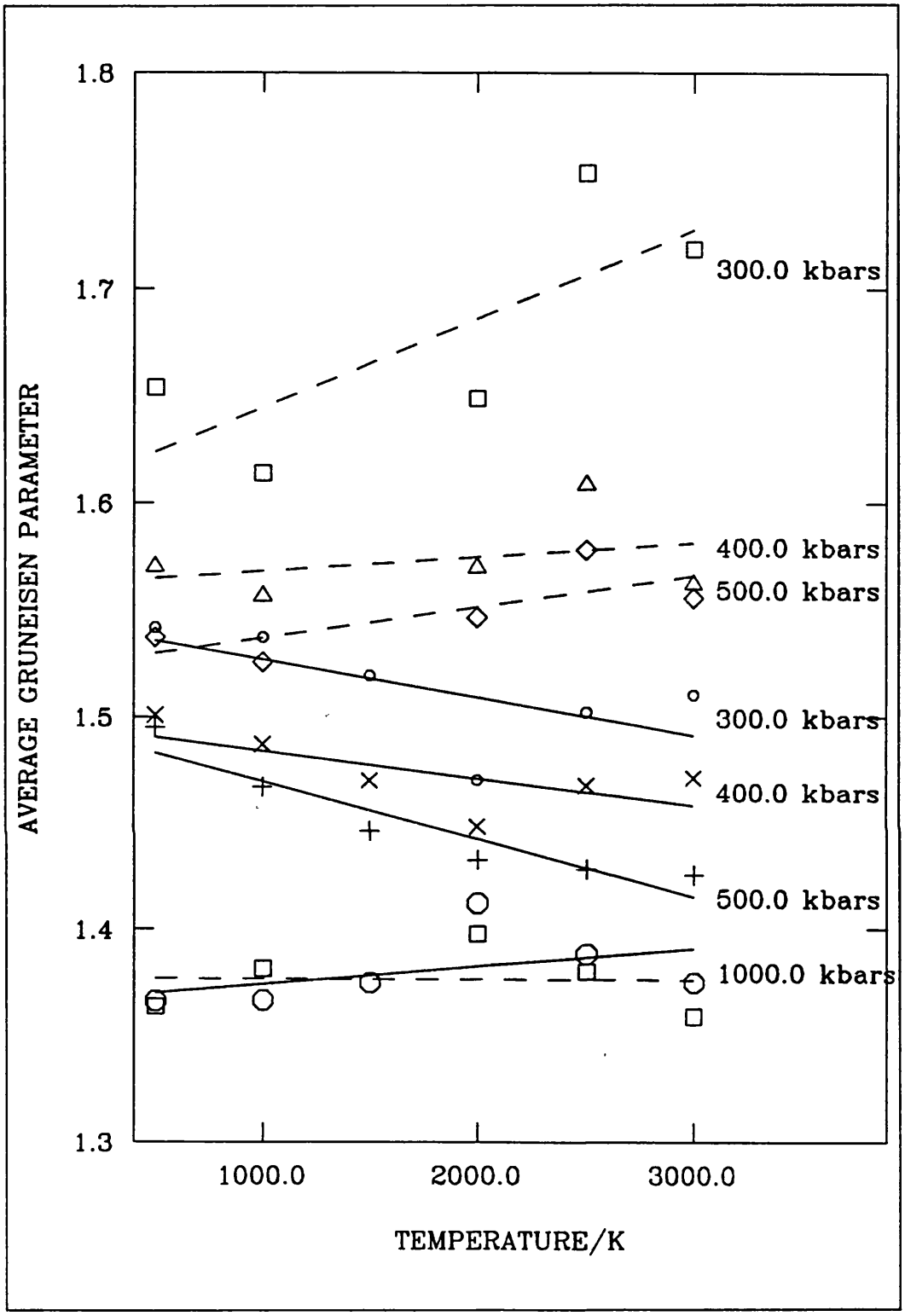

Figure 4.10c Calculated average Grüneisen parameters for $MgSiO_3$ (LDS = ------)

Finally, to conclude this section we have composed percentage deviation plots of the QHA from the intrinsically anharmonic molar volume, thermal expansion and isothermal bulk modulus. These plots (see Figures 4.11, 4.12 and 4.13) are shown for MgO.FI only so that this provides an example of the sort of corrections needed if calculations based on the QHA are performed. At high temperatures and pressures the LDS calculations should be corrected for 0.25% in the molar volume, 15% in the thermal expansion and 5% in the isothermal bulk modulus. Geophysically, this implies that the MDS technique is necessary for the upper mantle conditions (at all temperatures) and the LDS approach is limited to the lower mantle (all temperatures) and low temperature studies in the upper mantle. Recent theoretical developments on phonon-phonon interactions and the anharmonic potential energy function have led to models which could significantly improve the current LDS approach and give a good description of high temperature phenomena. This progress has been reported in Ball (1989) and Brüesch (1982) along with finite-temperature perturbation theory to phonons in a quantised crystal lattice, self-consistent phonon theory and nonpolynomial field theories.

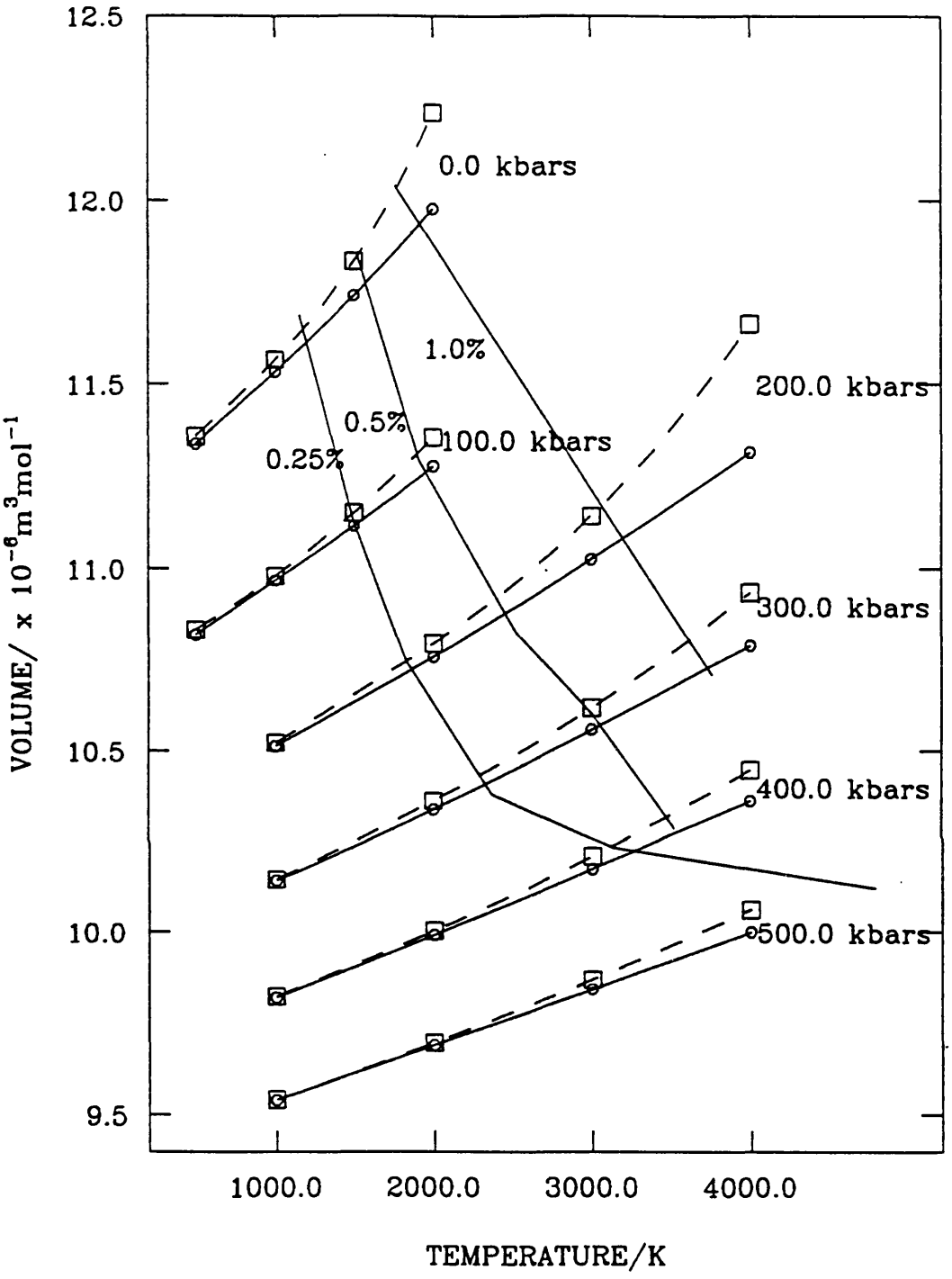

Figure 4.11 Deviation (LDS model away from the MDS model) contours (0.25%, 0.5% and 1.0%) for the molar volume of MgO.FI. (LDS = ------)

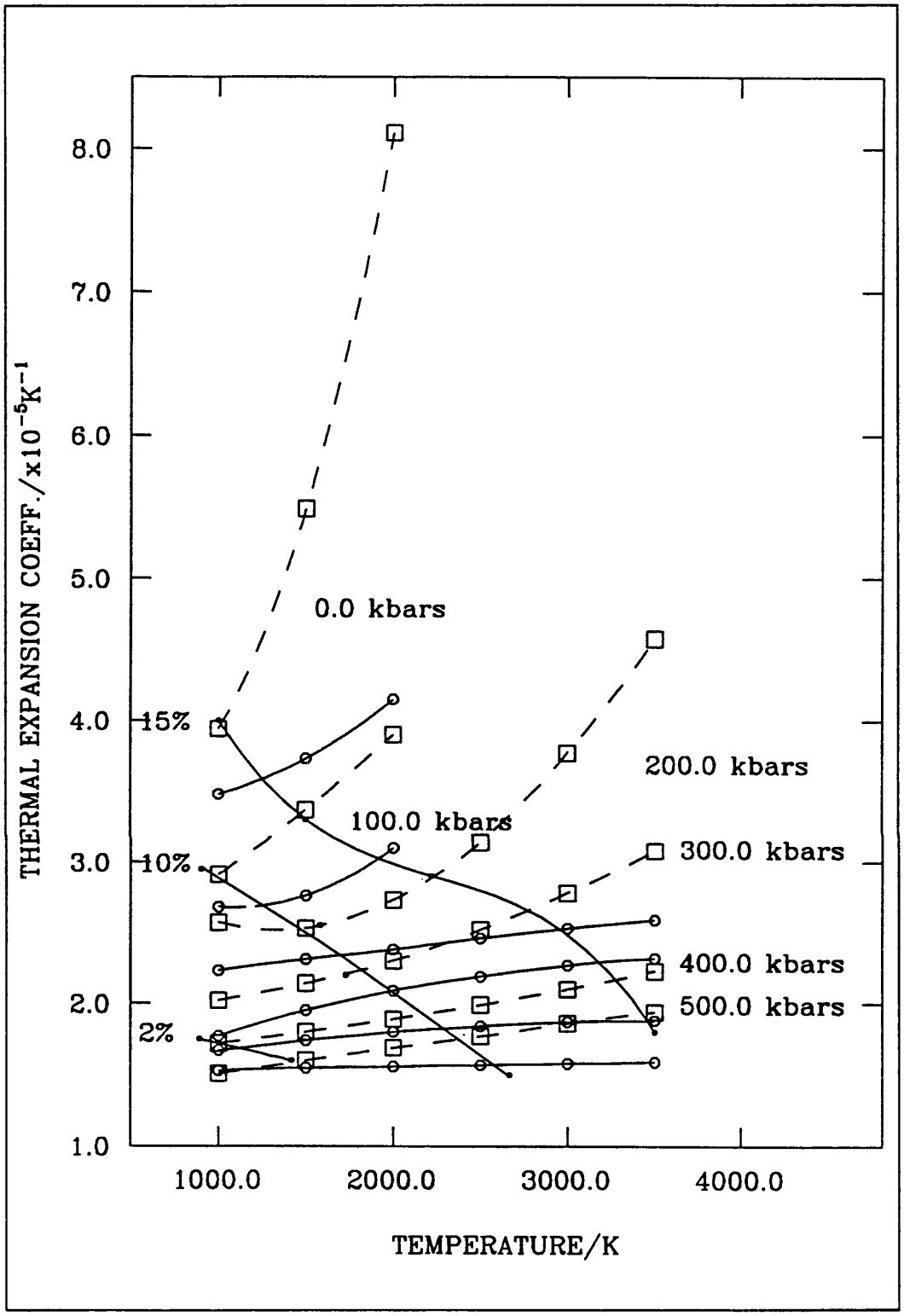

Figure 4.12 Deviation (LDS model away from the MDS model) contours (2%, 10% and 15%) for the thermal expansion coefficient of MgO.FI. (LDS = ------)

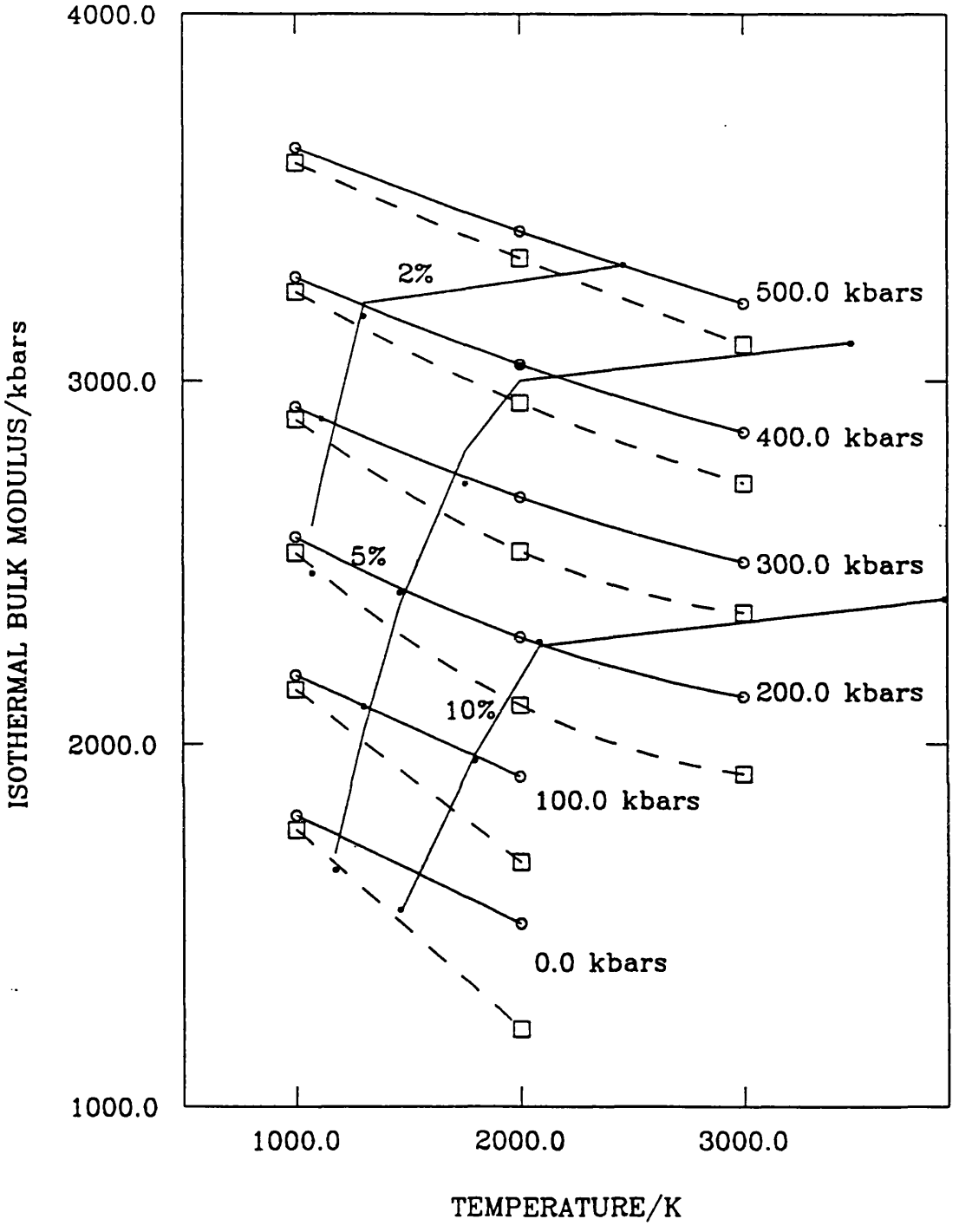

Figure 4.13 Deviation (LDS model away from the MDS model) contours (2%, 5% and 10%) for the isothermal bulk modulus of MgO.FI. (LDS = ------)

4.4 Summary

We have compared calculations based on the QHA with corresponding MDS (i.e. intrinsic anharmonicity included) derived results for MgO and $MgSiO_3$. It has been clearly shown that the QHA breaks down at high temperatures and low pressures and this deviation from the "true" values is reduced when the external pressure is increased. In fact, for the molar volume, enthalpy and isothermal bulk modulus the two approaches converge at very high pressures implying that the intrinsic anharmonic effects are negligible at these conditions. It has also been demonstrated that the major shortcoming of our methodology was insufficient data. Sampling at many more points in P-T space is necessary so that precise polynomial fits could be achieved in order to calculate other physical properties with minimal uncertainty. We did not pursue this line because many of the MDS runs were taking thousands of seconds (varying between 1000 to 6000) on the CRAY/CONVEX supercomputers and our limited resources could not cope with this demand. On the whole, the effects of intrinsic anharmonicity reduces the Anderson-Grüneisen parameters and this has the possible conclusion that the experimental values derived from seismic data implicitly include such effects, explaining why they are generally lower than the values found from other experimental procedures. Finally, we gave quantitative estimates of the errors one would find for the molar volume, thermal expansion and isothermal bulk modulus, if calculations based on the QHA were used. We found that it was necessary to use the MDS technique for upper mantle conditions and the LDS model is limited to the lower mantle although, in the near future, improvements can be made via the theory of phonon-phonon coupling to remove such restrictions.

CHAPTER FIVE

QUANTUM MECHANICAL SIMULATIONS OF SILICATES

5.0 Introduction

The obvious limitation of the atomistic modelling approach is the dependency on empirical fitting for suitable potential energy distributions of the system under study. This can be overcome by adopting so-called "a priori" methods for calculating the potential energy surface for a variety of geometries and then deriving the necessary information from a least-squares fitting to the surface. To penetrate beyond the atomistic realm we have to go into the subatomic world of electrons and nuclei. Unfortunately, the exact solution for the many-electron atom or molecule has not yet been discovered due to the additional interaction terms arising in the Hamiltonian, hence, restricting the separation of variables approach for the solution of the Schrödinger differential equation. This has not hindered progress on the approximate solutions of many-body systems and these have been extended to investigate periodic structures (see for example, Nada et al. 1990; Cohen et al. 1989). In the next section we discuss the approximations employed in the CRYSTAL code (Pisani et al. 1988; Dovesi et al. 1988) which is used for preliminary optimised geometry calculations for the idealised cubic $MgSiO_3$ perovskite. As was stated in the previous chapter, $MgSiO_3$ perovskite is probably the most abundant mineral in the Earth (80% of the lower mantle) and so the study of its electronic nature is of immediate importance. The results are discussed in section 5.2 and the summary and conclusions are presented in the final section.

5.1 Outline of model

In this section, a brief discussion of the quantum mechanical model for crystal structures, as used by the CRYSTAL program, will be given. As stated above, approximations are necessary for the solution of the many-electron molecule which we will now outline. The Schrödinger equation for the many-electron molecule is set up for the non-relativistic time-independent case and it is only possible to treat the ground state energy and not the excited (i.e. temperature dependant) states due to the complexity of the equations. In the Born-Oppenheimer approximation the nuclei are assumed to respond considerably more slowly (due to their heavier masses) than the electrons which further simplifies the Hamiltonian of the system by neglecting the kinetic energy of the nuclei. The Schrödinger equation can now be split into a set of linear one-electron molecule equations which can be solved for the ground state energy if the eigenfunctions (i.e. molecular spin-orbitals, MO) are known. This is achieved by constructing a trial MO from a linear combination of atomic orbitals (LCAO - which arise from the exact solutions of the hydrogen atom) and applying the variation theorem to calculate the minimum energy. These calculations are performed at the Hartree-Fock (HF) level of approximation where the one-electron Hamiltonians are replaced by the effective Hamiltonians which are perturbations from the one-electron case, and contain an average potential term to account for the average field of all the other electrons. The average potential is readily calculated from the MO (see, for example, George 1972) and through a series of iterations it is possible to calculate the potential which reproduces the eigenfunctions that determined it. This type of calculation is called a self-consistent field (SCF). The extension of this treatment to a periodic structure is achieved by imposing the periodic conditions on the eigenfunctions which gives, what are commonly called, the Bloch functions. The crystal orbitals (CO) are then constructed out of these Bloch functions from the LCAO method where Gaussian-type orbitals (GTO) are input along with their exponents and contraction coefficients (see, Hehre et al. 1969) to provide convenient approximations of the hydrogen-like solutions. The number of Gaussian functions used to construct the atomic orbitals of all the electrons of an atom

constitutes a resulting basis set for that atom in the crystal structure. Hence, the size of basis set is the computing limitation of CRYSTAL and calculations for large unit cell structures cannot yet be implemented. Within these approximations the motions of the individual electrons are not correlated and this is an obvious source for inaccurate ground state energies. Nevertheless, it is still possible to employ this procedure to study relative differences in energies (especially for different geometries of the same material) and can also provide insight into the nature of the bonding (see, for example, Nada 1990). In the next section we discuss the results of the HF-LCAO periodic calculations of cubic $MgSiO_3$-perovskite.

5.2 Results and Discussion

The establishment of a reliable, well balanced set of basis functions to describe the atomic species of the system under investigation, is an essential preliminary step of the calculation. We have used the basis functions which were originally variationally (i.e. the outer shell exponent is varied until a minimum energy is achieved) optimised for the $MgSiO_3$ ilmenite structure (see, Nada 1992a) as a starting point for our study. The basis set (b.s.) for each atomic species of the crystal structure is referred to by the standard notation, X-YZ A, adopted by Pople and his co-workers (see, for example Hehre et al. 1969) where X, Y and Z are the number of functions in the last three shells of the atom, and A is the type of function (Gaussian in our case). Hence, we have used a 8-61 G b.s. for the magnesium atom, an 8-51 G b.s. for oxygen and a modified 6-21 G b.s. for the silicon atom. For a more detailed discussion of the validity and accuracy of these basis set functions we refer the reader to Nada (1992a).

The above mentioned basis sets were variationally re-optimised for the cubic $MgSiO_3$ perovskite context, however, it was not necessary to optimise the outer shell exponent for the Mg atom as previous studies have shown (see, Nada 1992a) only minute energy differences for such changes, implying that the atom retains its highly ionic character as previously established for this b.s. It is worth noting that

the convergency test on the energy was set to a difference of 10^{-8} between the two consecutive SCF cycles. The outermost shell Gaussian function was omitted from the Si atom resulting in a 6-62 G b.s. as this was found to give convergent energies at a variety of tolerances (i.e. the accuracy cut-offs for the integrals). Therefore, there are two Gaussian functions which are modelling the sp valence functions and the optimised exponents are shown in Figure 5.1a. Similarly, for oxygen we have optimised the outermost sp shell Gaussian function and also the previous function (i.e. the last one of the 5 GTO group) and these results are shown in Figure 5.1b. It is important to note that the sequence of optimisation is always from the innermost function (core electrons) to the outer (valence electrons) as this provides as systematic method for avoiding unnecessary correlations. These calculations typically required 1000 seconds cpu time on the CONVEX supercomputer and were performed with the following tolerances (expressed as $-\log_{10}$ [x]:

Coulomb overlap tolerance = TOL1	6
Coulomb penetration tolerance = TOL2	6
Exchange overlap tolerance = TOL3	6
Exchange pseudo overlap (g sum) = TOL4	6
Exchange pseudo overlap (n sum) = TOL5	16

The meaning of these truncation parameters require a detailed discussion of the theoretical technicalities which is beyond the scope of this chapter, and so we refer the interested reader to Pisani et al. (1988). With the energy-minimised exponents for all the b.s the cell parameter was variationally optimised to give the best possible cell volume. Figure 5.2 shows the energy curves for the re-optimised b.s. (BS1) and the original b.s. (BS2) and we see little difference the re-optimisation makes possibly implying the transferability of b.s. from one symmetry to another. However, one would expect serious distortions in the electron clouds (i.e. b.s.) if the transfer is between two largely dissimilar geometries (e.g. cubic to triclinic). In Table 5.1 the energy and cell volume calculated for BS1 and BS2 are given. The bulk modulus is calculated from the second derivative of energy with volume (i.e. the curvature of the plots in Figure 5.2) and they are also presented in the

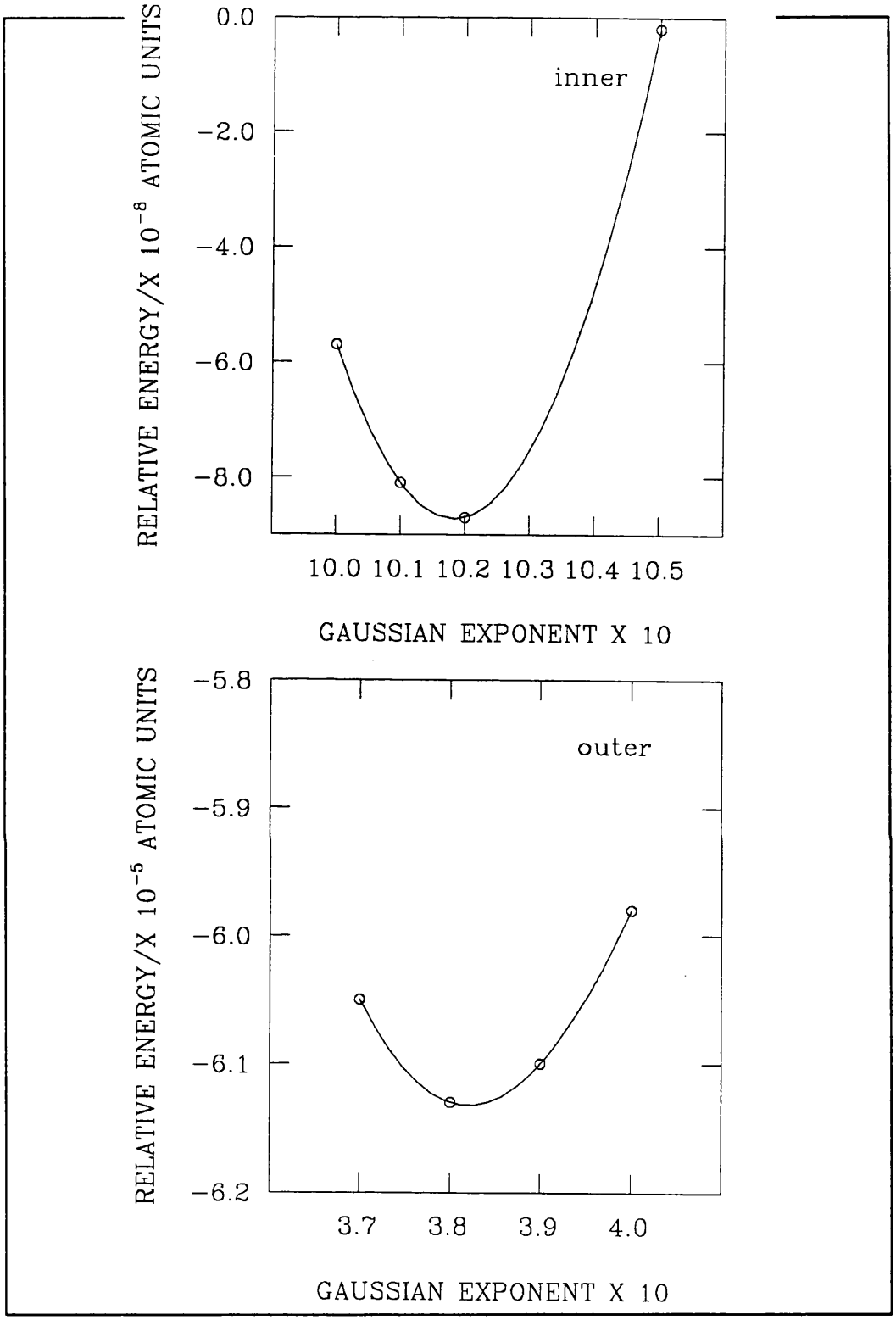

Figure 5.1a Variationally optimised inner and outer exponents of silicon. (Note the energies are not the absolute values but the significant figures after the eighth (inner) and fifth (outer) decimal places).

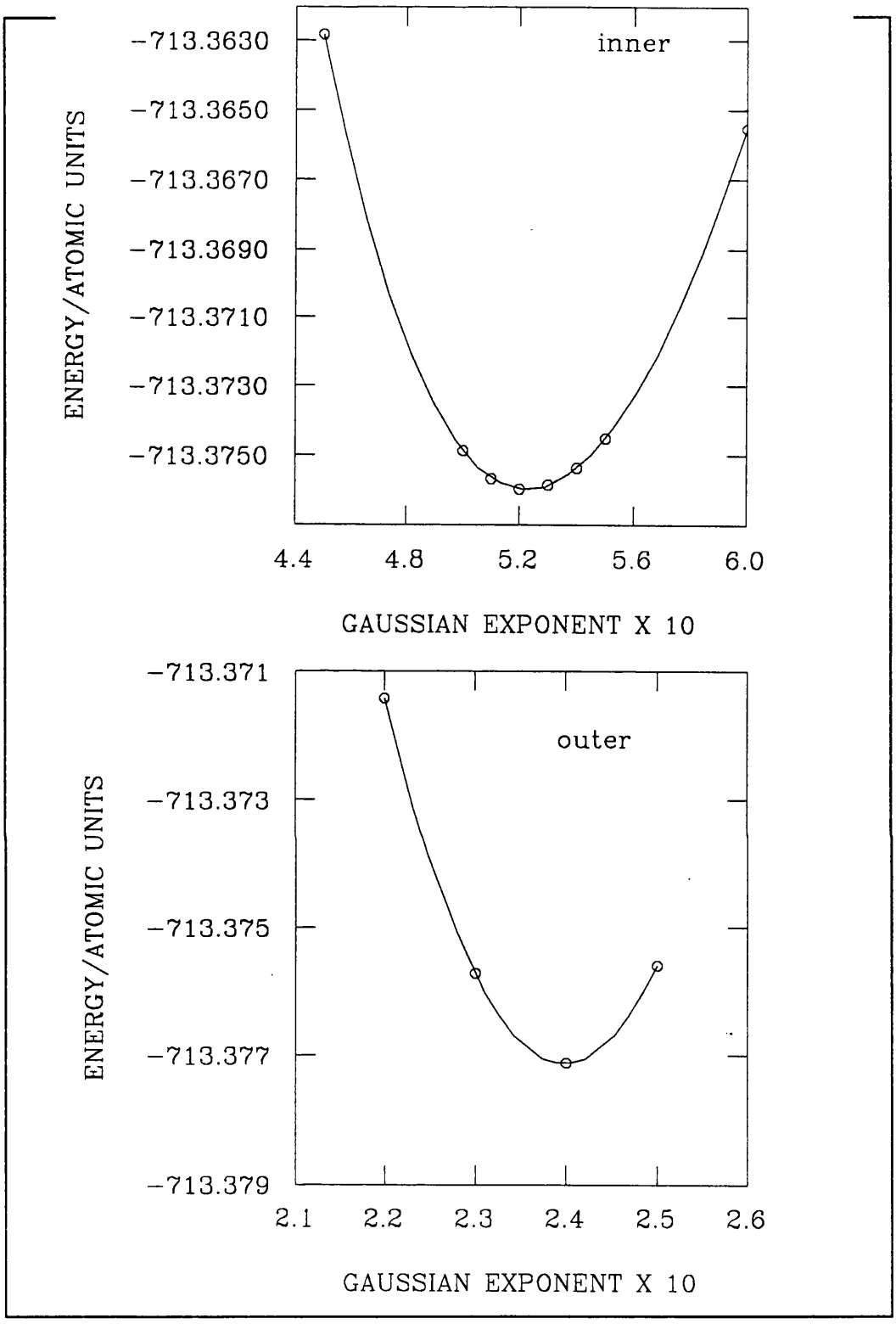

Figure 5.1b Variationally optimised inner and outer exponents of oxygen.

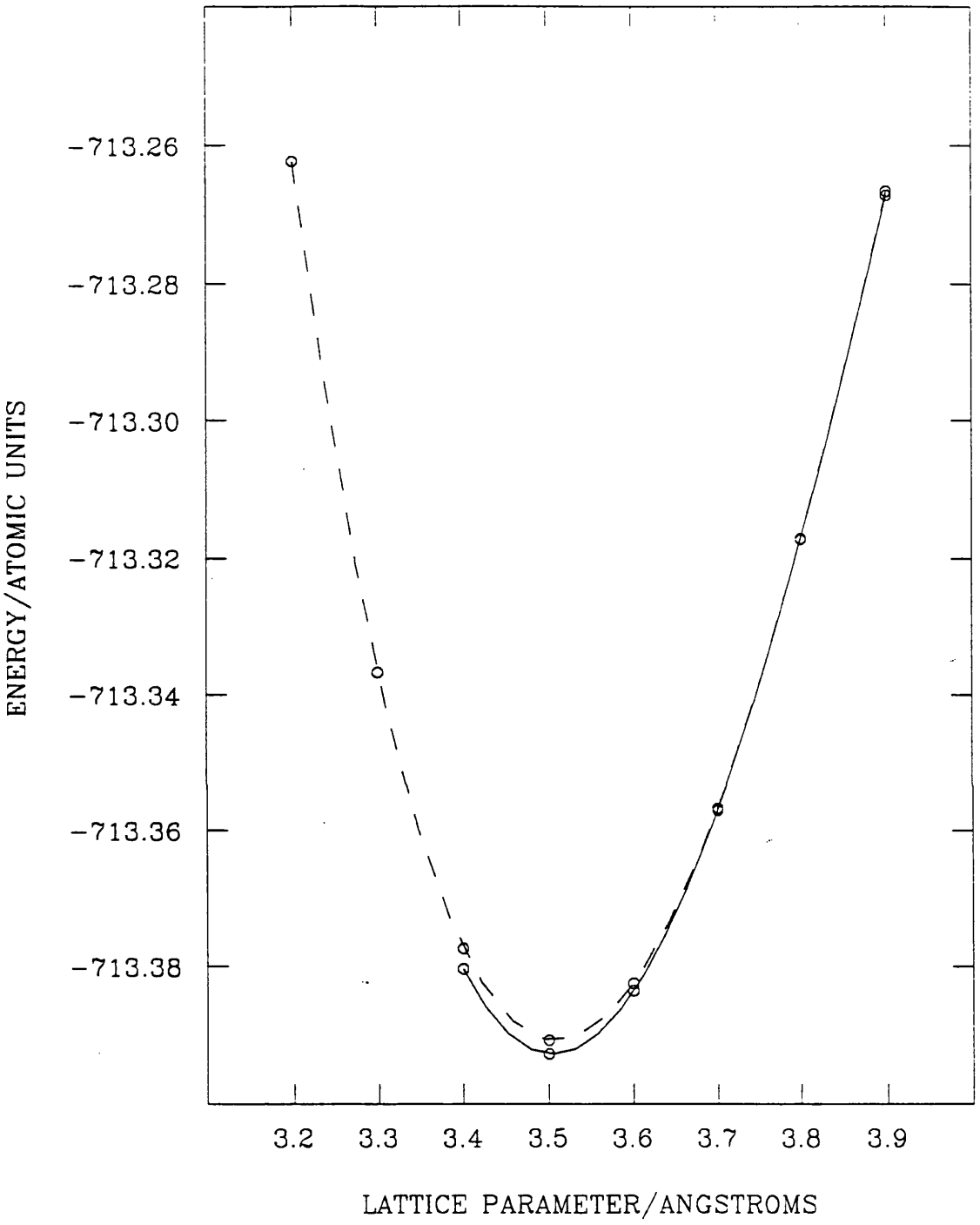

Figure 5.2 Variationally optimised lattice parameter for the cubic $MgSiO_3$ perovskite (BS1 = ------).

following table.

Table 5.1 Calculated energies, bulk moduli and cell volumes

	Energy/a.u.	K/GPa	Cell Volume/Å^3
BS1	-713.376	295.3	43.16
BS2	-713.380	297.7	43.01

We see that the energies, cell volumes and bulk moduli are in very close agreement for both b.s. implying, as stated above, the possible transferability of b.s. from one similar symmetry to another. It is encouraging to note the comparability of these results with the Linear Augmented Plane Wave (LAPW) method (an alternative ab initio method) of Cohen et al. (1989) where they found an optimum cell volume of 42.14Å^3 and a bulk modulus of 279 GPa. It is interesting that both ab initio methods predict a bulk modulus which is larger than the observed bulk modulus for the orthorhombic perovskite (i.e. 245 GPa, see Yeganeh-Haeri et al. 1989). This is as expected because it is generally found from high-pressure and vibrational spectroscopy experiments (see, for example, Angel et al. 1990) that it is more difficult to compress the octahedra than to rotate it, therefore the regular "packed" cubic case can only be deformed by compression (i.e. shortening of the Si - O bond) and will give a larger bulk modulus. These preliminary calculations have been extended by Nada et al. (1992b) to investigate the electronic properties of, not only the cubic perovskite, but the other possible symmetries as well.

It is possible to obtain an HF energy "hypersurface" if calculations are performed for variations in the three cell parameters **a, b** and **c**. This is a good approximation to the potential energy distribution of a crystal structure if the contribution from the correlation energy is small. Alternatively, one can use other quantum mechanical procedures such as the LAPW method (see for example,

Cohen et al. 1989) which accounts for such electron correlations. Once the energy surface is obtained a straightforward least-squares fitting procedure to the function given in equation 2.2 will yield the necessary parameters. This eliminates the empirical approach to obtaining accurate potential energy functions and it is hoped that the quantum mechanical method can be incorporated into PARAPOCS as a primary routine.

5.3 Summary

All electron HF-LCAO periodic calculations were performed for the cubic $MgSiO_3$ perovskite (an idealised structure) and successful geometry optimisations were performed for, not only the re-optimised b.s., but also the original b.s. which were originally developed for the ilmenite structure. Although only ground state energies can be calculated with this method, a definite application of this type of calculation is to determine the potential energy surfaces for particular crystal structures. Subsequently, potentials obtained by fitting to such an ab initio energy surface can be incorporated into the PARAPOCS code thus eliminating the problem of empirically determined potentials. It must be stressed that the HF approximation will fail to give accurate potential energy surfaces where the electron correlation is significant, therefore, this will limit its applicability to the number of materials that can be studied in the geological context. However, it may be possible to overcome this problem by including the option of an ab initio LAPW calculation within PARAPOCS code.

CHAPTER SIX

SUMMARY

As was stated in Chapter One, there is a great demand for accurate data of structural, elastic and thermodynamic properties of the Earth-forming silicates so that refinements can be made to existing compositional models, in particular phase diagrams, and discrepancies between the precise interrelationships of the interior Earth models are clarified. It is hoped that from such clarification, insight into the exact conditions for the formation and evolution of the Earth is gained. Experiments to simulate the conditions of the mantle and core are obviously difficult. Therefore, theoretical models which can predict the required geophysical data at such conditions are of immediate importance and provide a complement to gaining information of inaccessible terrain.

The research presented in this thesis was a theoretical investigation into the lattice and thermodynamics of the major Earth-forming silicates. We have used an atomistic approach based on the Born model of solids, in which potential functions represent the interactions between atoms in a structure. This work is, not only an extension the previous work but also a rigorous test of the methodology. We also set out to find how reliable the LDS model is in varying geological conditions (i.e. differing pressures and temperatures).

In Chapter Three we chose the modelling of oxygen isotope fractionation between the silicates; albite, diopside, forsterite, α-quartz, pyrope and wollastonite, as a stringent test for our approach. More precisely, the calculations were based on a lattice dynamics model to the quasi-harmonic level of approximation using the computer code PARAPOCS. Overall, we concluded that the model works very well, although the calculated fractionation factors are not yet sufficiently accurate

to be practically useful. The predicted structure and bulk thermodynamics of the silicates however are excellent and this clearly shows that the type of model potentials used in this approach are genuinely transferable, and can be applied to a wide variety of structural topologies (ortho-, chain-, layer- and framework-silicates). We suggested that the thermodynamic properties predicted from our fundamental, microscopic, atomistic models can now be considered as reliable as the predictions made by other bulk, phenomenological or empirical approaches. Also, refinements of the potential parameters is necessary if we are to predict accurately the structures and thermodynamic properties (to within 0.1% of observed values) that appear to be required if our approach is to be extended to the quantitative study of isotope effects, and rigorous testing of the temperature and pressure dependency of the fractionation factor.

The success of the lattice dynamics model in the geophysical context will be determined by its performance at a variety of temperature and pressures, especially under extreme conditions. The work presented in Chapter Four was the result of detailed analysis of this point. We compared calculations based on the QHA with corresponding MDS (i.e. intrinsic anharmonicity included) derived results for the geophysically important minerals periclase (MgO) and $MgSiO_3$ perovskite. It has been clearly shown that the QHA breaks down at high temperatures and low pressures and this deviation from the "true" values is reduced when the external pressure is increased. In fact, for the molar volume, enthalpy and isothermal bulk modulus the two approaches converge at very high pressures implying that the intrinsic anharmonic effects are negligible at these conditions. It has also been demonstrated that the major shortcoming of our methodology is insufficient data (i.e. sampling at many more points in P-T space) so that precise polynomial fits could be achieved in order to calculate other physical properties with minimal uncertainty. On the whole, the effects of intrinsic anharmonicity reduces the Anderson-Grüneisen parameters and this has the possible conclusion that the experimental values derived from seismic data (i.e. the lateral variations in the seismic velocities) implicitly include such effects explaining why they are generally lower than the values found from other experimental procedures. Overall,

for the geophysical context, this implies that it is necessary to use the MDS technique for upper mantle conditions and the LDS model is limited to the lower mantle although, in the near future, improvements such as the inclusion of anharmonic potentials and phonon-phonon interactions can be made to remove such restrictions. Also, to achieve a greater flexibility with the MDS technique the shell model can be incorporated into the calculation of the overall potential energy.

The obvious limitation of the atomistic modelling approach is the dependency on empirical fitting for suitable potential energy distributions of the system under study. This can be overcome by adopting so-called "a priori" methods for calculating the potential energy surface of a variety of geometries and then deriving the necessary information (i.e. the potential parameters) from a least-squares fitting to the surface. To penetrate beyond the atomistic realm we have to go into the subatomic world of electrons and nuclei. All electron HF-LCAO periodic calculations were performed for the geologically relevant cubic $MgSiO_3$ perovskite (an idealised structure) using the computer code CRYSTAL. Successful geometry optimisations were performed for, not only the re-optimised basis sets, but also the original basis set which were developed for the ilmenite structure. Subsequently, potentials obtained by fitting to such an ab initio energy surface can be incorporated into the PARAPOCS code, thus eliminating the problem of empirically determined potentials.

Finally, we can be hopeful that the indications made for developing the PARAPOCS code will be pursued in the near future and this will ultimately provide a reliable and accurate theoretical technique for studying minerals at any geological condition. With such a powerful tool, coupled with the growing experimental techniques to probe such levels, the models of the Earth's interior can be clarified to give an overall consistent picture. Ultimately, this may shed light on the beginning and evolution of the Earth.

REFERENCES

Akaogi M, Ross N, MacMillan P, Navrotsky A (1984) The Mg_2SiO_4 polymorphs (olivine, modified spinel and spinel) - Thermodynamic properties from oxide melt solution calorimetry, phase relations and models of lattice vibrations. Amer. Mineral. 69:499-512

Akaogi M, Ito E, Navrotsky A (1989) Olivine-modified spinel-spinel transitions in the system Mg_2SiO_4 - Fe_2SiO_4: calorimetric measurements, thermochemical calculation, and geophysical application. J. Geophys. Res. 94:15671-15685

Andersen HC (1980) Molecular dynamics simulations at constant pressure and/or temperature. J Chem Phys 72:2384-2393

Anderson DL (1987a) Thermally induced phase changes, lateral heterogeneity of the mantle, continental roots and deep slab anomalies. J. Geophys. Res. 92:13968-13980

Anderson DL (1987b) A seismic equation of state II, shear and thermodynamic properties of the lower mantle. Phys Earth Planet Inter 45:307-323

Anderson DL (1989) Theory of the Earth. Blackwell, Oxford.

Anderson OL (1967) Equation for thermal expansivity in planetary interiors. J Geophys Res 72:3661-3668

Anderson OL (1982) The Earth's core and the phase diagram of iron. Phil Trans R Soc Lond A306:21-35

Anderson OL, Suzuki I (1983) Anharmonicity of three minerals at high temperature: Forsterite, fayalite and periclase. J Geophys Res 88:3549-3556

Anderson OL, Chopelas A, Boehler R (1990) Thermal expansivity vs. pressure at constant temperature: A re-examination. Geophys Res Lett 17:685-688

Angel RJ, Carpenter MA, Finger LW (1990) Structural variation associated with compositional variation and order-disorder behaviour in anorthite-rich feldspars. Am Mineral 75:150-162

Baldereschi A (1973) Mean-value point in the Brillouin zone. Phys Rev B7:5212-5215

Ball RD (1989) Anharmonic lattice dynamics. In: Ionic Solids at High Temperatures. Ed. Stoneham M , World Scientific, Singapore, 9-105

Barker JA, Fisher RA, Watts RO (1971) Liquid argon - Monte Carlo and molecular dynamics calculations. Mol Phys 21:657

Bassett WA (1977) The diamond cell and the nature of the Earth's interior. Ann. Rev. Earth Planet. Sci. 7:357-384

Bigeleisen J, Mayer MG (1947) Calculation of equilibrium constants for isotopic exchange reactions. J Chem Phys 15:261-267

Bolt BA (1982) Inside the Earth. Freeman, San Francisco

Born M, Huang K (1954) Dynamical theory of crystal lattices. Clarendon Press, Oxford.

Bottinga Y, Javoy M (1973) Comments on oxygen isotope geothermometry. Earth Planet Sci Lett 20:250-265

Bottinga Y, Javoy M (1975) Oxygen isotope partitioning among the minerals in igneous and metamorphic rocks. Rev Geophys Space Phys 13:401-418

Boyer LL (1981) First-principles theory of phase transformations in ionic solids. Ferroelectrics 35:83-88

Boyer LL (1984) Parameter-free equation of state for $CsCaF_3$. J Phys C 17:1825-1832

Boyer LL, Hardy JR (1981) Theoretical study of the structural phase transition in $RbCaF_3$. Phys Rev B 24:2577-2591

Brown GC, Mussett AE (1981) The Inaccessible Earth. George Allen and Unwin, London.

Brown JM, McQueen RG (1986) Phase transitions, Grüneisen parameter and elasticity for shocked iron between 77 GPa and 400 GPa. J Geophys Res 91:7485-7494

Brown JM, Shankland TJ (1981) Thermodynamic parameters in the Earth as determined from seismic profiles. Geophys J R Astr Soc 66:579-596

Brüesch P (1982) Phonons: Theory and Experiment I. Springer-Verlag, Berlin

Catlow CRA, Cormack AN, Theobald F (1984) Structure prediction of transition-metal oxides using energy-minimization techniques. Acta Cryst B40:195-200

Catlow CRA, Mackrodt WC (1982) Theory of simulation methods for lattice and defect energy calculations in crystals. In: Computer simulation of Solids (Eds Catlow CRA, Mackrodt WC). Lecture notes in Physics 166, 3-20. Springer-Verlag, Berlin Heidelberg New York

Catlow CRA, Norgett MJ (1976) U.K.A.E.A Report A.E.R.E M2936, United Kingdom Atomic Energy Authority. Harwell

Chadi DJ, Cohen ML (1973) Special points in the Brillouin zone. Phys Rev B8:5747-5753

Chiba H, Chacko T, Clayton RN, Goldsmith JR (1989) Oxygen isotope fractionation involving diopside, forsterite, magnetite and calcite: application to geothermometry. Geochim Cosmochim Acta 53:2985-2995

Clayton RN (1981) Isotopic thermometry. In: Thermodynamics of Minerals and Melts (Eds Newton RC, Navrotsky A, Wood BJ). Springer-Verlag, Berlin, pp85-109

Clayton RN, Goldsmith JR, Karel KJ, Mayeda TK, Newton RC (1975) Limits on the effect of pressure on isotopic fractionation. Geochim Cosmochim Acta 39:1197-1201

Clayton RN, Goldsmith JR, Mayeda TK (1989) Oxygen isotope fractionation in quartz, albite, anorthite and calcite. Geochim Cosmochim Acta 53:725-733

Cochran W (1973) The dynamics of atoms in crystals. Edward Arnold, London

Cohen RE, Boyer LL, Mehl MJ, Pickett WE, Krakauer H (1989) Electronic structure and total energy calculations for oxide perovskites and superconductors. In: Perovskites, a structure of great interest to geophysics and materials science (eds. A Navrotsky and DJ Weidner). Geophys Monograph 45:55-66, AGU, Washington

Dove M (1988) Molecular dynamics simulation in the solid state sciences. In: Physical Properties and Thermodynamic Behaviour of Minerals. Ed. Salje EKH 501-590, D. Reidel, Dordrecht.

Dovesi R, Pisani C, Roetti C, Causa' M, Saunders VR (1988) CRYSTAL88. An ab initio all-electron LCAO-Hartree-Fock program for periodic systems. QCPE

Program N.577, Quantum Chemistry Program Exchange, Indiana University, Bloomington, Indiana, USA

Dziewonski AM, Anderson DL (1981) Preliminary Reference Earth Model. Phys. Earth Planet. Interiors 25:297-356

Filippini G, Gramaccioli Cm, Simonetta M, Suffritti GB (1976) Lattice-dynamical applications to crystallographic problems: consideration of the Brillouin zone sampling. Acta Crystallogr A32:259-264

Finger LW, Ohashi Y (1976) The thermal expansion of diopside to 800°C and a refinement of the crystal structure at 700°C. Am Mineral 61:303-310

Fujino K, Sasaki S, Takeuchi Y, Sadanaga R (1981) X-ray determination of electron distributions in forsterite, fayalite and tephroite. Acta Crystallogr B37:513-518

Gear CW (1971) Numerical Initial Value Problems in Ordinary Differential Equations. Prentice-Hall

George DV (1972) Principles of Quantum Chemistry. Pergamon Press, New York.

Gillet P, Guyot F, Malezieux JM (1989) High pressure, high temperature Raman spectroscopy of Ca_2GeO_4 (olivine form): Some insights on anharmonicity. Phys Earth Planet Int 58:141-154

Gillet P, Richet P, Guyot F, Fiquet G (1991) High-temperature thermodynamic properties of forsterite. J Geophys Res 96:11805-11816

Gordon RG, Kim YS (1972) Theory of the forces between closed-shell atoms and molecules. J Chem Phys 56:3122-3132

Gurevich VM, Khlyustov VG (1979) Calorimeter for determining of low-temperature heat capacity of minerals. Quartz heat capacity under the temperature 9-300K. Geokhimiia 6:829-839

Haile JM, Graben HW (1980) Molecular dynamics simualations extended to various ensembles. 1. Equilibrium properties in the isoenthalpic-isobaric ensemble. J Chem Phys 73:2412

Hansen JP, Weis JJ (1969) Quantum corrections to coexistence curve of neon near triple point. Phys Rev 188:314

Hardy RJ (1980) Temperature and pressure dependence of intrinsic anharmonicity and quantum corrections to the equation of state. J. Geophys. Res. 85:7011-7015

Harlow GE, Brown GE (1980) Low albite: an x-ray and neutron diffraction study. Am Mineral 65:986-995

Hart SR, Zindler A (1986) In search of a bulk Earth composition. Chemical Geology 57:247-267

Haselton HT, Westrum EF (1980) Low-temperature heat capacities of synthetic pyrope, grossular and $pyrope_{60}grossular_{40}$. Geochim Cosmochim Acta 44:701-709

Hehre WJ, Stewart RF, Pople JA (1969) Self-consistent molecular-orbital methods. I. Use of gaussian expansion of Slater-Type atomic orbitals. J Chem Phys 51:2657-2664

Hemingway BS (1987) Quartz: heat capacities from 340 to 1000K and revised values for the thermodynamic properties. Am Mineral 72:273-279

Hemley RJ, Bell PM, Mao HK (1987) Laser techniques in high-pressure geophysics. Science 237:605-612

Holland TJB (1989) Dependence of entropy on volume for silicate and oxide minerals: a review and a predictive model. Am Mineral 74:5-13

Hoover WG, Holt AC, Squire DR (1969) Adiabatic elastic constants for argon. Theory and Monte Carlo calculations. Physica 44:437

Isaak DG, Anderson OL, Cohen RE (1992) The relationship between shear and compressional velocities at high pressures: Reconciliation of seismic tomography and mineral physics. Geophys Res Lett 19:741-744

Ito E, Katsura T (1989) A temperature profile of the mantle transition zone. Geophys Res Lett 16:425-428

Jackson RA, Catlow CRA (1988) Computer simulation studies of zeolite structure. Mol Simulation 1:207-224

James R (1979) PhD Thesis, Univ. of London.

Jeanloz R, Thompson AB (1983) Phase transitions and mantle discontinuities. Rev. Geophys. Space Phys. 21:51-74

Katsura T, Ito E (1989) The system Mg_2SiO_4 - Fe_2SiO_4 at high pressures and temperatures: precise determination of stabilities of olivine, modified spinel and spinel. J. Geophys. Res. 94:15663-15670

Kieffer SW (1982) Thermodynamics and lattice vibrations of minerals V. Rev Geophys Space Phys 20:827-849

Kieffer SW, Navrotsky A (1985) Microscopic to Macroscopic. Reviews in Mineralogy 14. Mineralogical Soc America, Washington

Krupka KM, Robie RA, Hemingway BS, Kerrick DM, Ito J (1985a) Low-

temperature heat capacities and derived thermodynamic properties of anthophyllite, diopside, enstatite, bronzite and wollastonite. Am Mineral 70:249-260

Krupka KM, Hemingway BS, Robie RA, Kerrick DM (1985b) High-temperature heat capacities and derived thermodynamic properties of anthophyllite, diopside, dolomite, enstatite, bronzite, talc, tremolite and wollastonite. Am Mineral 70:261-271

Landau LD, Lifshitz EM (1958) Statistical Physics. Pergamon Press, London.

Lasage A, Gibbs JV (1987) Applications of quantum mechanical potential surfaces to mineral physics calculations. Phys Chem Minerals 14:107-117

Leitner BJ, Weidner DJ, Liebermann RC (1980) Elasticity of single crystal pyrope and implications for garnet solid solution series. Phys Earth Planet Inter 22:111-121

LePage Y, Calvert LD, Gabe EJ (1980) Parameter variation in low-quartz between 94 and 298K. J Phys Chem Solids 41:721-725

Levien L, Prewitt CT (1981) High- pressure structural study of diopside. Am Mineral 66:315-323

Levien L, Weidner DJ, Prewitt CT (1979) Elasticity of diopside. Phys Chem Minerals 4:105-113

Lewis GV (1985) Interatomic potentials: Derivation of parameters for binary oxides and their use in ternary oxides. Physica 131B:114-118

Lewis GV, Catlow CRA (1985) Potential models for ionic oxides. J Phys C: Solid State Phys 18:1149-1161

Mao HK, Bell PM (1979) Equation of state of MgO and ε-Fe under static pressure

conditions. J Geophys Res 84:4533-4536

Mao HK, Hemley RJ, Fei Y, Shu JF, Chen LC, Jephcoat AP, Wu Y, Bassett WA (1991) Effect of pressure, temperature and composition on lattice parameters and density of (Fe,Mg)SiO_3-perovskites to 30 GPa. J Geophys Res 96:8069-8079

Matsuhisa Y, Goldsmith JR, Clayton RN (1979) Oxygen isotopic fractionation in the system quartz-albite-anorthite-water. Geochim Cosmochim Acta 43:1131-1140

Matsui T, Manghnani MH (1985) Thermal expansion of single-crystal forsterite to 1023K by Fizeau interferometry. Phys Chem Minerals 12:201-210

Matsui M (1988) Molecular dynamics study of $MgSiO_3$ perovskite. Phys Chem Minerals 16:234-238

Matsui M (1989) Molecular dynamics study of the structural and thermodynamic properties of MgO crystal with quantum correction. J Chem Phys 91:489-494

Matsui M, Price GD (1992) Computer simulation of the $MgSiO_3$ polymorphs. Phys Chem Minerals 18:365-372

Matthews A, Goldsmith JR, Clayton RN (1983) Oxygen isotope fractionations involving pyroxenes: the calibration of mineral-pair geothermometers. Geochim Cosmochim Acta 47:631-644

McSkimin HJ, Andreatch P, Thurston RN (1965) Elastic moduli of quartz versus hydrostatic pressure at 25° and -195.8°C. J Appl Phys 36:1624-1632

Nada R, Catlow CRA, Dovesi R, Pisani C (1990) An ab-initio Hartree-Fock study of α-quartz and stishovite. Phys Chem Minerals 17:353-362

Nada R, Catlow CRA, Dovesi R, Saunders VR (1992a) An ab-initio Hartee-Fock

study of the ilmenite-structured $MgSiO_3$. Proc R Soc (Lond) A 436:499-509

Nada R, Stuart JA, Ross N, Patel A, Price GD (1992b) A comparative periodic ab-initio Hartee-Fock study of the stability of ilmentie-, cubic perovskite-, rhombohedral perovskite- and $LiNbO_3$ - structured $MgSiO_3$. Preprint

Norgett MJ, Fletcher R (1970) Fast matrix methods for calculating relaxation about defects in crystals. J Phys C 3:163

Nosé S (1984) A unified formulation of the constant temperature molecular dynamics methods. J Chem Phys 81:511-519

Nosé S, Klein ML (1983) A study of solid and liquid carbon tetrafluoride using the constant pressure molecular dynamics technique. J Chem Phys 78:6928-6939

Novak GA, Gibbs GV (1971) The crystal chemistry of the silicate garnets. Am Mineral 56:791-825

Ohashi Y (1984) Polysnthetically-twinned structures of enstatite and wollastonite. Phys Chem Minerals 10:217-229

O'Neil JR (1986) Theoretical and experimental aspects of isotopic fractionation. Rev Mineral 16:1-40

O'Neil JR, Taylor HP (1967) The oxygen isotope and cation exchange cemistry of feldspars. Am Mineral 52:1414-1437

Openshaw RE, Hemingway BS, Robie RA, Waldbaum DR, Krupka KM (1976) The heat capacities at low temperatures and entropies at 298.15K of low albite, analbite, microline and high sanidine. J Res US Geol Surv 4:195-204

Parker SC, Price GD (1989) Computer modelling of phase transitions in minerals.

Adv Solid-State Chem 1:295-327

Parker SC, Watson G (1992) Private communication.

Parrinello M, Rahman A (1981) Polymorphic transitions in single crystals: A new molecular dynamics method. J Appl Phys 52:7182-7190

Peltier WR, Jarvis GT (1982) Whole mantle convection and the thermal evolution of the Earth. Phys. Earth Planet. Interiors 29:281-304

Pisani C, Dovesi R, Roetti C (1988) Hartree-Fock ab initio treatment of crystalline systems. Lecture Notes in Chemistry. Springer-Verlag, Heidelberg.

Poirier JP (1991) Introduction to the Physics of the Earth's Interior. Cambridge University Press, Cambridge.

Poirier JP (1986) Dislocation-mediated melting of iron and the temperature of the Earth's core. Geophys J R Astr Soc 85:315-328

Post JE, Burnham CW (1986) Ionic modelling of mineral structures and energies in the electron gas approximation: TiO_2 polymorphs, quartz, forsterite, diopside. Am Mineral 71:142-150

Price GD, Parker SC, Leslie M (1987) The lattice dynamics and thermodynamics of the Mg_2SiO_4 polymorphs. Phys Chem Minerals 15:181-190

Prigogine I, Stengers I (1984) Order out of Chaos. Fontana, London.

Reissland JA (1973) The Physics of Phonons. Wiley, London.

Reynard B, Price GD (1990) Thermal expansion of mantle minerals at high pressures - a theoretical study. Geophys Res Lett 17:689-692

Reynard B, Price GD, Gillet P (1992) Thermodynamic and anharmonic properties of forsterite, α-Mg_2SiO_4: Computer simulation vs. high pressure measurements. Preprint

Richter R, Hoernes S (1988) The application of the increment method in comparison with experimentally derived and calculated O-isotope fractionations. Chem Erde 48:1-18

Robie RA, Hemingway BS, Fisher JR (1978) Thermodynamic properties of minerals and related substances at 298.15K and 1Bar (10^4 pascals) pressure and at higher temperatures. US Geol Survey Bull 1452

Robie RA, Hemingway BS, Takei H (1982) Heat capacities and entropies of Mg_2SiO_4, Mn_2SiO_4 and Co_2SiO_4 between 5 and 380K. Am Mineral 67:470-482

Sanders MJ, Leslie M, Catlow CRA (1984) Interatomic potentials for SiO_2. J Chem Soc, Chem Communications 1271-1273

Schütze H (1980) Der isotopenindex- eine inkrementenmethode zur näherungsweisen berechnung von isotopenaustauschgleichgewichten zwischen kristallin substanzen. Chem Erde 39:321-334

Shankland TJ, Brown JM (1985) Homogeneity and temperatures in the lower mantle. Phys Earth Planet Interiors 38:51-58

Smyth JR (1989) Electrostatic characterization of oxygen sites in minerals. Geochim Cosmochim Acta 53:1101-1110

Spiliopoulos S, Stacey FD (1984) The Earth's thermal profile: Is there a mid-mantle thermal boundary layer? J Geodynamics 1:61-77

Suito K (1977) Phase relations of pure Mg_2SiO_4 up to 200 kilobars. In High-

pressure research, Manghnani MH, Akimoto S eds. Academic, New York, 255-266

Suzuki I, Anderson OL, Sumino Y (1983) Elastic properties of a single-crystal forsterite Mg_2SiO_4, up to 1,200K. Phys Chem Minerals 10:38-46

Urey HC (1947) The thermodynamic properties of isotopic substances. J Chem Soc (London) 562-581

Verhoogen J (1980) Energetics of the Earth. National Academy of Sciences, Washington D.C.

Wall A, Price GD (1988) Computer simulation of the structure, lattice dynamics and thermodynamics of ilmenite-type $MgSiO_3$. Am Mineral 73:224-231

Wall A, Price GD (1989) Electrical conductivity of the lower mantle: a molecular dynamics simulation of $MgSiO_3$ perovskite. Phys Earth Planet Int 58:192-204

Wang CY (1972) Temperatures in the lower mantle. Geophys J R Astr Soc 27:29-36

Weston RM, Rogers PS (1976) Anisotropic thermal expansion characteristics of wollastonite. Mineral Mag 40:649-651

White GK, Roberts RB, Collins JG (1985) High Temp. High Press. 17:61

Williams DE (1971) Accelerated convergence of crystal lattice potential sums. Acta Crystallogr A27:452

Williams Q, Jeanloz R, Bass J, Svendsen B, Ahrens TJ (1987) The melting curve of iron to 250GPa: A constraint on the temperature at the Earth's center. Science 236:181-182

Williamson ED, Adams LH (1923) Density distribution in the Earth. J. Washington Acad. Sci. 13:413-428

Winkler B, Dove MT, Leslie M (1990) Static lattice energy minimization and lattice dynamics calculations on alumino-silicate minerals. Preprint

Yeganeh-Haeri A, Weidner DJ, Ito E (1989) Single-crystal elastic properties of $MgSiO_3$. In: Perovskites, a structure of great interest to geophysics and materials science (eds. A Navrotsky and DJ Weidner). Geophys Monograph 45, AGU, Washington

APPENDIX

Table A1 Enthalpy and volume data calculated at various pressures and temperatures for MgO.FI LDS model.

P/kbars	T/K	Enthalpy/kJmol^{-1}K^{-1}	Volume/cm^{3}mol^{-1}
0.001	500.0	-3891.6315	11.3569
	1000.0	-3867.3309	11.5664
	1500.0	-3840.5645	11.8354
	2000.0	-3810.3398	12.2378
100.0	500.0	-3782.3414	10.8327
	1000.0	-3758.5919	10.9800
	1500.0	-3732.9106	11.1523
	2000.0	-3705.9251	11.3545
200.0	1000.0	-3653.9541	10.5225
	2000.0	-3602.5822	10.7956
	3000.0	-3547.4024	11.1428
	4000.0	-3484.9351	11.6656
300.0	1000.0	-3552.8789	10.1446
	2000.0	-3502.1974	10.3615
	3000.0	-3448.7488	10.6181
	4000.0	-3391.9960	10.9358
400.0	1000.0	-3454.9093	9.8221
	2000.0	-3404.6760	10.0024
	3000.0	-3352.1403	10.2083
	4000.0	-3297.3901	10.4473

Table A1 Continued

P/kbars	T/K	Enthalpy/kJmol^{-1}K^{-1}	Volume/cm^{3}mol^{-1}
500.0	1000.0	-3359.6794	9.5409
	2000.0	-3309.7698	9.6952
	3000.0	-3257.8133	9.8678
	4000.0	-3204.1512	10.0616
1000.0	1000.0	-2915.9249	8.5100
	2000.0	-2866.9160	8.5986
	3000.0	-2816.2690	8.6942
	4000.0	-2764.7006	8.7954

Table A2 Enthalpy and volume data calculated at various pressures and temperatures for MgO.FI MDS model.

P/kbars	T/K	Enthalpy/kJmol^{-1}K^{-1}	Volume/cm^{3}mol^{-1}
-0.4340	498.6	-3895.248826	11.3371
-0.0275	999.8	-3869.805696	11.5332
-0.0830	1500.0	-3843.503414	11.7426
-0.0392	1999.4	-3816.583250	11.9760
100.0	499.1	-3786.468073	10.8184
99.9	999.4	-3760.712630	10.9678
100.0	1500.2	-3734.934165	11.1163
100.0	2000.2	-3708.528338	11.2775
200.0	1000.3	-3656.258081	10.5132
199.9	2000.3	-3604.233668	10.7586
199.9	2999.6	-3550.647975	11.0258
200.0	4000.0	-3494.954725	11.3157
299.9	1001.5	-3555.171746	10.1416
299.9	2000.1	-3503.525625	10.3371
300.0	3000.2	-3450.403686	10.5582
299.8	3999.5	-3395.517818	10.7900
400.0	999.3	-3457.315202	9.8188
400.0	2000.4	-3405.763699	9.9905
399.9	2999.7	-3353.053044	10.1734
399.8	3999.8	-3298.495662	10.3612

Table A2 Continued

P/kbars	T/K	Enthalpy/kJmol^{-1}K^{-1}	Volume/cm^{3}mol^{-1}
500.0	1000.4	-3362.129317	9.5394
499.9	2000.0	-3310.708796	9.6883
499.9	3000.1	-3258.107135	9.8411
499.8	3999.6	-3204.349260	9.9993
1000.4	1000.1	-2918.357158	8.5197
999.9	2000.0	-2867.564795	8.6000
999.9	2999.5	-2815.699113	8.6874
999.9	4000.9	-2762.559378	8.7844

Table A3 Enthalpy and volume data calculated at various pressures and temperatures for MgO.PI LDS model.

P/kbars	T/K	Enthalpy/kJmol^{-1}K^{-1}	Volume/cm^{3}mol^{-1}
0.001	500.0	-2029.9077	11.4482
	1000.0	-2004.2635	11.7739
	1500.0	-1973.5701	12.2979
100.0	500.0	-1920.6773	10.8662
	1500.0	-1869.1092	11.3290
	2000.0	-1839.3324	11.6644
	2500.0	-1802.5001	12.2374
200.0	500.0	-1815.8343	10.4287
	1000.0	-1791.9328	10.5810
	1500.0	-1765.8335	10.7608
	2000.0	-1738.2027	10.9701
	2500.0	-1708.7061	11.2217
	3000.0	-1676.1309	11.5494
	3500.0	-1633.8410	12.1344
300.0	500.0	-1714.5533	10.0771
	1000.0	-1691.0653	10.1981
	1500.0	-1665.4795	10.3379
	2000.0	-1638.7067	10.4942
	2500.0	-1610.7679	10.6703
	3000.0	-1581.4016	10.8728
	3500.0	-1550.0141	11.1149

Table A3 Continued

P/kbars	T/K	Enthalpy/kJmol^{-1}K^{-1}	Volume/cm^{3}mol^{-1}
400.0	500.0	-1616.2576	9.7832
	1500.0	-1567.8488	9.9981
	2000.0	-1541.5657	10.1239
	2500.0	-514.3903	10.2616
	3000.0	-1486.2510	10.4134
	3500.0	-1456.9539	10.5833
500.0	500.0	-1520.5294	9.5307
	1500.0	-1472.6443	9.7135
	2000.0	-1446.6882	9.8191
	2500.0	-1419.9829	9.9328
	3000.0	-1392.5285	10.0555
	3500.0	-1364.2449	10.1890
	4000.0	-1334.9855	10.3356

Table A4 Enthalpy and volume data calculated at various pressures and temperatures for MgO.PI MDS model.

P/kbars	T/K	Enthalpy/kJmol^{-1}K^{-1}	Volume/cm^{3}mol^{-1}
-0.0434	1000.2	-2006.053544	11.6956
-0.0355	1249.8	-1993.611718	11.8572
0.0043	1499.8	-1979.880587	12.0294
-0.0110	1749.7	-1965.680565	12.2065
-0.0807	2000.6	-1951.174124	12.4099
-0.0367	2500.4	-1920.840793	12.8566
-0.0698	3000.1	-1886.375140	13.5005
99.9	1000.1	-1898.658229	11.0361
99.9	1250.0	-1885.478408	11.1440
99.9	1499.5	-1872.053737	11.2560
100.0	1750.1	-1858.505291	11.3719
99.9	2000.4	-1844.778640	11.4836
99.9	2499.8	-1816.411442	11.7376
99.9	3000.2	-1786.993410	12.0219
99.9	3499.3	-1756.345307	12.3488
200.0	1000.1	-1794.411895	10.5617
200.0	1249.9	-1781.367500	10.6388
199.9	1500.2	-1768.188157	10.7203
200.0	1750.1	-1754.752297	10.8098
199.9	2000.0	-1741.330857	10.8941
199.9	2500.0	-1713.862173	11.0791
199.9	2999.9	-1685.672098	11.2721
200.0	3498.9	-1656.466636	11.4825

Table A4 Continued

P/kbars	T/K	Enthalpy/kJmol^{-1}K^{-1}	Volume/cm^{3}mol^{-1}
300.0	1000.5	-1693.648629	10.1805
300.0	1250.1	-1680.666294	10.2447
299.9	1500.1	-1667.539076	10.3113
300.0	1749.8	-1654.358911	10.3809
299.9	1999.7	-1641.006244	10.4496
300.0	2499.9	-1614.020438	10.5930
299.9	2999.8	-1586.192495	10.7425
300.0	3499.5	-1557.983236	10.9003
400.0	749.6	-1608.674772	9.8157
399.9	999.9	-1595.831274	9.8697
400.0	1500.5	-1569.876407	9.9790
399.9	2000.1	-1543.521156	10.0957
399.9	2500.3	-1516.706552	10.2111
399.9	3000.1	-1489.466513	10.3383
399.9	3499.4	-1461.549067	10.4632
499.9	749.1	-1513.335894	9.5572
499.9	1249.5	-1487.605160	9.6497
499.9	1500.0	-1474.563722	9.6947
499.9	1999.3	-1448.466975	9.7950
499.8	2500.0	-1421.737227	9.8955
499.9	3000.0	-1394.683639	9.9996
499.9	3499.6	-1367.221713	10.1146
499.9	4000.4	-1338.964623	10.2287

Table A5 Enthalpy and volume data calculated at various pressures and temperatures for $MgSiO_3$ perovskite LDS model.

P/kbars	T/K	Enthalpy/kJmol^{-1}K^{-1}	Volume/cm^{3}mol^{-1}
0.001	500.0	-7082.1800	24.6811
	750.0	-7052.8050	24.9386
	1000.0	-7020.6305	25.2493
	1250.0	-6985.7573	25.6473
100.0	500.0	-6844.1752	23.7439
	1000.0	-6784.7901	24.1328
	1500.0	-6718.4861	24.6224
	2000.0	-6645.1312	25.2925
200.0	500.0	-6613.6089	22.9875
	1000.0	-6555.4226	23.2901
	1500.0	-6491.1120	23.6496
	2000.0	-6422.8722	24.0720
	2500.0	-6349.7407	24.5947
	3000.0	-6265.6287	25.3802
300.0	500.0	-6389.4041	22.3502
	1000.0	-6332.0883	22.5991
	1500.0	-6268.8636	22.8884
	2000.0	-6202.5065	23.2135
	2500.0	-6133.1608	23.5832
	3000.0	-6060.0088	24.0179

Table A5 Continued

P/kbars	T/K	Enthalpy/kJmol^{-1}K^{-1}	Volume/cm^{3}mol^{-1}
400.0	500.0	-6170.7341	21.7986
	1000.0	-6114.1217	22.0105
	1500.0	-6051.6291	22.2541
	2000.0	-5986.3579	22.5220
	2500.0	-5918.7783	22.8168
	3000.0	-5848.6911	23.1450
500.0	500.0	-5956.9523	21.3122
	1000.0	-5900.9475	21.4967
	1500.0	-5839.0043	21.7078
	2000.0	-5774.4691	21.9370
	2500.0	-5707.9663	22.1847
	3000.0	-5639.5225	22.4536
	3500.0	-5568.9010	22.7485
	4000.0	-5495.6040	23.0772
1000.0	500.0	-4946.3893	19.4890
	1000.0	-4892.6934	19.5990
	1500.0	-4832.4626	19.7250
	2000.0	-4769.8590	19.8589
	2500.0	-4705.8385	19.9991
	3000.0	-4640.7077	20.1453
	3500.0	-4574.5595	20.2976

Table A6 Enthalpy and volume data calculated at various pressures and temperatures for $MgSiO_3$ perovskite MDS model.

P/kbars	T/K	Enthalpy/kJmol^{-1}K^{-1}	Volume/cm^{3}mol^{-1}
-0.0632	750.5	-7061.789015	24.8830
0.0175	999.9	-7029.052610	25.1440
-0.0619	1249.9	-6995.201434	25.4426
0.0047	1500.2	-6960.583161	25.7734
-0.0829	2000.3	-6887.256762	26.7214
100.0	499.9	-6857.585981	23.6927
100.0	1000.1	-6792.765094	24.0853
100.0	1500.0	-6726.337092	24.5093
99.9	2000.3	-6657.714246	24.9898
100.0	2500.2	-6586.020642	25.5318
200.0	500.0	-6628.170463	22.9413
200.0	1000.3	-6563.762480	23.2558
200.0	1500.3	-6497.948831	23.5884
200.0	2000.4	-6430.583556	23.9508
199.8	2500.2	-6361.213494	24.3522
199.9	3000.0	-6289.330411	24.7807
300.0	500.3	-6404.981420	22.3062
299.9	1000.0	-6340.945683	22.5687
299.9	1500.1	-6275.747414	22.8478
299.9	2000.0	-6209.110432	23.1392
299.9	2499.4	-6141.046879	23.4503

Table A6 Continued

P/kbars	T/K	Enthalpy/kJmol^{-1}K^{-1}	Volume/cm^{3}mol^{-1}
299.9	2999.7	-6071.254995	23.7883
300.0	3500.7	-5999.536785	24.1384
399.9	499.7	-6187.344660	21.7573
400.0	1000.2	-6123.454531	21.9841
400.0	1499.7	-6058.575656	22.2222
399.9	1999.8	-5992.647974	22.4679
399.9	2500.0	-5925.215582	22.7314
399.9	3000.5	-5856.256129	23.0076
399.9	3500.1	-5785.272162	23.3029
500.0	500.4	-5974.491732	21.2717
500.0	1000.1	-5910.722133	21.4734
499.9	1499.8	-5846.139071	21.6820
499.9	2000.0	-5780.540094	21.8982
500.0	2500.4	-5713.738638	22.1240
499.9	3000.4	-5644.969609	22.3677
499.9	3499.8	-5576.099973	22.6096
999.9	499.8	-4967.868003	19.4552
999.4	998.7	-4904.652182	19.5854
1000.0	1500.6	-4840.774881	19.7124
1000.0	2000.4	-4776.116127	19.8467
999.8	2500.0	-4710.701724	19.9843
999.9	3000.3	-4644.300231	20.1235
999.7	3500.4	-4577.117984	20.2678